Doctoral Dissertation

博士論文

Numerical study of earthquake generation processes on nonplanar faults

（非平面断層における地震発生過程の数値的研究）

A dissertation submitted for the Degree of Doctor of Philosophy
December 2021

令和 3 年 12 月　博士（理学）申請

Department of Earth and Planetary Science, Graduate School of Science,
The University of Tokyo

東京大学大学院　理学系研究科

地球惑星科学専攻

So Ozawa

小澤　創

Abstract

Recent advance in imaging subsurface faults revealed their extremely complex geometries, which may affect and even control the occurrence of earthquakes. In this thesis, I develop a highly-efficient method for earthquake sequence (cycle) simulations for nonplanar faults and present two applications for fundamental problems in earthquake science.

Earthquake sequence simulations based on the boundary element method have the flexibility of the fault geometries. Recently, H-matrices are often used to accelerate the computational cost from $O(N^2)$ to $O(N\log N)$. However, in large-scale parallel computing, the complicated structure of a H-matrix requires a high communication cost between CPUs and prevents us from scalable speed-up. Recently, the lattice H-matrices have been proposed for improvement of the original H-matrices in terms of parallel scalability. In this study, I implement lattice H-matrices in a quasi-dynamic earthquake sequence simulation code and test the accuracy and efficiency of my method against a nonplanar thrust fault. In a performance test conducted in Oakforest-PACS (a supercomputer system at University of Tokyo), I show more than 10-fold acceleration compared to the original H-matrices when a large number of MPI processes is used in parallel. Unprecedented large-scale simulations are now feasible with this algorithm.

While aftershocks are ubiquitous after a large mainshock, most earthquake sequence simulations cannot reproduce aftershock sequences. Building on several lines of observational evidence and theoretical consideration, I hypothesize that aftershocks are ruptures of small subsidiary faults surrounding the mainshock fault which has rough geometry. I validate our hypothesis using large-scale continuum mechanics-based earthquake sequence simulations. Our aftershock sequences display an Omori-type temporal decay and their locations delineate the mainshock fault geometry, as seen in nature. The simulations also reproduce log-time expansion of aftershock areas, diverse focal mechanisms, and spatial variation of their frequency-size distribution. This model extensively explains spatiotemporal characteristics of aftershock activities.

Fault bends are known to arrest rupture propagations in many earthquakes. To elucidate which factor controls the probability of rupture arrests in fault bends, I perform long-term earthquake sequence simulations on a fault that includes restraining and releasing bends, which are often seen in strike-slip faults. I use a novel stress relaxation method to avoid a pathological stress buildup due to the fault curvature. I perform a comprehensive parameter study to show that the probability of rupture arrests on the fault bend is primarily controlled by the angle of the bend and agrees with empirical laws obtained from historical earthquakes. Additionally, the spatial heterogeneity of long-term slip rates is consistent with a natural example of restraining bends.

要　旨

近年の地下の断層に対するイメージング技術の進歩により、非常に複雑な断層形状が明らかになってきた。複雑な断層形状は地震の発生に影響を与え、さらには制御するだろう。この論文では、非平面断層の地震シーケンス（サイクル）シミュレーションのための高効率な計算手法を開発し、地震科学における基本的な 2 つの問題に適用する。

境界要素法に基づく地震シーケンスシミュレーションには、断層形状に対して柔軟性がある。H 行列は、計算コストを$O(N^2)$から$O(N\log N)$に加速するために近年よく利用されている。ただし、大規模な並列コンピューティングでは、H 行列の複雑な構造により高い通信コストが必要であり、スケーラブルな高速化が妨げられている。近年，並列スケーラビリティの観点から H 行列の改善として格子 H 行列が提案されている。本研究では、準動的地震シーケンスサイクルシミュレーションコードに格子 H 行列を実装し、非平面逆断層に対する計算精度と計算効率を調べる。 東京大学のスーパーコンピュータシステム Oakforest-PACS で実施されたパフォーマンステストでは、多数の MPI 並列時において、元の H 行列と比較して 10 倍以上の高速化を示し、これまでにない大規模なシミュレーションが、このアルゴリズムで実現可能になった。

余震は大規模な本震の後に普遍的に発生するが、ほとんどの既存の地震シーケンスシミュレーション研究では余震系列を再現できない。我々はいくつかの観測的証拠と理論的考察に基づいて、「余震は凸凹形状を持つ本震断層を取り巻く小さな副次的断層の破壊である」という仮説を立てた。我々は、連続体力学に基づいた地震シーケンスシミュレーションで仮説を検証する。シミュレーション結果は、大森型の余震発生数の時間減衰を示し、それらの空間分布は、自然界に見られるように、本震断層に剃って分布する。また、余震領域の対数時間拡大、震源メカニズムの多様性、およびそれらの規模別頻度分布の空間不均一性を説明できる。

多くの地震において、断層の屈曲と破壊の停止の関連性が知られている。断層の屈曲での破壊停止が起きる頻度を決めるメカニズムを解明するために、本研究では、横ずれ断層によく見られるリストレイニングベンドとリリーシングベンドを含む断層で、地震シーケンスシミュレーションを行う。その際、断層の曲率による異常な法線応力の蓄積を回避するために、新しい応力緩和手法を用いる。そして、包括的なパラメータ研究により、断層屈曲での破壊停止の確率が主に屈曲の角度によって制御され、歴史地震から得られた経験則と一致することを示す。さらに、長期的滑り速度の走行方向の不均一性は、天然断層のリストレイニングベンドの例と一致する結果を得た。

Contents

1. General Introduction

The goal of this thesis is to improve our understanding of the earthquake generation and termination processes by taking faults' nonplanar geometries into account. I address this goal using numerical simulations based on continuum elasticity and friction laws. For this purpose, I develop a state-of-the-art high-performance computational method for quasi-dynamic earthquake sequence simulations. Using this method, I successfully explain various observations of aftershocks and earthquake rupture arrest at fault bends. In this chapter, we review previous work regarding the geometrical complexity of faults and earthquake sequence simulations, which serve as the basis for later chapters.

1.1. Geometrical complexity of faults

1.1.1. Fault geometry at the ground surface

Seismic hazard assessment requires the information on the geometry of regional active faults. Many efforts have been made to construct databases of regional faults, such as the active fault database by the Headquarters for Earthquake Research Promotion (HERP) in Japan and the community fault model by Southern California Earthquake Center (SCEC) in USA. Multidisciplinary approaches are used to obtain the geometries of faults as follows.

Geological and geomorphological analyses give the detailed distribution and long-term slip rates of active faults. The boundary of different geologic units informs us of the existence of a fault that experienced a large offset over geological time scales. The boundary between a plain and mountain area often corresponds to a dip-slip fault. Geomorphic markers, such as channel offsets and peaks of mountain ridges, are often produced by activities of strike-slip faults (Sieh & Jahns, 1984; Zielke et al., 2015). The use of geological and geomorphological analysis to investigate earthquakes that occurred in the past is referred to as paleoseismology (Grant Ludwig, 2015).

Meanwhile, modern remote sensing techniques can also be used to map fault traces as displacement discontinuity as well as the three-component displacement field in a high resolution when a large earthquake occurs. Remote sensing techniques include interferometric synthetic aperture radars (InSAR), airborne light detection and ranging (LiDAR) topographic surveys, and optical image correlation techniques using aerial photographs and satellite imagery (Fujiwara et al., 2016; Masson et al., 1993; Milliner et al., 2015; Oskin et al., 2012; Scott et al., 2019).

Nonplanar and complex fault geometries have been revealed by such measurement. Faults are usually segmented by stepovers or jogs (Klinger, 2010; Manighetti et al., 2007). Bends in major continental faults are universally observed, including the San Andreas fault, the North Anatolian fault, and the Dead Sea fault. Mann (2007) complied restraining and releasing fault bends worldwide. Further, faults often show bifurcations, also known as splay faulting (Ando et al., 2009; Moore et al., 2007; Scholz et al., 2010). Ando et al. (2009) reported that the angle of splay faults has a peak around 17° by analyzing the surface geometry of California faults. The geometrical complexity of faults is a hierarchical structure and exists at all scales like the concept of fractal (Ben-Zion & Sammis, 2003a; Otsuki & Dilov, 2005; Tchalenko, 1970). Okubo & Aki (1987) calculated the fractal dimension of surface fault traces in California using the box counting algorithm and obtained the values between 1.1 and 1.4.

Observations of outcrops of exhumed normal faults provide us finer scale geometries of faults. The topography of individual fault surfaces can be described as a self-affine fractal (Bistacchi et al., 2011; Brown & Scholz, 1985; Candela et al., 2009, 2012; Power et al., 1987; Power & Tullis, 1991; Renard et al., 2013). A self-affine geometry has statistically same appearance under a rescaling $\delta x \rightarrow \lambda \delta x, \delta y \rightarrow \lambda^H \delta y$, where H is called the Hurst exponent characterizing the self-affinity. In an outcrop scale, the Hurst exponent is ~ 0.6 for the slip-parallel direction and ~ 0.8 for the slip-perpendicular direction (Candela et al., 2009), which indicates that fault roughness in smaller scales is stronger than that in larger scales and fault roughness of slip- perpendicular direction is greater than that of slip-parallel direction. The former might reflect the scale-dependent strength of rocks (Brodsky et al., 2016), while the latter difference could be related to wearing processes due to slip (Candela & Brodsky, 2016). The term “fault roughness” or “rough fault” specifically refers to the self-affine nonplanar geometry of the fault.

The fractally rough fault might be still an oversimplification of natural fault geometry in the sense that a fault is an isolated single surface. Typical geologic observations of fault zones indicate slip is not localized into a single plane. Instead, multiple fault cores (slip surfaces) run in subparallel (Faulkner et al., 2003; Savage & Brodsky, 2011; Zoback et al. 2010), although some faults (e.g., the Punchbowl fault) show a single fault core with highly localized deformation (Chester & Chester, 1998). Furthermore, a major fault is surrounded by numerous subsidiary faults (Scholz, 2019). Because these faults are interconnected forming a fault zone (Ben-Zion & Sammis, 2003), defining an individual fault may be ambiguous.

1.1.2. Fault geometry at depth

Unlike the surface fault trace, we cannot directly assess the geometry of faults in the subsurface where natural earthquakes nucleate. It is an important question to what extent the fault geometry at the surface is consistent with that at depth since many modeling studies are built on the knowledge from surface traces. Also, the 3D structure of fault zones cannot be fully characterized by observations at the ground surface. Hence, techniques imaging the subsurface fault geometries are critically important, and several techniques using seismic waves have been developed.

Seismic wave gives the information of faults at depth. Seismic images using active sources can identify dip-slip faults from the discontinuity of reflection surfaces (Sato et al., 2005; Wu et al., 2019). For example, megathrust seamounts and splay faults has been imaged by seismic reflections (Kodaira et al., 2000; Moore et al., 2007). In addition, seismic reflections for continental faults often indicate “flower-structures”, bifurcations of a fault plane toward the earth surface (Harding, 1985; Huang & Liu, 2017). This observation raises the possibility that the fault geometry is simpler, and deformation is more localized toward seismogenic depth. Mechanical models also support the delocalization of deformation in shallower depths (Kaneko & Fialko, 2011).

The slip rate of the fault can also be estimated from the deposited sediments during faulting, a technique referred to as growth strata (Yeats et al., 1997). Additionally, the dip angle of faults deeper than the observational limit by seismic reflections can be determined by the method referred to as balance cross sections (Dahlstrom, 1969).

Meanwhile, high-resolution hypocenter distribution of earthquakes using relative location methods such as hypoDD (Waldhauser & Ellsworth, 2000) reveals planar clusters of seismicity (e.g., Kato et al., 2021). The planar structure of seismicity is interpreted as a fault surface (**Chapter 3**). The focal mechanisms also have information on the fault orientations (Fukuyama et al., 2003). Additionally, machine learning-based earthquake detection and location are rapidly growing. For example, recent high-resolution locations of seismicity using machine learning techniques illuminate a 3D imbricated fault system hosting a fluid-driven seismic swarm (Ross, Cochran, et al., 2019).

1.1.3. Mechanics of nonplanar faults

Here, we review the mechanics of nonplanar faults in the framework of continuum elasticity. Under a uniform stress field, the closeness of a fault to the Mohr-Coulomb failure condition is a unique function of its orientation since the shear and normal stresses are functions of the orientation of their plane. Therefore, the closeness to failure and the potential to generate slip are heterogeneous along a nonplanar fault trace. This consideration leads to the idea that asperity (locations producing higher slip during an earthquake) and barrier (locations hindering earthquake rupture propagations) are partly associated with local fault orientations. In fact, dynamic rupture simulations using nonplanar fault geometries reproduce rupture termination around locations unfavorably oriented to the regional stress field (Ando & Kaneko, 2018; Fang & Dunham, 2013). Furthermore, recent analyses of major earthquakes provided evidence for the correlation between local faults' orientation and rupture behaviors (Hamling et al., 2017; Okuwaki et al., 2020; Ross, Idini, et al., 2019).

However, the assumption of a spatially uniform stress field in their models is questionable. The difference in the focal mechanisms of nearby events suggests stress heterogeneity at a small spatial scale. Mechanically speaking, slip on a nonplanar fault causes spatially heterogeneous stresses on its neighbor (Chester & Chester, 2000; Dieterich & Smith, 2009; Dunham et al., 2011b; Romanet et al., 2020; Sagy & Lyakhovsky, 2019). The heterogeneous stress field due to slip on a nonplanar fault can also be inferred from field observations. For example, Griffith et al. (2010) reported that pseudotachylyte is concentrated in restraining bends, suggesting high frictional heats due to high normal stresses.

Recent advances of numerical simulations of dynamic ruptures and earthquake sequences on nonplanar faults enable us to study the role of fault geometry in the framework of elastodynamics and friction. These studies show that all types of geometrical complexity of a fault affect the dynamic and slip pattern in an earthquake (Bruhat et al., 2020; Harris & Day, 1999; Kame et al., 2003; Kase & Day, 2006; Romanet & Ozawa, 2021). In particular, the effect of fault roughness has been studied in recent years. High-frequency radiation is enhanced by fault roughness because of the change of fault strikes (Dunham et al., 2011b; Shi & Day, 2013). Zielke et al. (2017) showed that stress drop decreases with increasing fault roughness. Tal & Hager (2018b) obtained a similar result with earthquake sequence simulations on a rough fault. On a rough fault, there is an additional resistance to slip, which is referred to as roughness drag (Fang & Dunham, 2013). Roughness drag is known to suppress dynamic slip and enhance aseismic slip (Ozawa et al., 2019; Tal et al., 2018).

1.2. Earthquake sequence modeling using rate and sate dependent friction laws

The use of a rate and state-dependent friction law (RSF law) is the mainstream in earthquake source physics over the last 40 years. In this section, we review the application of the rate and state friction law to earthquake source physics.

1.2.1. The rate and state dependent friction law

Faults slowly accumulate elastic strain due to tectonic processes and rapidly release the elastic strain as an earthquake when the shear stress overcomes the frictional strength of rock. For active faults, this process repeatedly occurs over a geologic time scale. The stick-slip behavior seen in lab experiments is an analog of earthquakes (Brace & Byerlee, 1966), which is closely related to the nature of friction on the interface. Hence, a better understanding of rock friction is key to understanding the mechanics of earthquakes.

The rate and state friction law unifies the classical static and dynamic friction in a single framework. Laboratory experiments discovered the following natures for rock friction.

Observation 1: The steady-state friction (constant friction coefficient attained after sliding a long time with a fixed slip velocity) is a function of the slip velocity and has a logarithmic dependence on the slip rate.

Observation 2: The static friction increases with the logarithm of the contact (zero slip rate) time (log-*t* healing (Dieterich, 1972)).

Observation 3: If the sliding velocity jumps from a steady-state, there is an instantaneous jump in friction, which is followed by relaxation toward a new steady state. A characteristic slip distance that is independent of the slip velocity characterizes the relaxation process (Dieterich, 1978).

Based on these observations, Dieterich (1979) and Ruina (1983) formulated the so-called RSF law. The RSF law accounts for the memory effects (the history of the slip rate) using a state variable θ. The friction coefficient is expressed as

$$\mu(V,\theta) = \mu_0 + a\log\left(\frac{V}{V_0}\right) + b\log\left(\frac{\theta V_0}{d_c}\right).$$

The second term is called the direct effect, which corresponds to the instantaneous effect of a step-like change of sliding velocity (**Observation 3**). The parameter a characterizes the direct effect. The third term characterized by parameter b is called the evolution effect, corresponding to the relaxation of the steady-state. There are two types of widely used evolution laws for θ.

$$\frac{d\theta}{dt} = 1 - \frac{V\theta}{d_c} \text{ (aging law)},$$

$$\frac{d\theta}{dt} = -\frac{V\theta}{d_c}\log\left(\frac{V\theta}{d_c}\right) \text{ (slip law)}.$$

In the aging law, the first term of the right hand side indicates log-t frictional healing with time (**Observation 2**) since $\theta = t$ in stationary contact ($V = 0$). The second term indicates the slip-weakening process, although its prediction of the slip-weakening process does not completely agree with **Observation 3**. In the slip law, the behavior of the slip-weakening process matches **Observation 3**, but the frictional healing does not take place in stationary contact (**Observation 2**). Thus, neither of them can reproduce all of **Observation 1-3,** which leads to the proposal of other formulations of the RSF law (Barbot, 2019a; Kato & Tullis, 2001; Nagata et al., 2012).

The steady-state is defined as no state evolution, so that, $\theta_{ss} = d_c/V$. Hence, both evolution laws lead to the steady-state friction coefficient as

$$\mu_{ss}(V) = \mu_0 + (a-b)\log\left(\frac{V}{V_0}\right).$$

We confirm that the logarithmic-velocity dependence of steady-state friction is recovered (**Observation 1**).

In a microphysical sense, the RSF law is interpreted as the thermally activated creep of real contact areas (Heslot et al., 1994; Nakatani, 2001). Dieterich (1979) noted that the state variable θ corresponds to the average contact time of asperities. Several authors derived the RSF law from microphysical modeling (Aharonov & Scholz, 2018; Barbot, 2019a; Chen et al., 2017; Perfettini & Molinari, 2017), but we do not focus on the detail here.

The RSF law does not hold at higher slip velocity (> cm/s). High-velocity friction experiments have consistently shown that the friction coefficient exhibit a rapid decrease toward 1 m/s slip velocity (di Toro et al., 2011). Several mechanisms have been proposed to explain this dynamic weakening, including flash heating of asperities (Beeler et al., 2008; Rice, 2006), thermal pressurization of pore fluids (Lachenbruch, 1980; Rice, 2006), melting due to frictional heat (Hirose & Shimamoto, 2005), and nanoparticle lubrications (Han et al., 2011). Although the limitation of the RSF law at high slip velocities is evident today, the RSF law is still used at whole slip velocities in the numerical modeling of earthquake cycles (reviewed in section 1.2.3). This is partly because the RSF law is often used, and the use of the RSF law enhances comparisons to other studies. Also, despite the issue of high slip rates, there is some observational evidence suggesting that natural faults are governed by the RSF law. Several authors succeeded in quantitatively reproducing observed fault slip history using the RSF law (Larochelle et al. 2021). They also estimated the in-situ values of constitutive parameters of the RSF law. However, it should be noted that the success of the RSF law does not exclude the possibility that other friction laws better describe fault sliding (Lieou et al., 2017; van den Ende et al., 2018).

1.2.2. Application of the RSF law to earthquake physics

The RSF law has ingredients that are necessary to reproduce stick-slip. First, the slip weakening process at the onset of rapid slip allows for stress drop, which is necessary for driving rupture propagation. Second, frictional healing after the dynamic slip stops enables repeating ruptures in a single fault. In fact, it is a widespread idea that stick-slip and earthquakes are interpreted as frictional instability.

The simplest model of stick-slip is the spring-slider model, in which a block that obeys the RSF law is pulled by a constant speed via a spring with stiffness k. Obviously, the system has a steady-state behavior in which the block slides at the load point velocity. We consider the stability of the steady-state, which is a small perturbation to this steady-state grows or decays. Linear stability analysis for this system reveals that when $a - b > 0$ (steady-state velocity-strengthening), the system is stable and the block slides with the load point velocity. When $a - b < 0$ (steady-state velocity-weakening), the system is unstable and capable of producing stick-slip under the following condition (Ruina, 1983):

$$k < k_c = \frac{(b-a)\sigma}{d_c}.$$

Otherwise, the system is stable. This is so-called a Hopf bifurcation in terms of nonlinear dynamics. If the system is near critical ($k \sim k_c$), slow stick-slip appears (Leeman et al., 2016; Liu & Rice, 2007).

In continuum elasticity (2D antiplane shear), the minimum wavelength of perturbation that eventually results in unstable slip is given by Rice & Ruina (1983)

$$\lambda_c = \frac{\pi G d_c}{(b-a)\sigma}.$$

This characteristic length scale arising from the RSF law and elastic properties is fundamental in the sense that this determines the minimum earthquake size on a given fault, although the linear stability analysis is no longer directly applicable to earthquake slip. Nonlinear analyses and numerical simulations of the RSF law predict how slip instability evolves to dynamic crack propagation, which is called the earthquake nucleation process (Dieterich, 1992). There is a significant discrepancy in the earthquake nucleation process between the aging law and slip law (Ampuero & Rubin, 2008).

Dieterich (1992) theoretically studied the earthquake nucleation process governed by the

RSF law. He derived the analytical solution of the time of instability (time reaching divergence of the slip rate) as

$$t_c = \frac{a\sigma}{\dot{\tau}} \ln\left(\frac{\dot{\tau}}{H\sigma V_0} + 1\right),$$

where V_0 is the initial slip rate, $\dot{\tau}$ is the shear stressing rate, and $H = -\frac{k}{\sigma} + \frac{b}{d_c}$. This relationship between the slip rate and time to instability leads to an equation that relates the loading history of collective faults and the temporal evolution of seismicity rate in the system (Dieterich, 1994). Using this equation with the assumption of a step-like increase of the shear stress, the Omori-Utsu law for aftershocks can be derived (see **Chapter 3** for the details). This equation is also applied to a seismicity modulation in response to tidal stresses (Ader et al., 2014; Heimisson & Avouac, 2020).

The value of $a - b$ is particularly important because it determines the seismogenesis of a given location on the fault. It is well established that $a - b$ primarily depends on the temperature (Blanpied et al., 1995; Chester, 1994; den Hartog et al., 2012). For example, the depth distribution of hypocenter and locking of faults can be explained by the temperature dependence of $a - b$ given the temperature gradient with depth (Scholz, 1998). For example, in the continental crust, earthquakes occur at temperatures between 100 and 300 ºC (Sibson, 1983) and quartz gouge exhibits velocity-weakening behavior between temperatures 100 and 350 ºC (Chester & Higgs, 1992). The value of $a - b$ also depends on composition, normal stresses, pore fluid pressure, cumulative displacement, lithification state, and loading rates (Marone, 1998)

1.2.3. Modern earthquake sequence (cycle) simulations

Based on the RSF law and continuum elasticity, the entire earthquake cycle (from the stress accumulation due to tectonic loading to nucleation and dynamic rupture) on a given fault can be simulated. Tse & Rice (1986) is the first to solve the spatiotemporal slip evolution of a fault embedded in an elastostatic medium using the boundary element method (BEM). The inertia term was neglected in his model. By varying the friction parameter with depth in a manner consistent with laboratory results at different temperatures, they demonstrated periodic ruptures in the upper crust, stable creep in the lower crust, and the transitional behavior in between them. Expansion of ruptures reproduced in the simulation take the form of a propagating crack, qualitatively similar to the dynamic rupture process predicted by slip-weakening friction (Andrews, 1976). The model was also successful in reproducing afterslip below the seismogenic zone using velocity-strengthening frictional behavior.

The computational method of this model has been refined by many researchers. The original Tse & Rice (1986) model uses an artificial friction law to avoid the divergence of slip rate during the seismic slip, although what in reality bounds the slip rate is the inertia effect (instead of frictional properties). Rice (1993) introduced a radiation damping term that approximates the energy radiated from the seismic wave, limiting the slip rate during seismic slip without introducing a generic friction law. This technique is now widely used as "quasi-dynamic simulation", especially for exploring the effect of spatially nonuniform frictional properties (Cattania & Segall, 2019; Dublanchet et al., 2013; Hillers et al., 2006; Hori & Miyazaki, 2011; Kato, 2016; Yabe & Ide, 2017).

The use of quasi-dynamic (QD) approximation allows for a significant reduction in computational costs, although it is known that some differences from the true solution cannot be avoided (Duru et al., 2019; Lapusta & Liu, 2009; Thomas et al., 2014). In general, the QD approach underestimates the rupture speed and the peak slip rate compared with the true solution. One should not use quasi-dynamic approximation when investigating the rupture dynamics and ground motion of each event. Rigorous treatment of elastodynamic stress transfer for earthquake sequence simulations requires huge computational costs. Lapusta et al. (2000) developed a fully-dynamic but computationally efficient technique, called the spectra boundary integral equation method (SBIEM). This method utilizes an analytically expressed integration kernel (Geubelle & Rice, 1995) in the wavenumber domain to allow for the use of adaptive time-stepping and wavenumber-dependent truncation of time convolution. Lapusta & Liu (2009) extended it into a 3D vertical strike-slip fault. Although this method is only rigorously applicable to a planar fault due to the assumption of translational symmetry, Romanet & Ozawa (2021) recently extended the SBIEM into a weakly nonplanar fault. Also, Miyake & Noda (2019) extended SBIEM into a Maxwell viscoelastic medium for the 2D antiplane shear problem using a memory variable technique. Taking advantage of the fully-dynamic nature, SBIEM has revealed a variety of aspects of earthquake physics (Jiang & Lapusta, 2016; Kaneko et al., 2010; Lambert et al., 2021; Noda & Lapusta, 2013).

The boundary element method in the real space with quasi-dynamic approximation (hereafter, QD-BEM) is often used including this thesis. This method can account for nonplanar and complex fault geometries, which is impossible with SBIEM. QD-BEM also has several computationally efficient techniques, such as the fast multiple method and H-matrices (**Chapter 2**). QD-BEM has been used for stepover geometry (Romanet et al., 2018), fault bends (Ong et al., 2019; Sathiakumar et al., 2020), fractally rough faults (Cattania & Segall, 2021; Heimisson, 2020; Ozawa et al., 2019). Recently, 3D QD-BEM simulations targeted to real-world faults have also been performed (Galvez et al., 2020; Hori et al., 2004; Li & Liu, 2021; Ohtani et al., 2014; Yu et al., 2018).

Although QD-BEM has advantages in the flexibility of fault geometry and computational efficiency, it is difficult to account for elastic heterogeneity (such as sedimentary basins, fault damage zones) and distributed inelastic deformations (such as viscosity of asthenosphere and plastic yielding). Hence, some researchers develop volume discretized methods to account for more complex rheological properties in the bulk. Erickson & Dunham (2014) developed a finite-difference method (FDM) for earthquake cycle simulations for a vertical strike-slip fault. They explored the effect of a compliant sedimentary basin on the earthquake cycle. Their method was applied to several problems, including bimaterial problems (Erickson & Day, 2016), off-fault viscoplasticity (Erickson et al., 2017), power-law viscoelasticity (Allison & Dunham, 2018), and along-fault diffusion of pore fluid (Zhu et al., 2020). Meanwhile, Kaneko et al. (2011) developed a spectra element method (SEM) for fully-dynamic earthquake cycles and used it to explore the effect of shallow sedimentary layers. The same method was recently applied to low-velocity fault damage zones (Thakur et al., 2020), although SBIEM can also handle this problem setting in the quasidynamic case (Idini & Ampuero, 2020). Liu et al. (2020) developed 3D finite element method (FEM) for fully-dynamic earthquake sequence simulations for a branching strike-slip fault. Tal developed a 2D mortar finite-element method for earthquake sequence simulations that is applicable to nonplanar faults and off-fault plastic deformation (Tal, Goebel, et al., 2020; Tal & Hager, 2018a). Since shear deformation is thought to be not localized into a mathematical (i.e., zero thickness) plane but diffused below the seismogenic zone, some modelers attempt to allow for finite width deformation, using an invariant form of the RSF law (Behr et al., 2021; Herrendörfer et al., 2018).

Volume discretization methods suffer from the truncation error due to the finite computational domain. Some modelers attempt to combine volumetric and boundary methods. Abdelmeguid et al. (2019) used a hybrid method of SBIEM and FEM to compute earthquake cycles with elastic heterogeneity. Their hybrid method discretizes the fault zone (i.e., locations where all complex things occur) with finite elements and uses SBIEM for outside of the fault zone. Owing to the use of SBIEM, the method does not suffer from the truncation error of the computational domain. On the other hand, Barbot and others developed another method that accounts for viscoelastic deformation in the bulk. In addition to the slip of the fault surface with boundary elements, they implement bulk creep using an integral equation for volume discretized elements (Barbot, 2018; Lambert & Barbot, 2016; Q. Shi et al., 2020).

We summarize the strength and weakness of each numerical method. SBIEM is computationally highly efficient especially for fully-dynamic simulations, however cannot handle nonplanar faults and elastic heterogeneity. BEM is highly flexible to fault geometry but has difficulty in incorporating bulk non-linear rheology and elastic heterogeneity (although it is possible in principle). Volume discretized methods (FDM/FEM/SEM) can allow for complex off-fault rheology but are usually computationally more expensive and suffer from the truncation error of the computational domain (Jiang et al., 2021). A recent cross-validation project of computational codes illuminated agreements and discrepancies between different numerical methods (Erickson et al., 2020; Jiang et al., 2021). See also Appendix B.

2. Large-scale earthquake sequence simulations of geometrically complex faults using the boundary element method accelerated by lattice H-matrices

This chapter has been submitted as "Large-scale earthquake sequence simulations of geometrically complex faults using the boundary element method accelerated by lattice H-matrices in distributed memory systems" to Journal of Computational Physics (Ozawa et al., 2021).

2.1. Introduction

Earthquake sequence simulations using rate and state friction laws originate from Tse & Rice (1986) and Rice (1993). Several researchers now use earthquake sequence simulations to understand how faults behave under various conditions and how different model ingredients (e.g., fault rheology) influence an earthquake sequence (Erickson et al., 2020). Among various computational methods, the boundary element method (BEM) is often used because of its ease in handling complex fault geometries (Hori et al., 2004; Ohtani et al., 2014; Qiu et al., 2016; Thompson & Meade, 2019; Yu et al., 2018), although different methods were also developed (Liu et al., 2020).

A major challenge in earthquake sequence simulations is their computational cost. To simulate smaller earthquakes, the size of each element must be smaller, which increases the number of elements N. In 3D simulations (2D fault in 3D space), if the characteristic element size is reduced by a factor of 2, the increase in N is a factor of 4. In the original BEM, the computational cost for each time step scales with $O(N^2)$, where N is the number of discretized elements. This is because multiplications of a dense matrix and a vector (slip rate distribution) are necessary to evaluate the stress change on each element at every time step. Furthermore, the time step width must be small if we use small elements, which increases the repetition of matrix-vector multiplications. Thus, the computational cost increases rapidly with a decrease in the element size.

Several methods have reduced the complexity of $O(N^2)$ to $O(N\log N)$. The fast Fourier transform (FFT) method is often used for this purpose (Kato, 2003; Lapusta & Liu, 2009), but is limited to planar faults due to the assumption of translational symmetry. FFT also cannot process non-vertical faults. The use of hierarchical matrices (H-matrices) originally developed by Hackbusch (1999) is an alternative that can be used for general fault geometries. Ohtani et al. (2011) showed a significant acceleration in earthquake cycle simulations with H-matrices, and it is now common to use H-matrices in BEM-based quasi-dynamic earthquake sequence simulations (Galvez et al., 2020; Heimisson, 2020; Hyodo et al., 2016; Ohtani et al., 2014; Romanet, 2017). For example, Hyodo et al. (2016) performed earthquake sequence simulations in the Nankai trough megathrust using ~300,000 elements. H-matrices have also recently been used in dynamic rupture simulations (Sato & Ando, 2021).

Parallel scalability is also important in computations using supercomputers. Owing to the increase in MPI communication costs and load imbalance, the parallel speed increase is generally less than the expectation from the ideal linear scalability. Ida et al. (2014) showed that the computational speed of an H-matrix-vector multiplication saturates <100 cores in the Poisson equation of the $N\sim 100{,}000$ problem. Thus, we could not efficiently use a large number of cores in the H-matrices.

As a solution to this problem, Ida (2018) proposed the lattice H-matrices. The lattice H-matrices contain convenient structures to construct an efficient communication pattern compared with the normal H-matrices while maintaining the $O(N\log N)$ memory compression. In addition, a relatively adequate load balance is maintained in the case of lattice H-matrices, even if a large number of MPI processes are used. This method reduces the load imbalance and communication cost between MPI processes and improves parallel scalability, and it has been applied to micromagnetic simulations (Ida et al., 2020).

2.2. Method of earthquake sequence simulations on nonplanar faults

2.2.1. Boundary Element Method

We use the boundary element method (BEM) (M. Bonnet, 1999). In BEM, the shear stress change $\Delta\tau$ and normal stress change $\Delta\sigma$ are represented as the integral of the kernel function multiplied by the slip distribution on the fault surface:

$$\Delta\tau(\boldsymbol{x}) = \int K_{shear}(\boldsymbol{x}, \boldsymbol{\xi})\Delta u(\boldsymbol{\xi})dS(\boldsymbol{\xi}), \tag{2.1}$$

$$\Delta\sigma(\boldsymbol{x}) = \int K_{normal}(\boldsymbol{x}, \boldsymbol{\xi})\Delta u(\boldsymbol{\xi})dS(\boldsymbol{\xi}), \tag{2.2}$$

where K_{shear} and K_{normal} are elastostatic Green's functions, and Δu is the slip distribution.

To numerically calculate equations (2.1-2.2), we divide the fault surface into N elements and denote the index set as $I = \{1, \dots, N\}$. The shapes of the elements are either rectangular or triangular. In a discretized form using step functions as the base functions, the stress changes on the i-th element are represented as:

$$\Delta\tau_i = \sum_j^N A_{ij}D_j\,, \tag{2.3}$$

$$\Delta\sigma_i = \sum_j^N B_{ij}D_j\,. \tag{2.4}$$

where $D \in \mathbb{R}^N$, A, and B $\in \mathbb{R}^{N\times N}$ are dense matrices. The entries of A and B are calculated using the techniques of elastic dislocation theory. We use Nikkhoo & Walter (2015) and Okada (1992) for triangular and rectangular elements, respectively. The evaluation point of the stress component is the center of each element.

Triangular unstructured elements have more flexibility in fault geometry than rectangular elements. However, Barall & Tullis (2016) found that rectangles outperform triangles in terms of the accuracy of the stress value. Therefore, rectangular elements should be used as much as possible.

Notably, the normal stress change has often been neglected in several previous earthquake sequence simulations, unlike in single-event dynamic rupture simulations. Normal stress changes originate from broken symmetries such as nonplanar faults, free surfaces, and material heterogeneities. We will show the effects of normal stress changes on the earthquake cycle in a later section.

2.2.2. Governing Equations

The boundary condition of each element is governed by the regularized rate and state friction law (Dieterich, 1979; Ruina, 1983). Following Rice et al. (2001), the shear and normal tractions at each element are related as follows:

$$\frac{\tau_i}{\sigma_i} = a\mathrm{arcsinh}\left(\frac{V_i}{2V_0}e^{-\phi_i}\right), \tag{2.5}$$

where $V_i(t) = \frac{dD_i}{dt}$ is the slip rate, $\phi_i(t)$ is the state variable, a is the coefficient of the direct effect, and V_0 is the reference slip rate.

The evolution law for the state variable is given by the aging law (Dieterich, 1979; Ruina, 1983):

$$\frac{d\phi_i}{dt} = \frac{b}{d_c}\left[V_0 \exp\left(\frac{f_0 - \phi_i}{b}\right) - V_i\right], \tag{2.6}$$

where f_0 is the reference friction coefficient, b is the coefficient of the evolution effect, and d_c is the characteristic slip distance. Using the stiffness matrix calculated in the previous section, the shear and normal stress changes are given as follows:

$$\frac{d\tau_i}{dt} = \sum_j^N A_{ij}V_j + \dot{\tau}_i - \frac{\mu}{2C_s}\frac{dV_i}{dt}, \tag{2.7}$$

$$\frac{d\sigma_i}{dt} = \sum_j^N B_{ij}V_j + \dot{\sigma}_i, \tag{2.8}$$

where μ is the rigidity, c_s is the S wave speed, $\dot{\tau}_i$ and $\dot{\sigma}_i$ are the tectonic loading rates for shear and normal stresses on the i-th element, respectively. The first terms in both equations (2.7-2.8) represent the stress rates caused by slip (time derivative of equations (2.3-2.4)). The third term for the shear stress is radiation damping, which is an approximation of inertia (Rice, 1993). Earthquake sequence simulations using this approximation are "quasi-dynamic," and the effect of this approximation has been explored in previous studies (e.g., Lapusta & Liu, 2009).

We eliminate dV_i/dt from equation (2.7) using the total derivative of V:

$$\frac{dV_i}{dt} = \frac{\partial V_i}{\partial \tau_i}\frac{d\tau_i}{dt} + \frac{\partial V_i}{\partial \sigma_i}\frac{d\sigma_i}{dt} + \frac{\partial V_i}{\partial \phi_i}\frac{d\phi_i}{dt}, \tag{2.9}$$

so that:

$$\frac{d\tau_i}{dt} = \left(1 + \frac{\mu}{2c_s}\frac{\partial V_i}{\partial \tau_i}\right)^{-1}\left[\sum_j^N S_{ij}V_j + \dot{\tau}_i - \frac{\mu}{2c_s}\left(\frac{\partial V_i}{\partial \sigma_i}\frac{d\sigma_i}{dt_i} + \frac{\partial V_i}{\partial \phi_i}\frac{d\phi_i}{dt}\right)\right], \tag{2.10}$$

where the partial derivatives are (from equation (2.5)):

$$\frac{\partial V_i}{\partial \tau_i} = \frac{2V_0}{a\sigma_i}e^{-\phi_i}\cosh\left(\frac{\tau_i}{a\sigma_i}\right), \tag{2.11A}$$

$$\frac{\partial V_i}{\partial \sigma_i} = -\frac{2V_0\tau_i}{a\sigma_i^2}e^{-\phi_i}\cosh\left(\frac{\tau_i}{a\sigma_i}\right), \tag{2.11B}$$

$$\frac{\partial V_i}{\partial \phi_i} = -\frac{2V_0}{a}e^{-\phi_i}\sinh\left(\frac{\tau_i}{a\sigma_i}\right). \tag{2.11C}$$

2.2.3. Time Integration scheme

Based on equations (2.6), (2.8), and (2.10), we solve a $3N$ set of ordinary differential equations (ODEs) $\frac{dy}{dt} = f(\boldsymbol{y})$ where $\boldsymbol{y} = (\phi_1, \dots, \phi_N, \tau_1, \dots \tau_N, \sigma_1, \dots, \sigma_N)$ using the Runge-Kutta method with adaptive time-stepping (Press et al., 2007). We compute $y(t + \Delta t)$ with 5th order accuracy. See Fig. 2.1 for details. If the maximum value of the relative difference between the 4th and 5th solutions is larger than the allowance ε_{RK}, we retry the time integration as follows:

$$\Delta t_{new} = \max\left(\frac{\Delta t_{try}}{2}, \qquad 0.9\Delta \mathrm{t}_{try}{\varepsilon_{RK}}^{-0.25}\right) \tag{2.12}$$

If the error is below the threshold, we update the variables and calculate the next time step using the following formula:

$$\Delta t_{new} = \min\left(2\Delta t_{try}, \qquad 0.9\Delta \mathrm{t}_{try}{\varepsilon_{RK}}^{-0.2}\right). \tag{2.13}$$

As a result, the time step is approximately inversely proportional to the maximum slip rate. This property results from the displacement in each time step having to be smaller than the characteristic state evolution distance. Lapusta et al. (2000) and many other studies explicitly adapted inverse-slip rate time-step widths based on stability analyses. The resultant Δt weakly decreases with decreasing the element size if other parameters are identical.

The slip is thus updated as follows:

$$D_i(t + \Delta t) = D_i(t) + \frac{\Delta t}{2}\left(V_i(t) + V_i(t + \Delta t)\right). \tag{2.14}$$

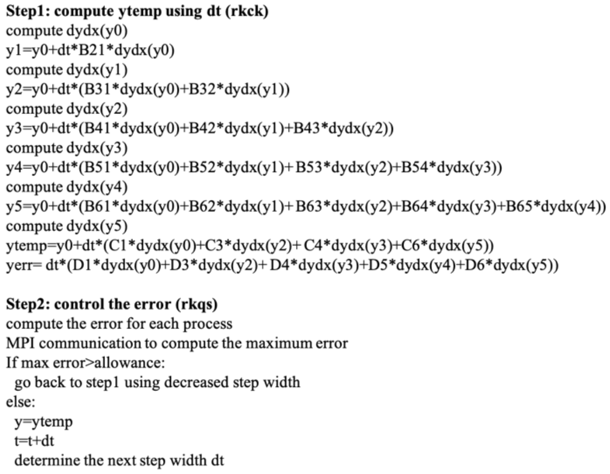

```
Step1: compute ytemp using dt (rkck)
compute dydx(y0)
y1=y0+dt*B21*dydx(y0)
compute dydx(y1)
y2=y0+dt*(B31*dydx(y0)+B32*dydx(y1))
compute dydx(y2)
y3=y0+dt*(B41*dydx(y0)+B42*dydx(y1)+B43*dydx(y2))
compute dydx(y3)
y4=y0+dt*(B51*dydx(y0)+B52*dydx(y1)+B53*dydx(y2)+B54*dydx(y3))
compute dydx(y4)
y5=y0+dt*(B61*dydx(y0)+B62*dydx(y1)+B63*dydx(y2)+B64*dydx(y3)+B65*dydx(y4))
compute dydx(y5)
ytemp=y0+dt*(C1*dydx(y0)+C3*dydx(y2)+C4*dydx(y3)+C6*dydx(y5))
yerr= dt*(D1*dydx(y0)+D3*dydx(y2)+D4*dydx(y3)+D5*dydx(y4)+D6*dydx(y5))

Step2: control the error (rkqs)
compute the error for each process
MPI communication to compute the maximum error
If max error>allowance:
  go back to step1 using decreased step width
else:
  y=ytemp
  t=t+dt
  determine the next step width dt
```

Figure 2.1. Algorithm of the Runge-Kutta method with an adaptive step size (Press et al. 2007). The function dydx, which appears six times, includes two matrix-vector multiplications (equations (2.7) and (2.8)).

2.3. H-matrices

H-matrices are an efficient method to compress the memory of the dense matrix derived from the integral operator (Hackbusch, 1999). The 3D elastostatic kernel exhibits $|\boldsymbol{x}-\boldsymbol{\xi}|^{-3}$ decay, and this kernel function can locally degenerate for a distant source and receiver points ($K(\boldsymbol{x},\boldsymbol{\xi})\sim\sum_k g_k(\boldsymbol{x})h_k(\boldsymbol{\xi})$). This allows for constructing H-matrices for dense matrices A and B in equations (2.3-2.4) for typical mesh geometries.

2.3.1. Construction of H-matrix

The construction of a H-matrix consists of the following steps (Borm et al., 2006). First, we construct a binary cluster tree for the set of triangular or rectangular elements using the (x,y,z) coordinates of their centers. We denote a cluster set as Ω_i $(i=1,\dots,N_\Omega)$. We set the minimum cluster size to 15. Then, we construct a partition structure of the matrix using the following admissibility condition:

$$\min\left(diam(\Omega_i), diam(\Omega_j)\right) < \eta\, dist(\Omega_i,\Omega_j) \tag{2.15}$$

where *diam* is the diameter of the cluster and *dist* is the distance between the two clusters. This condition is derived from the ability of the kernel function to approximately degenerate for distant source and receiver points. Typically, we set the parameter $\eta=2$.

Fig. 2.2 shows the partition structure of a square-shaped fault plane divided by triangular meshes. We reorder the index of the elements $I=(1,\dots,N)$ according to the structure of the cluster tree in the construction of the matrix structure. Blocks located at far-diagonal parts tend to be larger than those around diagonal parts because they correspond to the interactions of distant locations, and the admissibility condition is easy to satisfy (see equation (2.15)).

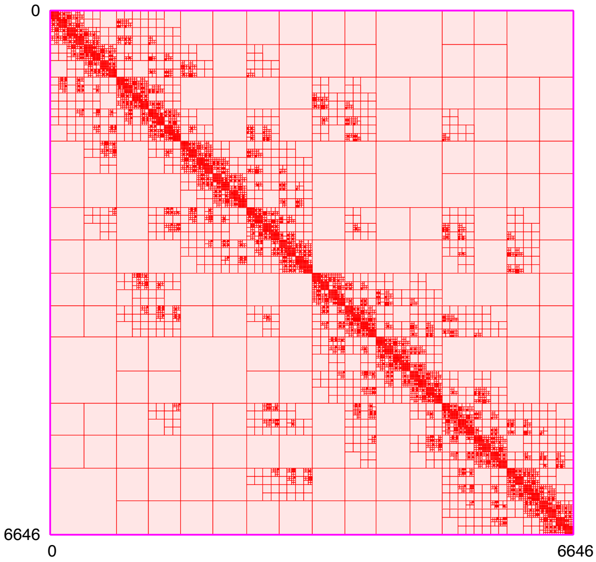

Figure 2.2. Block structures of H matrices (A square-shaped fault using 6646 triangular elements) made by the admissibility condition $\eta = 2$.

Let $L, M \subset I$, and $A_{LM} \in \mathbb{R}^{L\times M}$ be a submatrix of $A \in \mathbb{R}^{N\times N}$. A submatrix A_{LM} is compressed by a low-rank approximation (LRA) if possible; otherwise, we use the dense matrix (full-rank matrix). A low-rank approximated submatrix A_{LM} is represented as follows:

$$A_{ij} \approx \tilde{A}_{ij} = \sum_{k=1}^{r_{LM}} g_{ki} h_{kj}\,, \tag{2.16}$$

Where $g \in \mathbb{R}^{L\times r}, h \in \mathbb{R}^{r\times M}$, and r_{LM} is the rank of the approximated matrix. We apply the adaptive cross approximation (ACA) (Bebendorf, 2000) as the LRA. The rank r_{LM} is controlled by the error tolerance, ε_{ACA};

$$\frac{\left\|A - \tilde{A}\right\|_F}{\|A\|_F} < \varepsilon_{ACA}, \tag{2.17}$$

where F denotes the Frobenius norm. In performing ACA, we use the method proposed by Ida et al. (2015) to prevent the H-matrix from having an excessively large rank.

2.3.2. H-matrix and vector multiplication (HMVM)

A matrix-vector multiplication AV is performed submatrix-wise as follows:

$$\sum_{j}^{|L|} A_{ij} V_j \approx \sum_{j}^{|L|} \sum_{k}^{r_{LM}} g_{ki} h_{kj} V_j = \sum_{k}^{r_{LM}} g_{ki} \left(\sum_{j}^{|L|} h_{kj} V_j \right). \tag{2.18}$$

The original computation using dense matrices requires $O(|L|\ |M|)$, while it becomes $O((|L| + |M|) r_{LM})$ in H matrix-vector multiplication (HMVM). If the rank r_{LM} is much smaller than $min(|L|, |M|)$, the number of operations is significantly reduced. The computation of equation (2.18) results in a part of the vector, and the full vector is obtained by taking the summation of all the submatrix-wise HMVMs.

2.3.3. Parallel Earthquake Sequence Simulation using H-matrices

Our earthquake sequence simulation code is parallelized using a message passing interface (MPI). Submatrices on the H-matrix are assigned to MPI processes, and each MPI process contains a quasi-1D-sliced portion of the entire matrix (Fig. 2.3a). This does not represent a complete 1D slice because a submatrix cannot be separated into multiple MPI processes. For the HMVM, each processor possesses a full slip rate vector, but the resultant stress rate vector comprises a part of the slip rate vector in general. To obtain the full stress-rate vector, each MPI process calls MPI_iSEND and MPI_iRECV by $N_p - 1$ times, where N_p denotes the number of MPI processes. The complexity of the communication cost is $O(NN_p)$. The assignment algorithm is described in detail in (Ida et al., 2014).

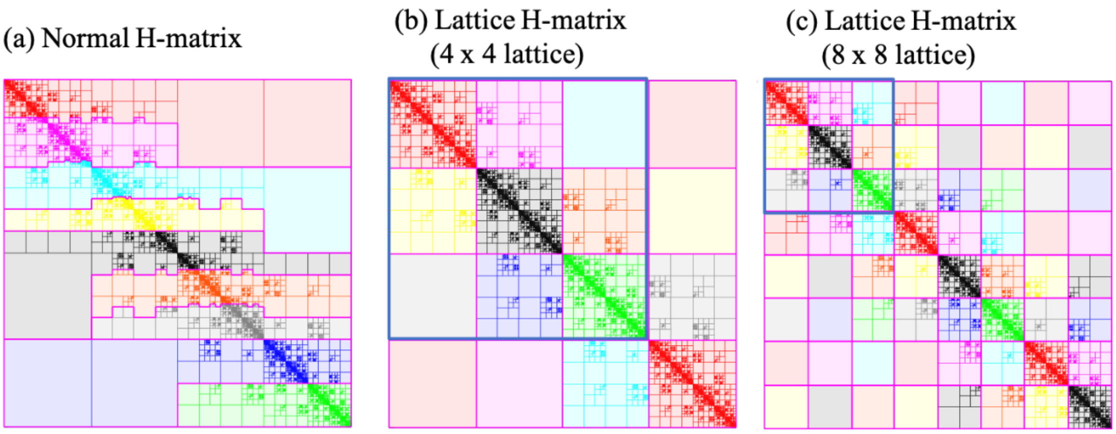

Figure 2.3. Comparison of the block structure and assignments to MPI processes of normal and lattice H matrices. Colors correspond to MPI processes $(N_p = 9)$. (a) is a normal H-matrix. (b) and (c) represent lattice H-matrices using 3 x 3 process grid (shown in blue frames). (b) is a 4 x 4 lattice ($q = 1$) and (c) is an 8 x 8 lattice ($q = 2$).

For $O(N)$ part (element-wise computation), each MPI process is responsible for part of the vector. To construct the full-size vector required for the HMVM, MPI_Allgather is called before the HMVM. To perform a parallel computation of the $O(N)$ part, MPI_Scatter is called after the HMVM. As the number of MPI processes increases, the performance deteriorates owing to the MPI communication costs (both inside and outside the HMVM) in this method.

2.3.4. Lattice H-matrices

As previously explained, earthquake sequence simulations using H-matrices are not suitable for large-scale parallel computations because of the communication cost and load imbalance resulting from their extremely complex structure. To overcome this difficulty, Ida (2018) proposed lattice H-matrices. In this section, we describe the method for earthquake sequence simulations using lattice H-matrices. Hereafter, the H-matrices described in the previous section are referred to as normal H-matrices.

We first construct a cluster tree similar to the normal H-matrices, except for the truncation of the depth L of the cluster tree. We then construct a lattice structure using a truncated cluster tree. Then, an H-matrix is constructed for each lattice block in the same way as the normal H-matrices if it is admissible in terms of equation (2.15). The depth L determines the number of lattice blocks (Figs. 2.3b and 2.3c).

We utilize the lattice structure for assigning MPI processes. This is achieved by introducing a process grid that has N_{pr} rows and N_{pl} columns ($N_{pr} \times N_{pl} = N_p$). We 2D-cyclically array this process grid on the lattice blocks, which means that each MPI process has discontinuous blocks of the matrix (Figs. 2.3b and 2.3c). The number of lattice blocks is determined by the number of MPI processes, which ensures that q process grids are repeated in rows and columns (Figs. 2.3b and 2.3c). This condition gives $L = \lfloor \log_2(\sqrt{N_p} q) \rfloor$ because the binary tree is adopted. In a fixed q, as N_p increases, each lattice becomes smaller. Thus, the entire matrix is divided into a larger number of submatrices, and the memory becomes larger compared with the normal H-matrices. However, in the procedure of HMVM using lattice H-matrices, we significantly reduce the communication traffic compared with the algorithm used in normal H-matrices. After the arithmetic of HMVM (equation (2.18)) assigned to each MPI process, diagonal MPI processes obtain part of the stress rate vector using MPI_Reduce along each row in the process grid, and then send it to other MPI processes in each column in the process grid using MPI_Broadcast. This algorithm, which was first proposed by Ida et al. (2018) for block low-rank matrices, utilizes the lattice structure, and to perform this algorithm, the number of processors must be a squared number (Fig. 2.4). The complexity of the communication costs for the HMVM using lattice H-matrices is $O(N)$ regardless of the number of MPI processes, which is reduced from that of normal H-matrices $O(NN_p)$.

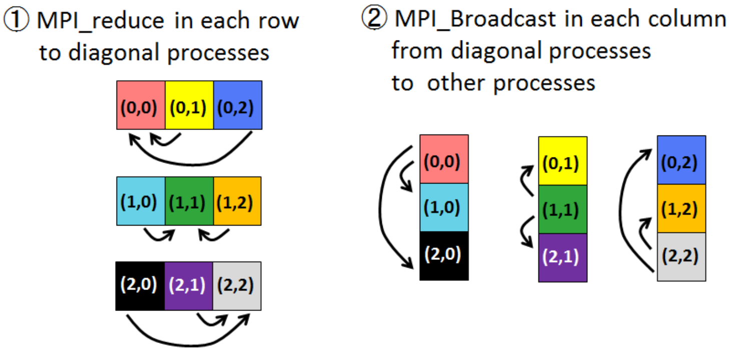

Figure 2.4. Schematic illustration of the algorithm of the MPI communication for HMVM (From Ida, 2018).

The HMVM in the lattice H-matrices requires only a part of the slip rate vector (size ~ $N/\sqrt{N_p}$) for each MPI process. In addition, each MPI process has identical indices of the resultant stress rate vector to the slip rate vector. Furthermore, each MPI process is in charge of the same part of the vector for element-wise computation as the HMVM. Therefore, unlike the normal H-matrix algorithm, MPI communication is not necessary before and after the HMVM. Note that this algorithm performs redundant computations for the element-wise part between $\sqrt{N_p}$ MPI processes. However, HMVM comprises ~90% of the computational time in the case of $O(10^5)$ problems and a few tens of thousands of MPI processes, thus this redundant computation does not deteriorate the overall performance.

In the implementation, we use the open-source library *HACApK* for the construction of H-matrices and HMVM. We validated our code with normal H-matrices using a benchmark problem of a 3D vertical strike-slip fault as defined by the Simulation of Earthquakes and Aseismic Slip (SEAS) project (Jiang et al. 2021).

2.4. Simulation Examples

In this section, we detail a representative earthquake sequence simulation using lattice H-matrices to demonstrate its application capability and error control.

2.4.1. Problem setting

A nonplanar fault is embedded in an elastic half-space, with elastic constants of $c_s =$ 3.464 km/s, $c_p = 6$ km/s, and $\mu = 32.04$ GPa. The fault geometry is shown in Fig. 2.5. The fault is 50 km in the along-strike length and 20 km in the along-dip length. The shallower (30 °dip angle) and deeper (10 °dip angle) parts are smoothly connected. The fault cut the free surface. The mesh is rectangular, and 256,000 elements are used. We fix $b = 0.020$ and vary the a-b values, as shown in Fig. 2.5 in color. We set $a/b = 0.75$ in the velocity-weakening zone. The characteristic slip distance d_c is uniformly set to 0.02 m. The initial normal and shear tractions are uniformly set to 58 MPa and 100 MPa, respectively. For simplicity, we neglect the depth dependence of the initial shear and normal stresses.

To ensure numerical convergence, the following length scale of the breakdown zone must be resolved by at least a few elements (Rubin & Ampuero, 2005)

$$L_b = \frac{\mu d_c}{b\sigma}. \tag{2.19}$$

We set $L_b \sim 5\Delta s$ for the initial (uniform) normal stress, where Δs is the caharacteristic element size. Note that $L_b/\Delta s$ changes with time because of the change in normal stresses. The loading approach is the backslip method with a plate rate $V_{pl} = 10^{-9}$m/s for both the shear and normal stresses (Heimisson, 2020).

$$\dot{\tau}_i = -V_{pl} \sum_j^N S_{ij}\,, \tag{2.20}$$

$$\dot{\sigma}_i = -V_{pl} \sum_j^N N_{ij}\,, \tag{2.21}$$

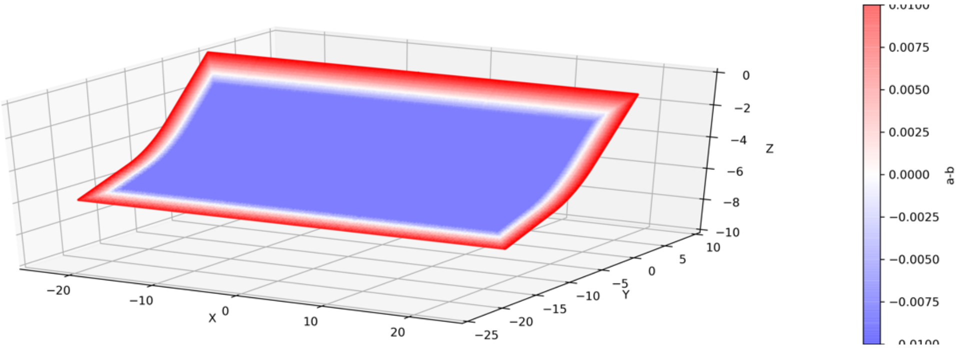

Figure 2.5. Fault geometry used in this study. The fault is 50 km in the along-strike length and 20 km in the along-dip length. There is a bend at dip = 10 km. The dip angle is 30° at the surface and 10° at the bottom. The color indicates the distribution of *a-b* values.

2.4.2. Numerical Results

Fig. 2.6 shows the temporal variation of the cumulative slip distribution on the fault. The earthquake sequence is complex, and partial ruptures and full ruptures occur on the fault. A previous study with a 2D planar fault demonstrated that, in this type of loading, the condition of the occurrence of the partial rupture is $W/h^* \gg 1$, where W is the dimension of the velocity-weakening region and h^* is given by $h^* = \frac{2\mu d_c}{\pi(b-a)\sigma}$ (Cattania, 2019). Otherwise, only full system size ruptures occur. We assume $W/h^*>10$ ($h^* \sim 2$ km and $W > 20$ km), and the condition of partial ruptures is met. We believe that free surface effects and fault bends would also contribute to the complex earthquake sequence by modulating the stress interaction. The purpose of this study is to examine the numerical accuracy, and a detailed discussion on the mechanism is beyond the scope of this study.

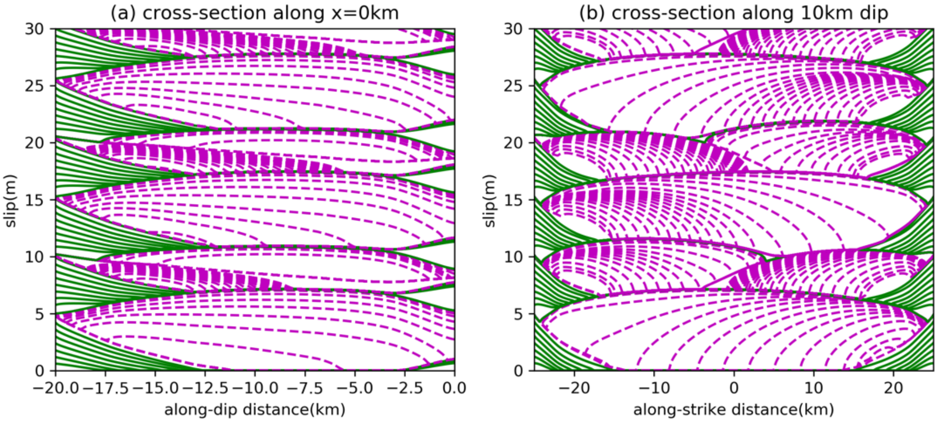

Figure 2.6. Cumulative slip at every 20 years during the interseismic period (green solid lines) and every 5 seconds during the coseismic period (purple dashed lines). (a) cross-section along $x = 0$ km. (b) cross-section along 10 km dip.

2.4.3. Case without normal stress effect

Most earthquake sequence simulations on nonplanar and/or dip-slip faults neglect the effect of normal stress changes (Galvez et al., 2020; Ong et al., 2019). In addition, we ran a simulation without normal stress changes (Fig. 2.7) as a comparison. The observed differences between Figs. 2.6 and 2.7 originate from the two sources of normal stress changes. First, the free surface effect leads to a coseismic normal stress reduction in the shallower part (e.g., Oglesby et al., 2000). Second, the fault curvature leads to a normal stress change that is proportional to the slip (Romanet et al., 2020). However, the coupling between the normal stress and state evolution (Tal, Rubino, et al., 2020), which we neglected, could partly reduce the effect of the normal stress changes.

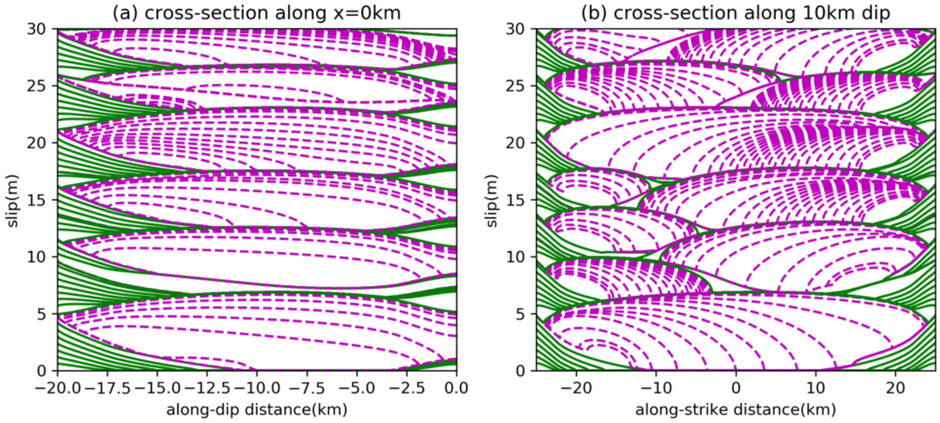

Figure 2.7. Same figure as Figure 2.6 but without considering the normal stress changes.

2.4.4. Effect of accuracy controls

The accuracy of the simulation is controlled by two errors: the low-rank approximation of the H-matrices and the truncation of high-order terms of the Runge-Kutta method. In this section, we explore the effect of error tolerance on the above simulation results with the normal stress change.

Fig. 2.8a shows the results using different error tolerances of the H-matrices. We determine that $\varepsilon_{ACA} = 10^{-4}$ and 10^{-5} show no differences. $\varepsilon_{ACA} = 10^{-3}$ also matches closely with the others in terms of the timing of the event marked by spikes, although a slight difference in the nucleation phase (slow rise before the peak) for the 5th event is identified. In a simulation with $\varepsilon_{ACA} = 10^{-3}$, Ohtani et al. (2011) documented a larger discrepancy in the timing of the event than that observed here. We suspect that the nonuniform d_c distribution (and thus nonuniform $L_b/\Delta s$ distribution) of Ohtani's model may be the cause of this discrepancy.

We also evaluate the effect of ε_{RK} in Fig. 2.8b. Again, $\varepsilon_{RK} = 10^{-4}$ and 10^{-5} show no visible differences. In the case of $\varepsilon_{RK} = 10^{-3}$, the timing of earthquakes does not change, but the maximum slip rate fluctuates during the interseismic period. The number of time steps for 800 years using $\varepsilon_{RK} = 10^{-3}, 10^{-4}$, and 10^{-5} are 28400, 32300, and 42400, respectively.

(a) Error tolerance of H-matrix

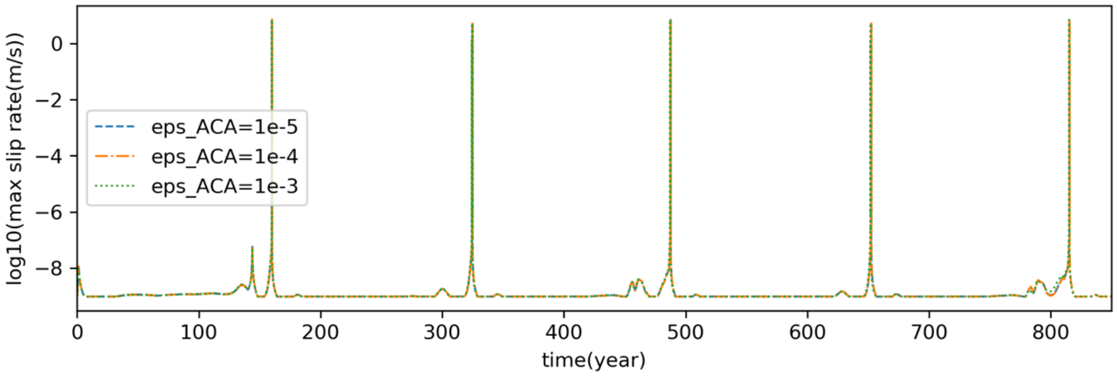

(b) Error tolerance of time integration

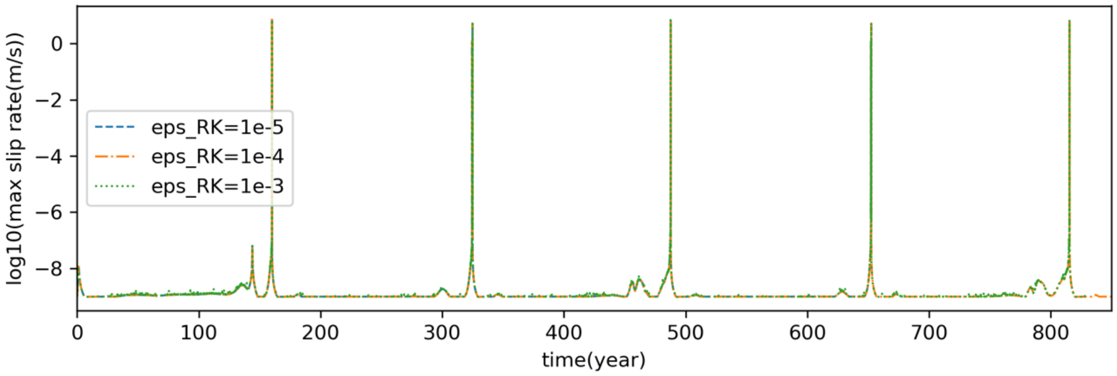

Figure 2.8. Maximum slip rate plotted against time. (a) Effect of the error tolerance of the ACA in constructing a lattice H-matrix and (b) effect of the error tolerance of the Runge-Kutta method.

2.5. Performance and scalability

In this section, we detail the performance and parallel scalability of our simulations. All simulations were performed in Oakforest-PACS(OFP) at the University of Tokyo, which is equipped with an Intel® Xeon Phi ™ 7250 (68 cores, 1.4 GHz) and 96 GB(DDR4) memory in addition to 16 GB(MCDRAM) memory. The OFP system utilizes Intel® Omni-Path for the interconnect network, which has a link throughput of 100 Gbps. We used 64 cores per CPU node. We also used an Intel Fortran compiler with the -O3 optimization option and an Intel MPI Library. All results are flat MPI parallelization. The physical problem setting is described in section 2.4.2.

2.5.1. Memory Usage of H-matrices and Lattice H-matrices

Like Ohtani et al. (2011), we investigate the compression efficiencies of the normal and lattice H-matrices. Fig. 2.9 shows the memory size of the normal H-matrices as a function of the number of elements. We fix the fault geometry and change the element size to vary the number of elements. Fig. 2.9a shows the case for the rectangular elements. We confirm a roughly $O(NlogN)$ dependence on the memory size for both the shear and normal stresses. For shear stresses, the compressibility against the original dense matrix is 8% for $N = 16{,}000$ and 0.7% for $N = 400{,}000$. Shear stresses have systematically larger memories than normal stresses for a given number of elements. However, the memory size also depends on the fault geometry. We also try a planar thrust fault with 30 degree dip angle (i.e. same geometry as the original except the bend) for a comparison. We find 20-30% memory reductions for normal stresses, but shear stresses have little change (Fig. 2.9a). The matrices for nonplanar faults do not simply decay with the distance of the source and receiver around the fault bend, which increases the ranks of part of submatrices. The memory size of normal stresses is more sensitive to the fault geometry because the deviation from planar faults due to the curvature is dominant in normal stresses (Romanet et al. 2020).

We also measure the memory size of the normal H-matrices with the same geometry using triangular unstructured meshes. As shown in Fig. 2.9b, triangular meshes have larger memories than rectangular elements. This is presumably caused by the slightly non-uniform element sizes in unstructured meshes, which lowers the efficiency of the low-rank approximation of the submatrices.

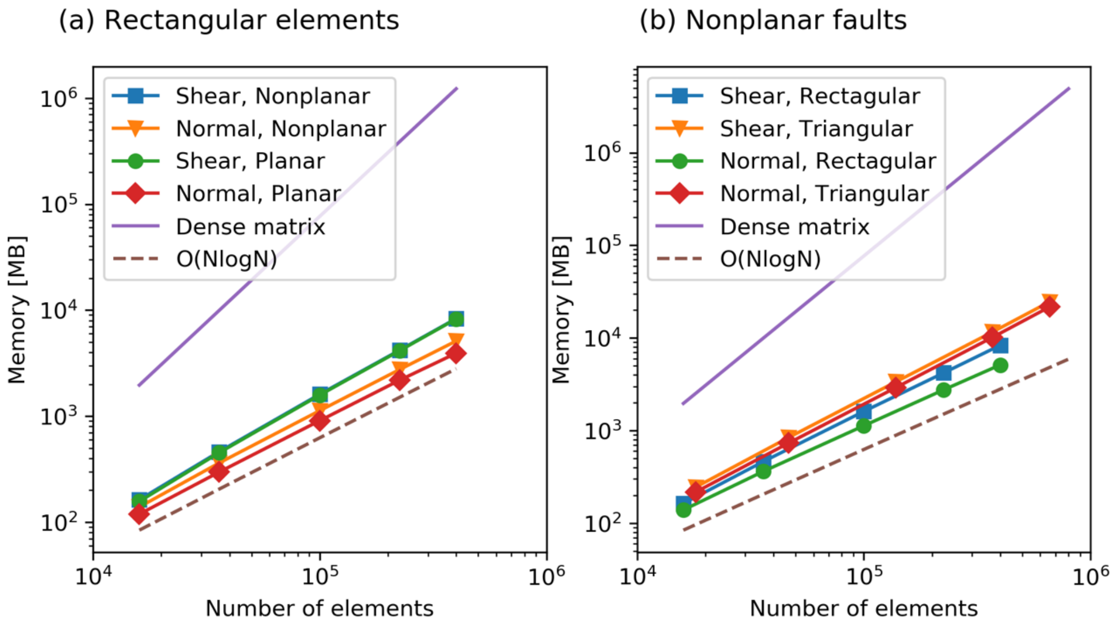

Figure 2.9. Memory sizes of the H matrix with respect to the number of elements. (a) Comparison of nonplanar and planar fault geometries using rectangular elements. (b) Comparison of rectangular and triangular elements using the nonplanar fault geometry. The memory size of the dense matrix ($O(N^2)$) and an $O(N\log N)$ slope are also shown as a reference.

Next, we measure the memory size of lattice H-matrices by varying the number of MPI processes (in concept, the memory size of the normal H-matrices does not depend on the number of MPI processes). We set $q = 4$ except for $N_p = 1$. As expected, the overall memory size of the lattice H-matrices increases with the number of MPI processes because of the smaller off-diagonal block sizes (Fig. 2.10a). However, the maximum memory among the MPI processes is the bottleneck in the computation of HMVM, which is plotted in Fig. 2.10b. For N_p<1,000, normal H-matrices are superior because the memory sizes of the diagonal MPI processes in the process grid tend to be large in lattice H-matrices. For N_p>1,000, the lattice H-matrices perform better. The saturation of the maximum memory in normal H-matrices corresponds to the submatrix that has the largest memory.

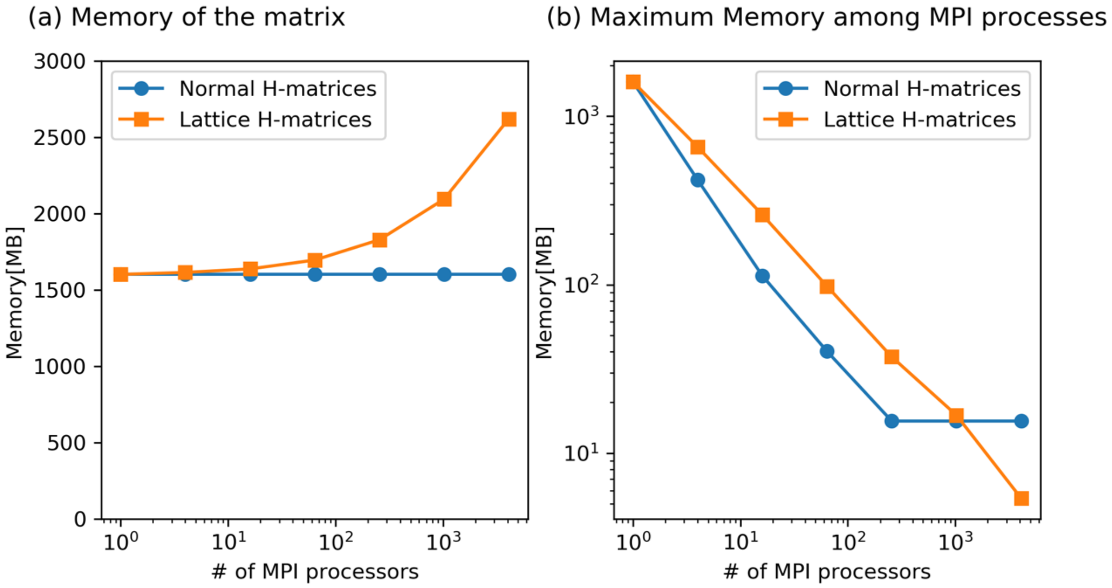

Figure 2.10. (a) Overall memory sizes of the normal and lattice H-matrices. (b) Maximum memory size among MPI processes. The case for shear stress and 100,000 rectangular elements.

2.5.2. Execution time and parallel scalability

For lattice H-matrices, we measure the dependence of the number of elements on the execution time of 100 time-steps using 100 and 900 MPI processes (Fig. 2.11). As expected, we confirm a $O(N\log N)$ or slightly steeper increase in the execution time.

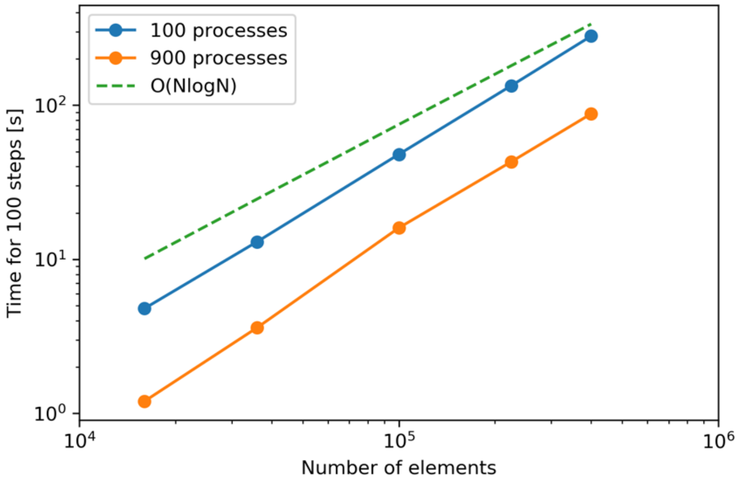

Figure 2.11. Number of elements vs. execution time of 100 time-steps with the lattice H-matrices. $O(N\log N)$ curve is also shown as a reference.

Next, we measure parallel scalability (Fig 2.12). Our simulation using lattice H-matrices shows a consistent acceleration beyond 30,000 cores in the case of $N = 400{,}000$. We also show the result of the normal H-matrices, which exhibits an almost linear acceleration up to ~20 cores but rapidly saturates ~100 cores. The speed-down over 100 cores is caused by the increase in the communication cost, which is proportional to N_p.

By comparing the two methods, the normal H-matrices are faster by up to a few hundred MPI processes. The deceleration of lattice H-matrices from normal H-matrices occurred because the maximum memory for an MPI process is larger than that of normal H-matrices, as shown in the previous section (Fig. 2.10b). The lattice H-matrices outperform normal H-matrices beyond a few 100s of cores owing to the reduction in the communication cost. We do not observe the saturation of the computation speed for lattice H-matrices, even with more than 10,000 cores. Fig. 2.13 shows how a large fraction of the computation time is used in the HMVM in lattice H-matrices. The ratio of HMVM decreases with an increase in MPI processes, but it is always above 90%. From this figure, we expect a further acceleration in performance using additional processors.

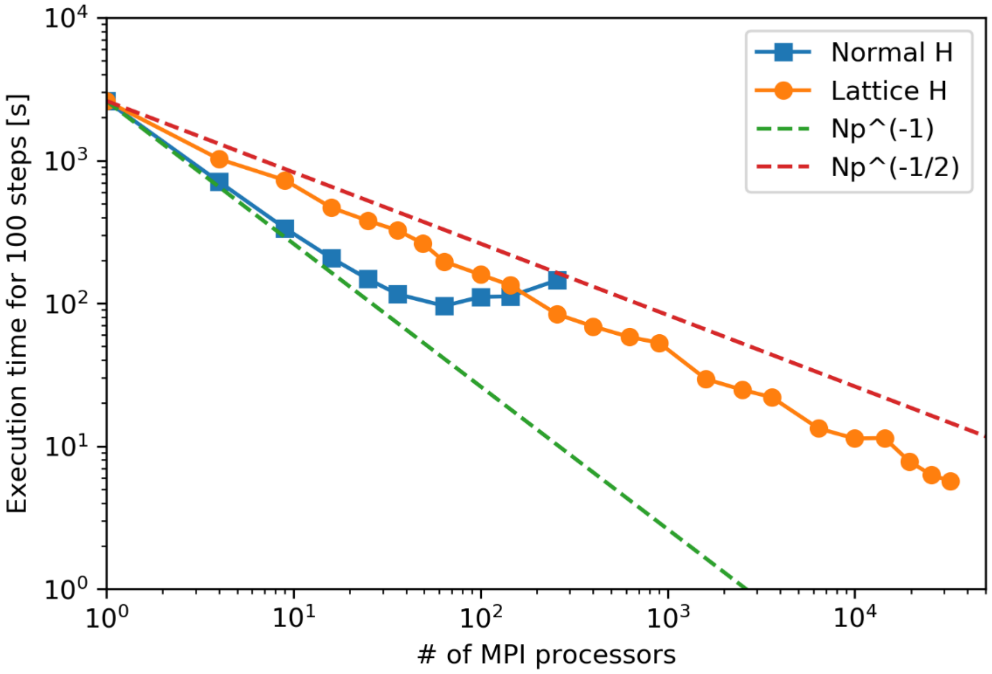

Figure 2.12. Parallel scalability when 100 time-steps are performed ($N = 400{,}000$ rectangular elements).

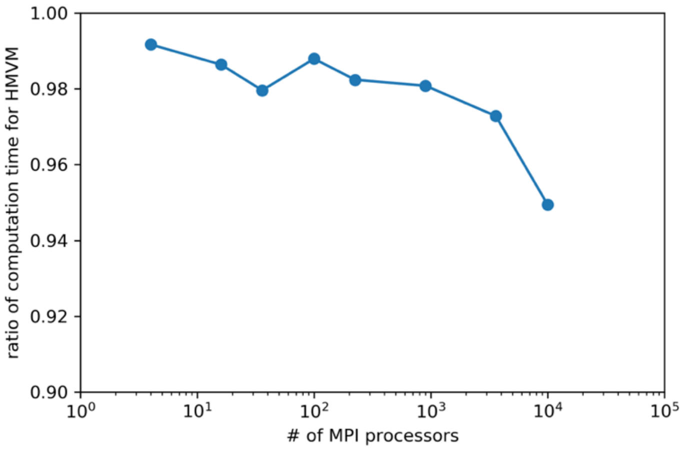

Figure 2.13. Ratio of calculation time of HMVM over the one time-step for $N = 400{,}000$.

2.6. Discussions

In this study, we developed a method for earthquake sequence simulations with BEM using normal and lattice H-matrices. This method is highly flexible with fault geometries and accounts for the normal stress evolution, which is often neglected. Numerical experiments were conducted in a 3D nonplanar thrust fault to demonstrate the accuracy of our method in terms of convergence with decreasing error tolerances in both the low-rank approximation in H-matrices and the Runge-Kutta method. Our numerical simulation using a curved thrust fault showed complex patterns in earthquake sequences, which motivates us to conduct further studies focusing on earthquake science. Our code can also be applied to natural fault systems worldwide and is potentially highly useful in physics-based earthquake hazard analyses.

In our numerical experiments, we confirmed $O(N\log N)$ complexity for the execution time for lattice H-matrices. Although Ohtani et al. (2011) also showed $O(N\log N)$ complexity, our curved fault geometry is more complex than the planar thrust fault model used by them. One question is that whether this $O(N\log N)$ complexity is maintained for further complex geometries, such as rough faults and/or fault networks (Ozawa & Ando, 2021). Additionally, inhomogeneous meshes can be used if the required resolution is not uniform due to spatial variation in friction and stress conditions. The use of inhomogenous meshes might change the compressibility of the dense matrices, even for planar faults. Further studies are necessary to answer these questions.

We evaluated the parallel scalability of our simulation code using a supercomputer Oakforest-PACS. The lattice H-matrices overcame the high communication costs between MPI processes and enabled efficient computation using many cores. The maximum computation speed for the lattice H-matrices was greater than ten times faster than that of the normal H-matrices. However, the lattice H-matrices were not as efficient as the normal H-matrices for a small number of cores. Thus, normal H-matrices should be used when a small number of CPUs is available.

Although we only performed flat-MPI simulations, we expect further acceleration using openMP and MPI hybrid parallelization. Hybrid parallelization is especially important for extremely large ($N > 1{,}000{,}000$) problems, as only few MPI processes can be used per CPU node because of memory limitations that cannot be distributed, such as the information of the coordinates.

3. Mainshock and Aftershock Sequence Simulation in Geometrically Complex Fault Zones

This chapter has been published as "Mainshock and Aftershock Sequence Simulation in Geometrically Complex Fault Zones" in Journal of Geophysical Research; Solid Earth (Ozawa & Ando, 2021).

3.1. Introduction

The complexity of natural fault zones has been a target of numerous studies (Ben-Zion & Sammis, 2003; Faulkner et al., 2010). Although often simplified as a single flat surface in modeling, natural faults have complicated geometry. Faults are typically composed of a few discontinuous segments at a wide range of scales (Manighetti et al., 2015; Otsuki & Dilov, 2005; Segall & Pollard, 1980). Each continuous slip surface has deviation from planarity over broad spatial scales. The fractal-like geometrical irregularity of fault surfaces is referred to as fault roughness and is documented from various observations (Bistacchi et al., 2011; Candela et al., 2012; Power & Tullis, 1991). Furthermore, the complexity of fault zones evolves over time. In general, fault geometry becomes smoother and simpler with growth (Brodsky et al., 2011; Perrin, Manighetti, Ampuero, et al., 2016; Sagy et al., 2007; Wesnousky, 1988).

In this work, we aim to link the complex geometry of fault zones and aftershocks of earthquakes. Aftershocks are valuable tools to probe mainshock rupture. In highly accurate earthquake catalogs, the locations of aftershocks delineate the fault traces and planes (Ross, Idini, et al., 2019). They are interpreted as on-fault aftershocks, leading to the estimation of the fault plane(s) of mainshock from well-constrained aftershock distributions (Fukuyama et al., 2003). The fault model constructed using aftershock data is then used for a variety of studies, including slip inversions and dynamic rupture simulations (Hisakawa et al., 2020; Shen et al., 2009).

Recent dense seismic observations and accurate focal mechanisms prompt us to consider where aftershocks actually occur. Yukutake & Iio (2017) determined the hypocenters and focal mechanisms of the aftershocks of the 2000 western Tottori earthquake, Japan, and concluded that most aftershocks are off-fault events rather than the rerupture of the mainshock fault (Fig. 3.1). Some of aftershocks are distributed in the conjugate orientation of the main fault. The observation of the 2019 Ridgecrest earthquake has highlighted the ubiquitous nature of such an aftershock distribution (Ross, Idini, et al., 2019).

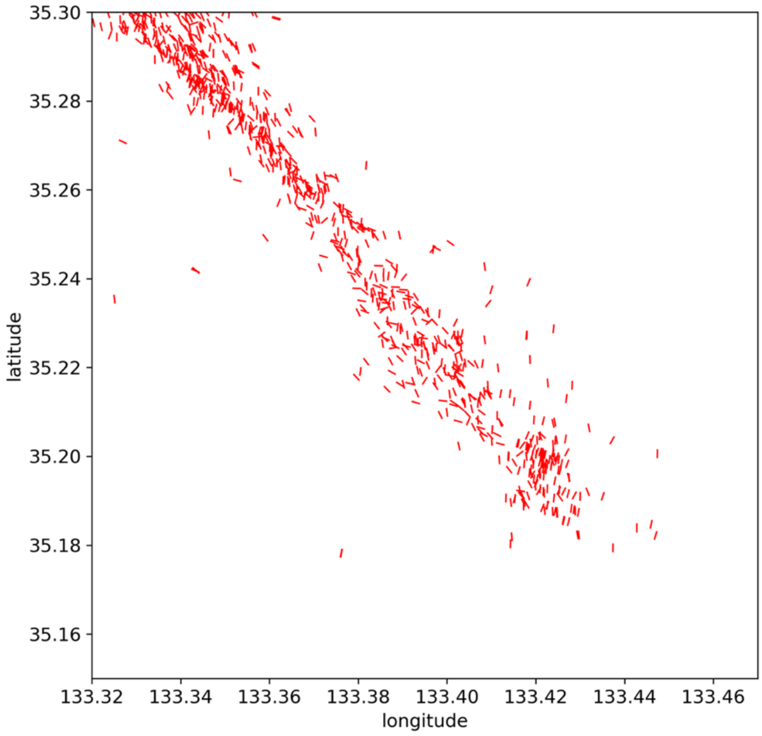

Figure 3.1. Example of the spatial distribution of aftershocks and their P-axis orientations, indicted by ticks in the case of the 2000 Tottori earthquake (Yukutake & Iio, 2017). The southern part of the rupture area, including its tip, is shown. Based on the width of aftershocks zone and large variability of focal mechanisms, they suggested that most aftershocks are off-fault events.

From the physical perspective, rerupture of part of the mainshock fault as an aftershock requires very high-speed healing and reloading. Although some recent numerical studies show that rerupture of the main fault is possible in a subset of the parameter space (Barbot, 2019b; Cattania, 2019; Yabe & Ide, 2018), many earthquake sequence models on a flat fault with spatially variable friction often show seismic quiescence after the largest events occur (Aochi & Ide, 2009; Dublanchet et al., 2013). Therefore, it is reasonable to assume that most aftershocks are the ruptures of subsidiary faults surrounding major faults that are ruptured as mainshock, at least for intraplate earthquakes on immature faults (i.e., faults with short slip histories), which have been shown to have a more complex architecture than long-lived, mature faults (Ben-Zion & Sammis, 2003; Manighetti et al., 2007), such as the Tottori event. As geological evidence, major faults are surrounded by many subsidiary faults and microcracks, and the density of subsidiary faults/microcracks decays away from the core of a fault (Savage & Brodsky, 2011; Shipton & Cowie, 2001). This structure is referred to as a damage zone (Kim et al., 2004; Perrin, Manighetti, & Gaudemer, 2016). The subsidiary faults in the damage zones would be ruptured, causing aftershocks.

The occurrence of off-fault aftershocks poses another enigmatic issue. The side of the mainshock fault is usually in the stress shadow for both conjugate faults, and so the occurrence of aftershocks on the side of the fault might be paradoxical. A solution to this issue has been given by Smith & Dieterich (2010). As mentioned, natural faults universally show deviation from a flat surface at a wide range of scales (Brown & Scholz, 1985b; Candela et al., 2012; Perrin, Manighetti, Ampuero, et al., 2016; Sagy et al., 2007). Uniform slip on a rough fault leads to heterogeneous stress distribution in its proximity (Dieterich & Smith, 2009; Sagy & Lyakhovsky, 2019). In some parts corresponding to traditional stress-shadow zones, the stress state actually becomes closer to failure. As evidence, Aslam & Daub (2018, 2019) explored the off-fault stress distribution by dynamic rupture simulations on a rough fault and many positive ΔCFF areas are present at the side of the fault trace.

The purpose of this study is to convert the work by Smith & Dieterich (2010) into numerical simulations of fault slip. We use large-scale 2D earthquake sequence simulations to reproduce realistic aftershock seismicity. The strength of an earthquake sequence simulation is its internal consistency. The times, locations, and sizes of events are determined by the system itself (Erickson et al., 2020; Rice, 1993; Tse & Rice, 1986). Furthermore, it is based on a continuum representation of faults rather than representation by inherently discrete elements (Ben-Zion & Rice, 1993; Richards-Dinger & Dieterich, 2012; Shaw et al., 2015; Ziv & Rubin, 2003) or models based on the rate-state seismicity equation (Dieterich, 1994; Hainzl et al., 2010; Helmstetter & Shaw, 2006; Smith & Dieterich, 2010), which are even more simplified. Thus, our model can remove many simplifying assumptions made in previous models. Taking advantage of this method, we demonstrate that realistic mainshock and aftershock sequences, both in space and time, are consistently explained by the effect of a geometrically complex fault zone composed of a rough main fault and numerous subsidiary faults.

3.2. Model

3.2.1. Fault geometry

The problem is in the 2D plane strain condition. The main fault is assumed to be 100 km in length and its geometry $y = h(x)$ is self-similar, which is generated using a Fourier transformation method (Dunham et al., 2011b). The RMS amplitude of roughness L_y for a fault length L_x is expressed as

$$L_y = \alpha \, L_x \; (L_x > \lambda_{min}), \tag{3.1}$$

where α is the aspect ratio of roughness and λ_{min} is the minimum roughness scale. We use $\alpha = 0.01$ and $\lambda_{min} = 0.5$ km for the reference simulations. This value of α is consistent with observation by Candela et al. (2012), while the choice of non-zero λ_{min} is to avoid stress divergence originated from the curvature effect in an elastic model (Romanet et al., 2020).

The main fault is surrounded by 600 subsidiary faults, which are potential aftershock locations. The subsidiary faults are 0.6 km in length and planar. These choices are ad-hoc and are not motivated by observational evidence, so we do not focus on the absolute number of aftershocks and their magnitudes. We also attempt to use power-law size distributions of subsidiary fault distributions in section 3.3.6 because it has been suggested to characterize natural fault length distributions (Bonnet et al., 2001).

The locations of the subsidiary faults are random in a 15 km × 140 km rectangle (Fig. 3.2a). This size is chosen by trial and error so that more than 90% of potential aftershocks are covered. The density of secondary faults decays away from the fault (Shipton & Cowie, 2001) and could be heterogeneous along strike (Perrin, Manighetti, Ampuero, et al., 2016), but we ignore the heterogeneity to focus on the effect of the stress perturbation by the mainshock on the aftershock distribution. For computational reasons, we do not allow two different faults to overlap.

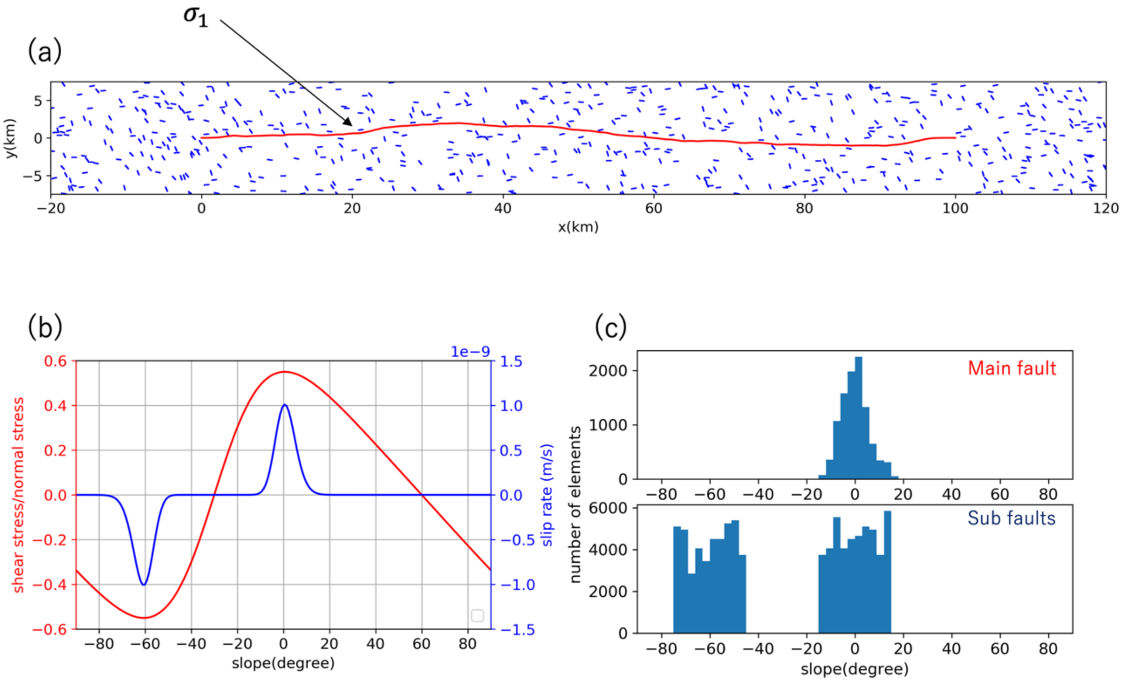

Figure 3.2. Problem setting. (a) Fault geometry. The main fault is shown in red and subsidiary faults are shown in blue. (b) Initial friction coefficient and slip rate as a function of the local orientation of the subsidiary faults. (c) The histogram of local orientation of the fault for main and subsidiary faults, measured from the x-axis.

The orientation of the subsidiary faults is confined in the ranges -75° to -45° and -15° to 15° relative to the x-axis, because, in the preliminary simulations, we found that few subsidiary faults whose orientations are outside these ranges produced aftershocks (see also Section 3.3.5). This restriction can also be justified given that the distribution of fault orientation should reflect the regional stress field, although some geological studies show that most secondary faults and cracks off a major fault are oblique by 0° to 30° to its trace, which is considered to be related to the growth process of the fault (Perrin, Manighetti, & Gaudemer, 2016). This restriction will be relaxed in Section 3.3.5 to explore the variability in focal mechanisms for strong and weak faults. To examine statistical properties, we generate 30 different realizations of subsidiary faults (Fig. 3.2a) for the same main fault geometry.

3.2.2. Fault Constitutive Law

The faults are governed by the rate and state friction law (Dieterich, 1979; Ruina, 1983). Specifically, we use the regularized version around $V = 0$ (Rice et al., 2001), in which the ratio of shear stress τ and normal stress σ is given by

$$\frac{\tau}{\sigma} = a\sinh^{-1}\left(\frac{V}{2V_0}e^{\frac{\phi}{a}}\right). \tag{3.2}$$

This formulation allows for freedom of the slip direction (positive indicates right-lateral and negative indicates left-lateral slip). It is notable that Barbot (2019a) proposed another physics-based formulation of rate and state friction that is regularized at $V = 0$. The state evolution is governed by the aging law

$$\frac{d\phi}{dt} = \frac{b}{d_c}\left[V_0 \exp\left(\frac{f_0 - \phi}{b}\right) - |V|\right]. \tag{3.3}$$

The parameter values are set as given in Table 3.1. Our faults are velocity-weakening everywhere ($a - b$ is negative). The value d_c is taken to be different for the main and subsidiary faults, which is to enable seismic slip on the subsidiary faults. A fault can slip seismically when the fault length L is larger than the nucleation length $L_c =$

$\pi^{-1}\left(\frac{b-a}{b}\right)^2\frac{Gd_c}{b\sigma}$. (Rubin & Ampuero, 2005), so we set $L > L_c$.

To ensure numerical convergence, the mesh size needs to be smaller than the cohesive zone size $L_b = \frac{GD_c}{b\sigma}$. Although L_b depends on the locations due to the normal stress variation, we use $L_b = 30\Delta x$ for the main fault, and $L_b = 3.75\Delta x$ for the subsidiary faults in the case of $\sigma = 100$ MPa. We also perform the convergence test in Appendix C. In addition, μ_0 in the main fault is set to be slightly smaller than that of subsidiary faults to prevent the mainshock rupture from being arrested due to the geometric complexity before reaching the tip of the fault (Table 3.1). This could be supported given that a main fault is frictionally weaker than subsidiary faults, which is expected to be more immature (Fang & Dunham, 2013), but examining the effect of this difference is beyond the scope of this study.

3.2.3. Initial Condition

We assume a spatially uniform stress field. Thus, the shear and normal stresses on the fault are unique functions of the local orientation of the fault as

$$\tau_0 = \sigma_{xy}\cos 2\theta + \frac{1}{2}\left(\sigma_{xx} - \sigma_{yy}\right)\sin 2\theta, \tag{3.4}$$

$$\sigma_0 = \frac{\sigma_{xx}+\sigma_{yy}}{2} - \frac{\sigma_{xx}-\sigma_{yy}}{2}\cos 2\theta + \sigma_{xy}\sin 2\theta, \tag{3.5}$$

where θ is the angle of the fault relative to the x-axis and σ_{ij} is the background stress. Thus, initial friction coefficient τ/σ is a function of θ. Initial slip rate V and state variable ϕ can be chosen arbitrarily with a constraint of the friction coefficient. We fix the initial state variable to a constant value ($\phi_{ini} = 0.55$), and the initial slip rate V is determined by equation (3.2). Fig. 3.2b shows the initial condition of the subsidiary faults as a function of orientation, and Fig. 3.2c shows the histogram of fault orientation for main and subsidiary faults for the realization shown in Fig. 3.2a.

Although our model can run multiple earthquake cycles with an adequate external loading process, we focus on a single mainshock and aftershock sequences rather than multiple earthquake cycles of the main fault in this work. This is mainly because the heterogeneity in stresses constantly grows with accumulating slip, and running many cycles is difficult in a purely-elastic model. Hence, we set no external loading and stop a run of our simulation after the last slip event completes.

3.2.4. Numerical Method

Our numerical method is a quasi-dynamic earthquake sequence simulator using the boundary integral equation method (BIEM). BIEM is one of the best options for handling complex fault geometry. The change of normal and shear stresses on the center of each element are computed by the following equations:

$$\tau_i^e = \sum_j S_{ij} \Delta u_j - \frac{GV_i}{2V_s}, \tag{3.6}$$

$$\sigma_i^e = \sum_j N_{ij} \Delta u_j, \tag{3.7}$$

where Δu is slip and S_{ij} and N_{ij} represent the stress interaction kernel (see the full expression in Appendix A) assuming an infinite and homogeneous elastic medium. The $GV/(2V_s)$ term is radiation damping (Rice, 1993), an approximation of inertia effects.

In computing matrix-vector products in the above equations, which is the most time-consuming part, we use the method called hierarchical matrices (H-matrices) to reduce computational costs as done in many boundary integral models (e.g. Ohtani et al. 2011). HACApK libraries are used for implementation. Equations (3.6) and (3.7) are coupled with the boundary conditions described by equations (3.2) and (3.3) to make a closed system. This results in a $3N$ set of ordinary integral equations, where N represents the number of elements ($N = 100{,}000$ in this study). In a time-marching scheme, we solve these equations using a Runge-Kutta scheme with adaptive-time stepping (Press et al., 2007). As a result, the step size Δt becomes roughly proportional to the inverse of the maximum slip rate.

With linear elasticity and rough fault geometry, the root-mean-square of normal stress fluctuation in space is proportional to slip (Dunham et al., 2011b). Thus, fault opening would occur with increasing slip where normal stress becomes negative. In reality, however, off-fault plasticity would relax the stress heterogeneity (Dieterich & Smith, 2009), and normal stress does not become negative. This is confirmed from dynamic rupture simulation on a rough fault with Drucker-Prager viscoplasticity (Dunham et al., 2011b). Hence, we set the minimum and maximum values of normal stress to 30 MPa and 170 MPa as an approximation of plastic yielding.

Table 3.1. Notation and parameter values in the representative simulation

Parameter	Description	Value
G	Shear modulus	40 GPa
ν	Poisson's ratio	0.25
V_s	Shear wave speed	3.464 km/s
L_m	Length of main fault	100 km
L_s	Length of subsidiary faults	0.6 km
N_s	Number of subsidiary faults	600
α	Roughness amplitude of main fault	0.01
λ_{min}	Minimum roughness of main fault	0.5 km
σ_{yy}	Background stress	100 MPa
σ_{xy}	Background stress	55 MPa
Ψ	Maximum compressive angle of background stress	30º
ϕ_{ini}	Initial state variable	0.55
a	Rate state parameter	0.016
b	Rate state parameter	0.02
D_c^m	Characteristic slip distance for the main fault	0.02 m
D_c^s	Characteristic slip distance for the subfaults	0.001 m
V_0	Reference slip rate	1 nm/s

μ_0^m	Reference friction coefficient for the main fault	0.55
μ_0^s	Reference friction coefficient for the subfaults	0.60

3.3. Results

3.3.1. Overview

In our simulations, the mainshock ruptures the entire main fault trace for the reference parameters (Table 3.1). If the initial stress is smaller than this, the rupture stops before arriving at the tips of the main fault. For simplicity, we limit our attention to the full-rupture case in this work. Fig. 3.3a shows the evolution of the maximum slip rate on the fault, which shows many spikes (i.e., aftershocks) with a power-law-like decaying trend after the mainshock. This reflects the logarithmic increase of the state variable ϕ with time. While the power-law decay is similar to afterslip in a velocity-strengthening fault (Marone et al., 1991), we note that the amount of net slip during the postseismic period is negligible compared to that of the coseismic slip (Fig. 3.3b).

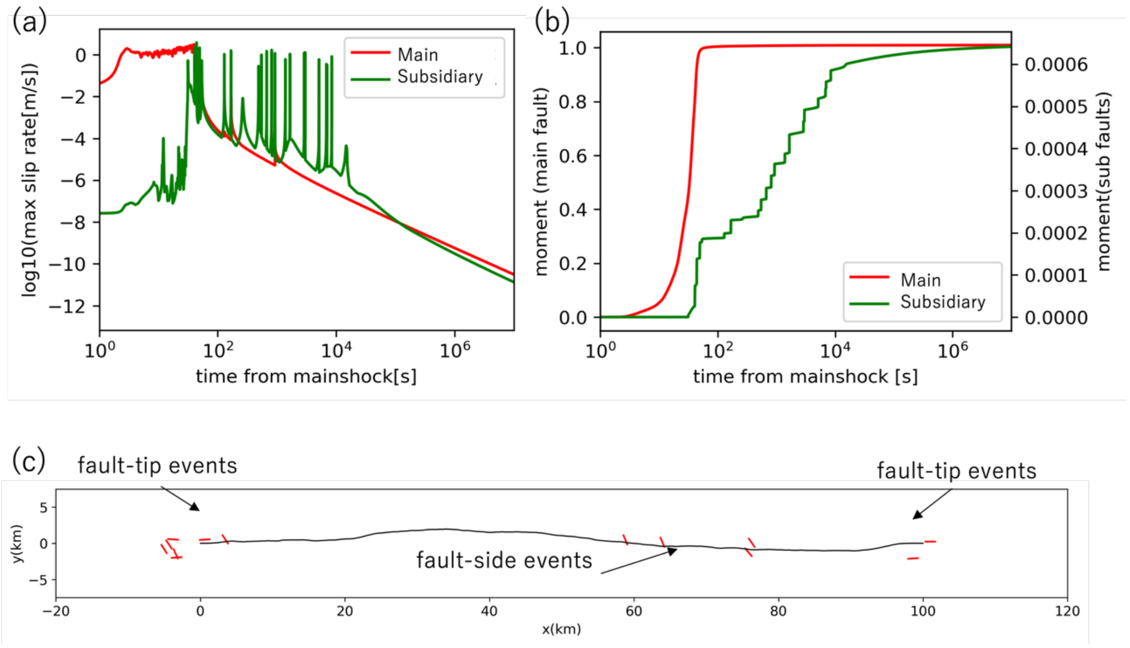

Figure 3.3. (a) The maximum slip rates on the main and subsidiary fault plotted against the time from the onset of mainshock in one representative sample. (b) Cumulative moment release on the main and subsidiary faults. The moment is computed by the sum of slip × element size for all elements. We

normalize the seismic moment by the mainshock moment. (c) Spatial distribution of aftershocks for one simulation. The black line indicates the main fault trace. The orientation of red lines indicates the orientation of subsidiary faults that produce aftershocks.

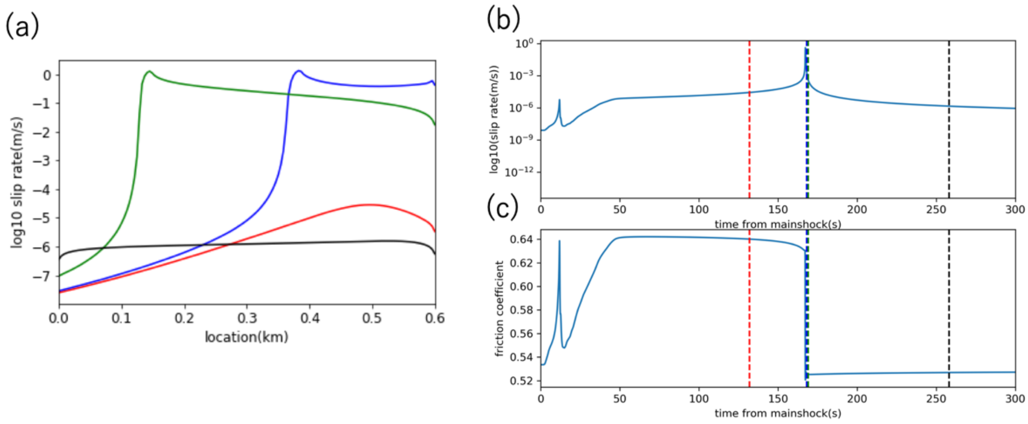

Figure 3.4. One example of aftershocks. The fault is located at (x, y) = (59, 0 km). (a) Snapshots of spatial distribution of slip rate. The red curve is the nucleation phase. The blue and green is the coseismic phase. The black curve is the postseismic phase. (b) Evolution of slip rate. (c) Evolution of friction coefficient. The colors of the dashed lines in (b) and (c) corresponds the snapshots in (a).

We define an aftershock as a slip event on each subsidiary fault that has a maximum slip rate larger than 1cm/s. Fig. 3.4a shows snapshots of slip rate in a subsidiary fault located at $x = 59$ km that produces aftershocks roughly 200 seconds after the mainshock. This event nucleates at the closest end of this subsidiary fault. The evolution of the slip rate and friction coefficient at the nucleation point of this fault is plotted in Fig. 3.4b and 3.4c, respectively. During the mainshock, the slip rate changes due to the direct effect of the rate and state friction in response to the coseismic stress change. The first sharp peak is the effect of the passage of the rupture front. The second gradual rise is the static stress change by slip, which makes the fault enter its nucleation phase. In a finite time, the fault transitions to dynamic rupture and releases the stress. After the rupture, the slip rate shows power-law decay, and the stress becomes constant.

As shown in Fig. 3.3c, the aftershocks are clustered in the vicinity of the main fault, as observed in nature. They can be classified into two types based on their locations: fault-tip aftershocks and fault-side aftershocks (Fig. 3.3c). Fault-tip aftershocks are triggered by stress concentration due to the termination of rupture, while fault-side aftershocks are triggered by the heterogeneous stress perturbation due to rough main fault slip. Hereafter, aftershocks located in 5 km$< x <$95 km are classified as fault-side events and others are classified as fault-tip events in the ensemble analyses given from section 3.3.2. This value is chosen by the region of the aftershock occurrence in the case of a flat fault (i.e., no aftershock occurs in 5 km$< x <$95 km). The number of subsidiary faults that produce an aftershock is roughly 10 out of 600 subsidiary faults for a single run of our simulation (Fig. 3.3c), which means that most of the subsidiary faults are not activated. Notably, we observe no reruptures of the main fault because the stress of the main fault has already been released by the mainshock.

Fig. 3.3c also shows the orientations of the faults that host aftershocks. Their orientation is shown to have a variety and is not limited to a plane parallel to the main fault, corresponding to the observation in the Tottori earthquake (Fig.3.1) and many others. The mixture of two conjugate fault planes in a single earthquake sequence is often observed (Fukuyama, 2015). We perform statistical analysis of the focal mechanism of aftershocks in section 3.3.5.

A fraction of slip events on the subsidiary faults occurs before the rupture termination of the mainshock (~ 50 sec). They are not counted as aftershock in our analysis. They could be viewed as a type of off-fault damage, which is explicitly modeled as discrete fractures or branching faults in dynamic rupture simulations (Ando & Yamashita, 2007; Okubo et al., 2019). However, it should be noted that off-fault damage includes many extensional cracks in nature, which are not captured in our model.

Hereafter, we combine the results with 30 ensembles of locations of subsidiary faults to study the statistical characteristics of aftershocks because the number of aftershocks resulting in a single simulation is not sufficiently large. We checked that the difference in the distribution of subsidiary faults has little impact on the mainshock process itself, for example, slip distribution.

3.3.2. Spatial distribution of aftershocks

An important result of our simulations is the occurrence of fault-side aftershocks. Most fault-side aftershocks are confined within 1 km from the main fault trace (Fig. 3.5b). This value is similar to the observationally obtained value by Dieterich & Smith (2009) and Yukutake & Iio (2017) shows that the stress fluctuation decreases as a power of the fault-perpendicular distance, in which the exponent depends on the Hurst exponent that characterizes the fractality of the fault geometry. Hence, the width of the aftershock zone is determined by the superposition of the amplitude of small-scale stress heterogeneity and the large-scale stress drop.

The number of fault-side aftershocks is not uniform along strike. We find that the frequency has a strong correlation with the local orientation of the main fault (Fig. 3.5a). Specifically, aftershocks are clustered where the slope of the main fault $dh(x)/dx$ is local minimum, which corresponds to releasing bends or transtensional structures (Cunningham & Mann, 2007).

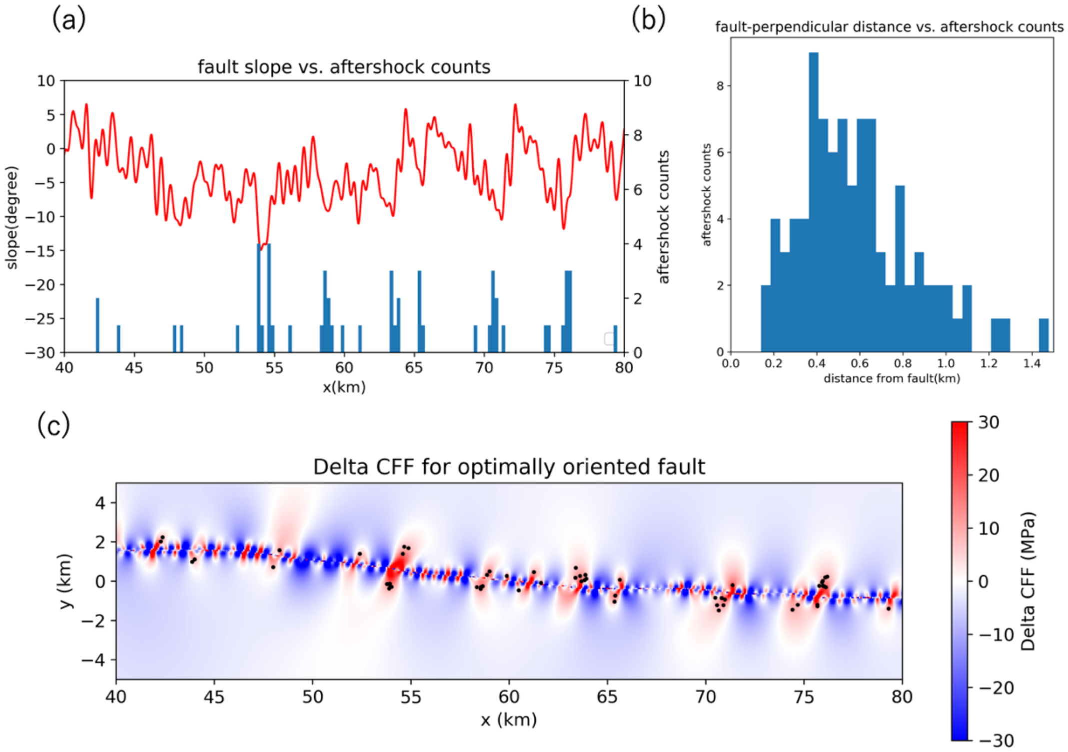

Figure 3.5. (a) The slope $dh(x)/dx$ of the main fault and the number of the location of aftershocks in an ensemble of 30 simulations. (b)Perpendicular distance of aftershock hypocenters from the main fault. (c) Computed ΔCFF for the optimally oriented planes from the slip distribution of the mainshock. Black dots indicate the location of aftershocks.

We compute the Coulomb failure function (ΔCFF) as

$$\Delta\mathrm{CFF} = \Delta\tau - \mu\Delta\sigma, \tag{3.8}$$

from the final slip of the mainshock in Fig. 3.5c assuming $\mu = 0.6$ and optimally oriented planes using the prestress and stress change due to the mainshock (King et al., 1994).

As can be seen from Fig. 3.5c, positive ΔCFF is concentrated at releasing bends (local minimum of slope) where most aftershocks occur. This correlation implies that fault roughness can be an origin of the along-strike heterogeneity of aftershock productivity. As previously noted, the postseismic slip on the main fault is negligible (Fig. 3.3b), and ΔCFF is almost the same after the rupture is complete. Conversely, the stress transfer due to aftershocks could alter local stress states. This results in secondary triggering and is responsible for the deviation between aftershock locations and Δ CFF from the mainshock. In the current simulation, the number of aftershocks in the negative ΔCFF area due to the mainshock is small, which implies that the contribution of secondary triggering is limited.

The roughness of the main fault is critically important for the spatial distribution of aftershocks. To illustrate its effect, we plot the distribution of aftershocks for different aspect ratios α in equation (3.1) in Fig. 3.6. The number of fault-side aftershocks increases with fault roughness because of the increase in positive ΔCFF area (Aslam & Daub, 2018; Smith & Dieterich, 2010), where the positive stress perturbation due to roughness overcomes the overall decreasing trend in the stress shadow.

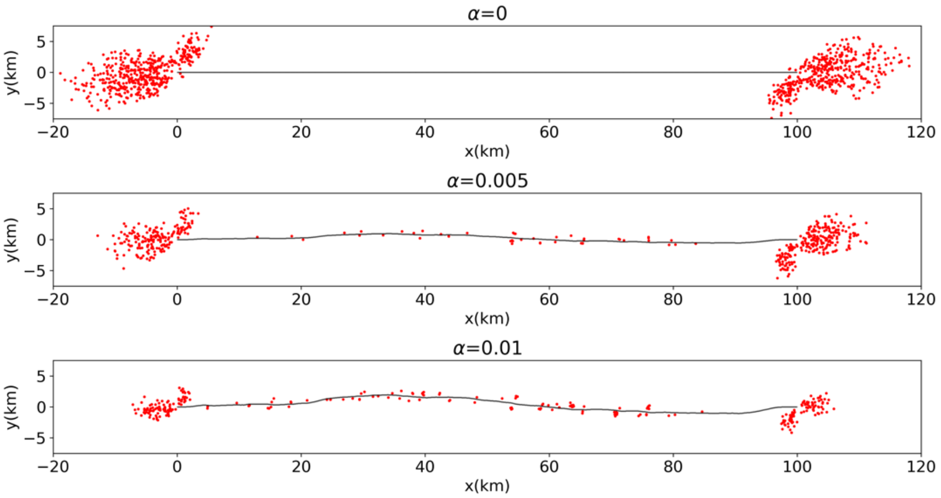

Figure 3.6. Aftershock locations for different main fault roughness (α = 0, 0.005, 0.01). The black line indicates the main fault trace. Fault-tip aftershocks decrease, and fault-side aftershocks increase with increasing fault roughness.

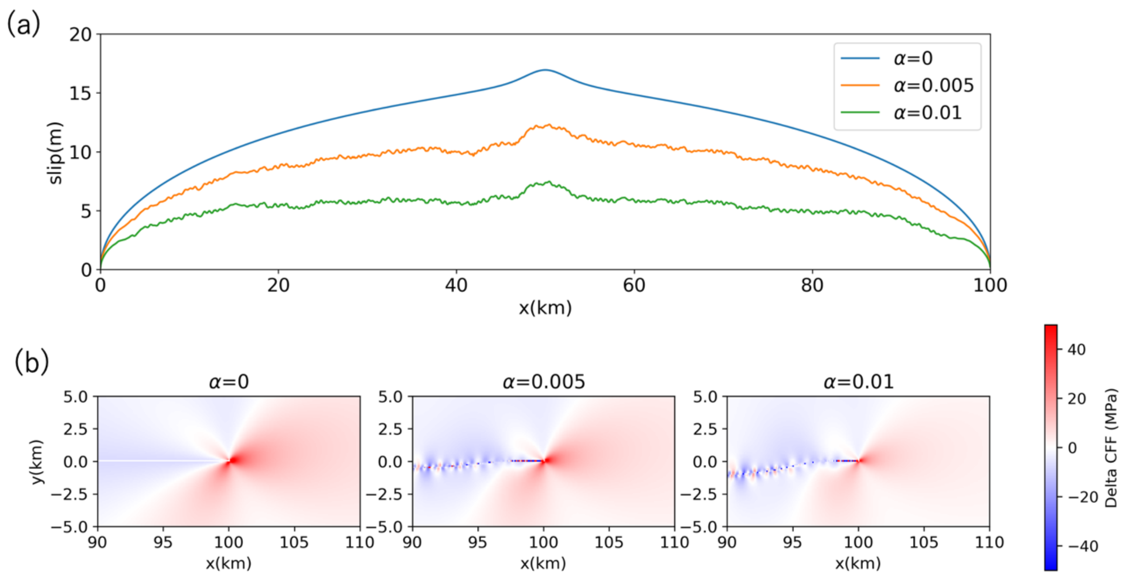

Figure 3.7. (a) Slip distribution of the mainshock for different main fault roughness. (b) ΔCFF for a plane parallel to the x-axis for different main fault roughness.

In contrast, the number of fault-tip aftershocks decreases with increasing fault roughness. This is related to the slip distribution of the main fault (Fig. 3.7a). The fault roughness reduces the slip of the mainshock, and the stress concentration around the tips of the fault becomes smaller (Fig. 3.7b). Smaller stress concentration results in lower aftershock productivity.The reduction of slip on rougher faults can be understood by backstress or roughness drag (Dieterich & Smith, 2009; Fang & Dunham, 2013; Ozawa et al., 2019). Slip on a rough fault produces an additional shear resistance, which is expressed as

$$\tau_{drag} = (2\pi)^3 \alpha^2 G \frac{\delta}{\lambda_{min}}, \tag{3.9}$$

where δ is slip. Roughness drag enhances pulse-like ruptures and deviation from the classical elliptic crack (Dieterich & Smith, 2009; Heimisson, 2020), which reduces the stress concentration at the fault tips.

The pulse-like ruptures only occur and the effect of roughness drag is only important if the rupture length is larger than $\lambda_{min}/(4\,\pi^4\,\alpha^2)$ (Heimisson, 2020). Otherwise, the classical elliptic crack is realized and the stress concentration around the tips is strong. Hence, at least for the same fault, we can expect that the aftershocks of smaller mainshocks are more localized around the fault tips.

3.3.3. Temporal evolution

We now consider the temporal behavior of the aftershocks and exploring the effect of the initial condition. Fig. 3.8 plots the seismicity rate against time, which follows the Omori-Utsu law (Omori, 1894; Utsu et al., 1995),

$$\lambda(t) = \frac{K}{(t+c)^p}. \tag{3.10}$$

with the p-value being approximately 0.9. This is similar to the circular crack case of the Dieterich's model, which derives the Omori-Utsu law as a sequence of nucleation of rate-state faults subjected to a stress step due to a mainshock. In deriving the Omori-Utsu law, the Dieterich model assumes a constant background seismicity rate before the mainshock, which makes that the population of faults follow a particular inverse-exponential-like initial slip-rate distribution (equation (B5) in Dieterich, 1994). Our model is based on uniform background stress and non-uniform stress change by the mainshock, and therefore these assumptions should not be held. Nevertheless, our result clearly shows the Omori-Utsu law. This implies that the Dieterich model still works, considering the modification of the stressing conditions before and after the mainshock with realistic stress perturbations and subsidiary fault distributions surrounding the main fault.

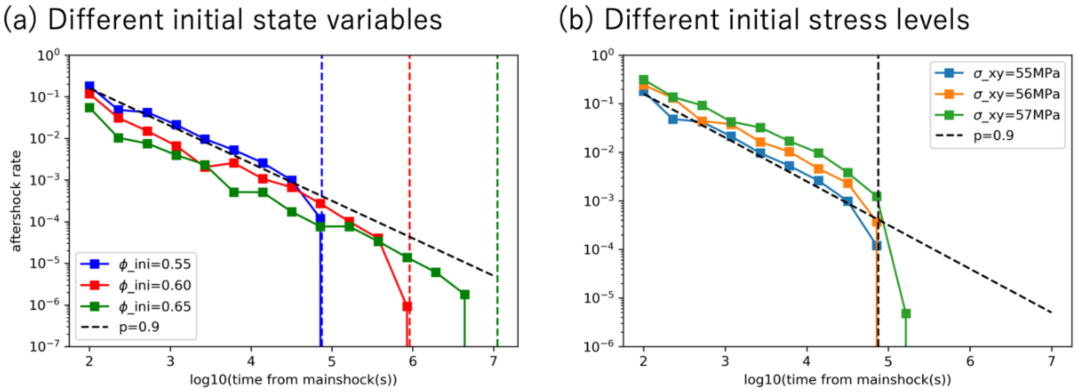

Figure 3.8. Number of aftershocks per second against time from the onset of mainshock with reference slope $p = 0.9$. (a) Dependence on the initial state variable. (b) Dependence on the background stress. Vertically dashed lines are estimated by equation (3.11).

In contrast, the observed numbers of the aftershocks are significantly smaller than the prediction by the Omori-Utsu law after characteristic times. By changing the initial state variable, we find that the duration increases upon increasing the initial state variable (Fig. 3.8a). Heimisson & Segall (2018) found that the Dieterich model (and the Omori-Utsu law) hold only when the sources are "well-above steady state" after the mainshock, and aftershocks do not occur below the steady-state. With this in mind, as shown in Appendix C, we can estimate the duration of power-law decay by

$$t_{omori} = \frac{a}{HV_0} \exp\left(-\frac{\mu_0 - \phi_{ini}}{b}\right), \tag{3.11}$$

where H is a constant depending on friction parameters and stiffness, and ϕ_{ini} is the initial state variable. Equation (3.11) indicates that the aftershock duration primarily depends on the initial state variable of the subsidiary faults. The estimated t_{omori} for the parameters and initial state by equation (3.11) are in good agreement with our simulations (Fig. 3.8a).

The early cut-off time c cannot be seen (Fig. 3.8). There is a debate regarding whether the cut-off time is intrinsic instead of the detection limit due to mainshock coda wave (Utsu et al., 1995) (significantly larger than the rupture duration of the mainshock). Enescu et al. (2009) showed that the power-law time dependence holds from approximately one minute from the mainshock using highpass-filtered seismograms. Similar to their observation, our results suggest that power-law decay of aftershock rate begins immediately after the termination of the mainshock rupture.

We also run simulations of different initial stress levels (background σ_{xy}) and check the robustness of the Omori-Utsu law, also finding that the number of aftershocks increases with the initial stress for two reasons (Fig. 3.8b). First, the high initial stresses on the subsidiary faults require smaller stress increases to trigger aftershocks. Secondly, higher initial stresses lead to higher stress drops and mainshock slips. Therefore, it induces larger stress perturbation to the surrounding medium. Observations also suggest that the aftershock productivity has a positive correlation with the stress drop with fixed rupture area (Wetzler et al., 2016). Although higher initial stress leads to more aftershocks, the duration of power-law decay is unchanged (Fig. 3.8b). The p-value shows a slight decrease with increasing initial stress.

3.3.4. Expansion of aftershock area

It has long been documented that aftershock zones expand with time (Kato et al., 2016; Lengliné et al., 2012; Peng & Zhao, 2009; Tajima & Kanamori, 1985). Our simulation also shows a clear expansion of the area of fault-tip aftershocks (Fig. 3.9). While early aftershocks are limited near the main fault, later aftershocks occur approximately 6 km away from the main fault. Our result implies that very early aftershocks are a good indicator of the rupture extent of the mainshock.

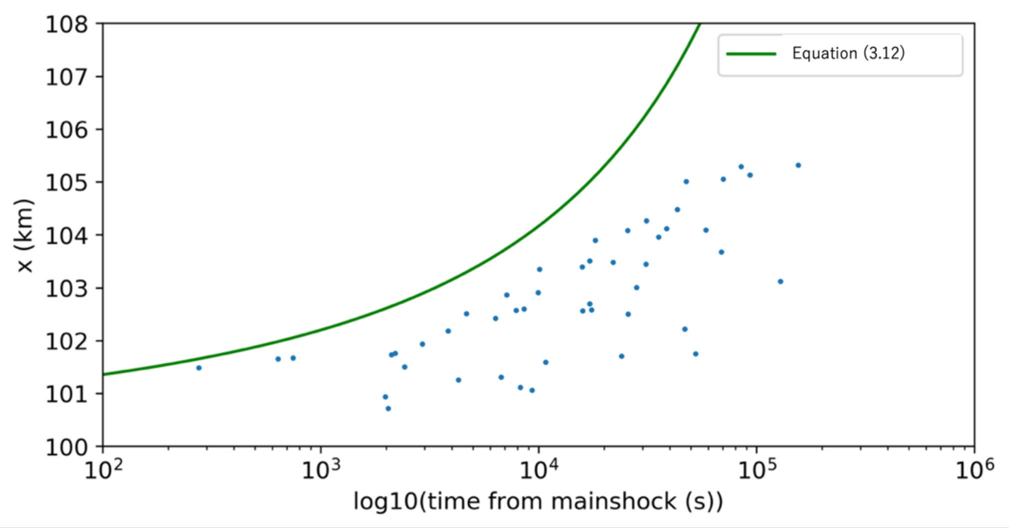

Figure 3.9. Migration process of aftershock area around the tip of the fault (the rupture termination is at 100 km). Thirty ensembles are plotted together. The curve is equation (3.9) or (D.13) with $V_{ini} = 2 \times 10^{-10}$ m/s, K = 4 MPa$\sqrt{50\pi km}$, σ = 100 MPa, and other parameters are given by Table 3.1.

The expansion can be interpreted as the non-uniformity of nucleation time of triggered events, which originates from the decay of stress change with distance from the mainshock fault in the Dieterich model. For planar mainshock fault, using fracture mechanics and rate and state friction, we can approximately derive the aftershock front x_{tip} as

$$x_{tip} = (A - B\log t)^{-2}, \tag{3.12}$$

where A and B are constants (see Appendix C for the detail). Using the values, the numerical result can be fit with that calculated using equation (3.12) for the early time. However, the expansion speed is slower than equation (3.12) for the later aftershocks due to the breaking of approximation made in deriving equation (3.12). Notably, our numerical result shows a nearly log-time expansion pattern between 10^3 s and 10^5 s in both cases. Logarithmic expansion is preferred by many observations, including the 2004 Parkfield earthquake (Peng & Zhao, 2009), the 2011 Tohoku earthquake (Lengliné et al., 2012), and the 2016 Kumamoto earthquake (Kato et al., 2016). Aftershock migration is often interpreted as afterslip (Kato, 2007; Koper et al., 2018; Perfettini et al., 2018), but our result suggests that afterslip is not necessary to explain it. However, it should be noted that interaction between aftershocks is also important in aftershock expansion in some models (Heimisson, 2019; Helmstetter & Sornette, 2002).

3.3.5. Focal mechanisms

We then focus on the statistics of the focal mechanism of aftershocks. To explore the possible focal mechanism of aftershocks, we relaxed the limitation of the orientation of the subsidiary faults, and the orientation has a uniform probabilistic density function for all angles. Fig. 3.10 shows the histogram of the angle of aftershock faults and their direction of slip. We can confirm that almost all events are confined within $\pm 15^{\circ}$ around the optimal angle of the prestress in the case of $\mu = 0.6$ (Fig. 3.10a). This is comparable to the variation in the orientation of the main fault. With the conventional rate and state friction and typical parameters, the stress rotation is negligible because the stress drop is small compared with the absolute stress (Hardebeck & Okada, 2018), and is not sufficient to activate less optimally oriented faults, even if fault roughness is present.

(a) $\mu_0 = 0.6$

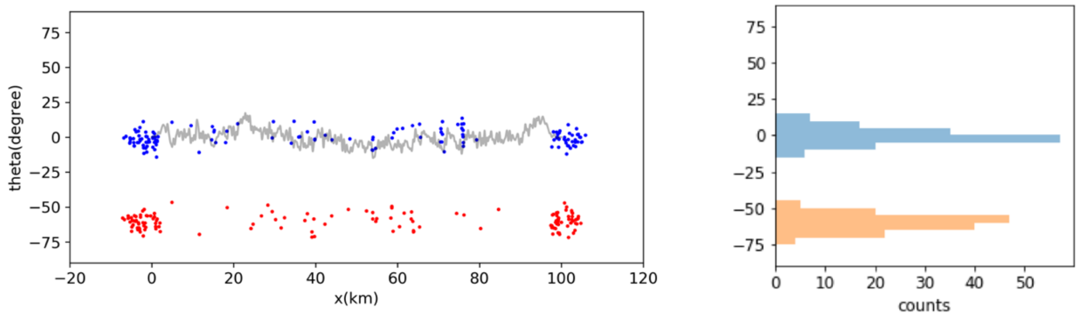

(b) $\mu_0 = 0.2$

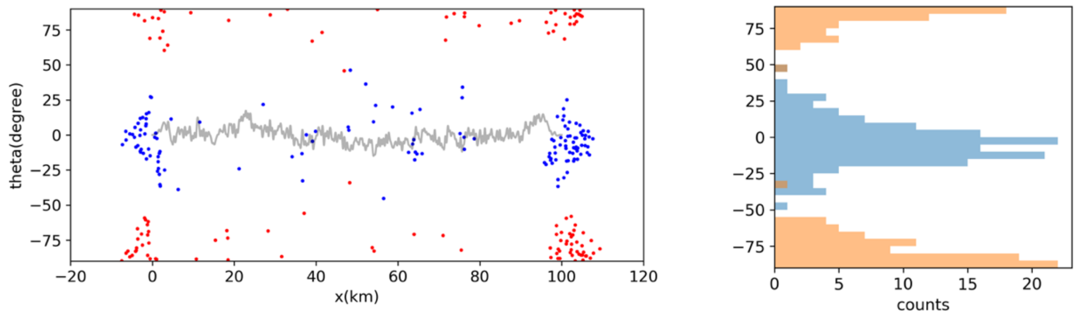

Figure 3.10. Distribution of fault angles that produced aftershocks. Two different background friction coefficients for the subsidiary faults are considered, and the background stress is changed according to the friction coefficient. Right-lateral slip is shown in blue and left-lateral slip is shown in red. The gray line represents the orientation of the main fault.

This is not the case when the fault is weak in terms of friction coefficient. We also run simulations with $\mu_0^s = 0.2$, in which a larger variation in focal mechanisms is present (Fig. 3.10b). The variation is far larger than that of the orientation of the main fault. This is because an almost complete stress drop occurs on the main fault. Interestingly, some less optimally oriented faults can slip in both directions. Local stress heterogeneity allows for reversal of slip direction of nearby faults, as sometimes seen in nature (Beroza & Zoback, 1993; Wang & Zhan, 2020).

We can also see that the fault-side aftershocks have a larger variation of focal mechanisms than fault-tip aftershocks because of larger stress heterogeneity. For fault-tip aftershocks, the variability decreases away from the tip. The stress jump due to mainshock decay with distance from the main fault, and therefore the range of the fault's orientations whose perturbed stress state reaches a failure threshold becomes narrower.

3.3.6. Magnitude distribution of aftershocks

Thus far, we have assumed the length of subsidiary faults as a constant as shown by geological observations and variability in aftershock magnitudes. Geological observations suggest that the length distribution of natural faults follows a power law (Bonnet et al., 2001; Scholz et al., 1993) and could be responsible for the power-law size distribution of earthquakes. In this section, we thus vary the length of subsidiary faults according to a band-limited power-law distribution. The density function of fault length L is given by

$$P(L) \propto L^{-2} \quad (0.15 \text{ km} < L < 5 \text{ km}). \tag{3.13}$$

This range is chosen by computational reasons. The characteristic slip distance d_c. on each fault is proportional to the length of the fault, and the number of computational elements for each subsidiary fault is constant. This choice is often made (Ide & Aochi, 2005), although we do this for computational reasons. Fig. 3.11a shows an example of the distribution of subsidiary faults.

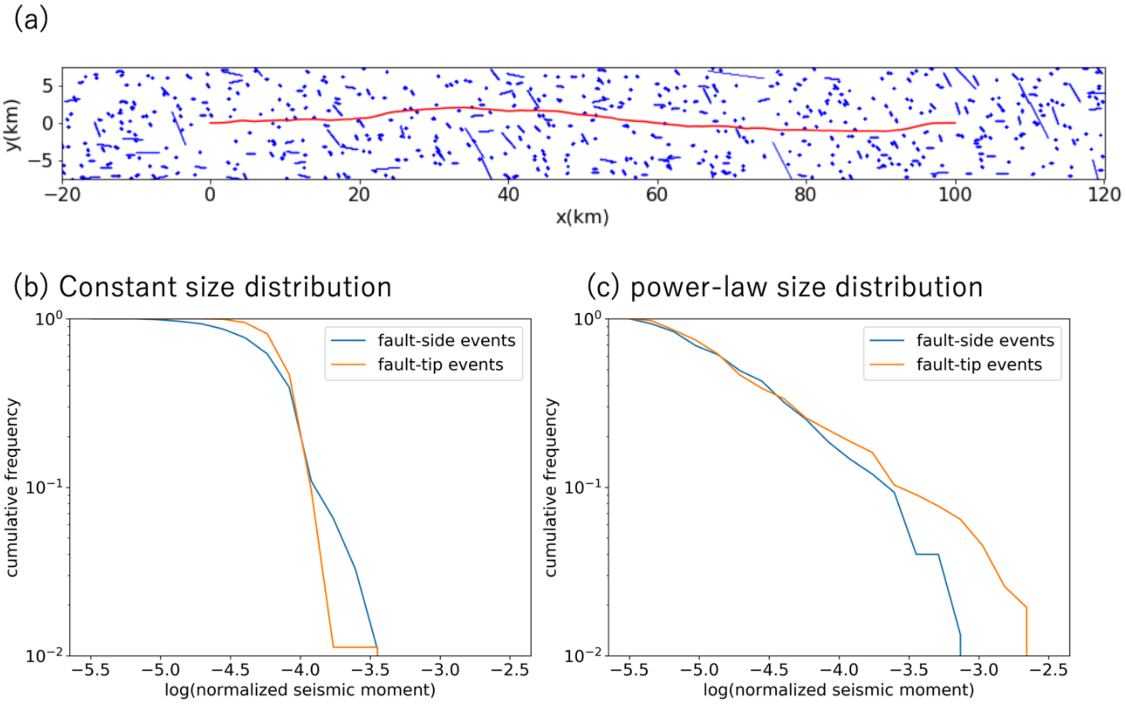

Figure 3.11. (a) Example of the fault geometry when the power-law length distribution of the subsidiary faults is taken into account. (b) Seismic moment versus cumulative number of events for the case of the constant subsidiary fault lengths. (c) Seismic moment versus cumulative number of events in the case of power-law subsidiary fault length distribution.

Because we did not find any significant difference between the uniform and power-law cases on the spatiotemporal statistics of aftershocks, we focus on the magnitude distribution of aftershocks, which shows difference. Fig. 3.11b and Fig. 3.11c shows the cumulative moment-frequency plot of aftershocks using 30 ensembles together, comparing the uniform and power-law distributions of subsidiary fault lengths. The seismic moment is computed by the sum of the element length times slip amount for all slipped elements, and is normalized by the mainshock moment. In the uniform subsidiary fault lengths, the magnitude-frequency plot shows a characteristic size distribution. The difference in the moment is mostly from the variation in the stress drop because the source area is constant. The stress drop variation comes from the normal stress and the heterogeneous stress from the mainshock. Fault side aftershocks seem to have a larger variation in seismic moment, possibly reflecting a more heterogeneous stress distribution.

In the power-law fault length distribution, as expected, the aftershock seismic moment obeys the Gutenberg-Richter relationship. In addition, we find that fault-side aftershocks include few large events ($>10^{-3.5}$ in the normalized seismic moment), whereas fault-tip events include large events. This is because fault-side aftershocks occur in a highly heterogeneous stress field and the rupture easily stops in regions where ΔCFF is negative (Aslam & Daub, 2018). In contrast, fault-tip aftershocks have the potential to grow large because ΔCFF is uniformly positive. Therefore, even if the fault-length distribution is uniform, the earthquake magnitude distribution can be spatially heterogeneous depending on the stress distribution, implying that the b-value of Gutenberg-Richter's law does not simply reflect the size distribution of faults.

3.4. Discussion

Our 2D numerical simulations have shown that realistic aftershock sequences can be obtained in a fault zone consisting of a rough main fault surrounded by many subsidiary faults. Specifically, we successfully reproduced fault-side aftershocks, the Omori-Utsu law, expansion of the aftershock zone, variations in focal mechanisms, and aftershock size distributions. We also show that rougher faults enhance fault-side seismicity, which is consistent with the experimental results of Goebel et al. (2017).

The important lesson from our model is that no aftershock occurs on the ruptured area of the mainshock fault plane, which is consistent with the observation that most aftershocks of the western Tottori earthquake are off-fault events (Yukutake & Iio, 2017). Nevertheless, the hypocenters of aftershocks delineate the main fault trace because the stress perturbation, and thus aftershocks, decreases as it moves away from the mainshock fault (Dieterich & Smith, 2009). This justifies, to some extent, the estimation of the fault plane length of the mainshock from well-constrained aftershock locations.

Recently, dynamic rupture simulations made to reproduce real earthquakes have shown that the overall behavior of the rupture can be reproduced if we know the fault geometry and initial stresses (e.g., Ando & Kaneko, 2018). Therefore, a next step for this type of models would be to reproduce not only the mainshock but also major aftershocks, although it would be difficult to precisely reproduce aftershocks due to the difficulty in knowing the geometry of smaller faults and high non-linearity of the earthquake generation process.

3.4.1. Aftershock clustering around the tips of the ruptured fault

Many observations show lower aftershock productivity in large slip areas in the mainshock (Beroza & Zoback, 1993; Chang & Ide, 2020; Das & Henry, 2003; Wetzler et al., 2018). For example, Wetzler et al. (2018) compiled the spatial distribution of aftershocks for a large number of subduction zone earthquakes and statistically found that aftershocks are clustered around the edges of the coseismic slip. However, the concentration is very weak or not present in some cases. Das & Henry (2003) suggested that this is because the stress concentration is "dull" due to various reasons. Our results show that fault roughness is a candidate. We also believe that the number of fault-tip events decreases further if the termination of the mainshock becomes more gentle (i.e., small gradient of the slip distribution) by a gradual increase in slip weakening distance closer to the fault tip.

Furthermore, we have shown that the largest aftershocks are limited in the fault-tips, by employing a power-law length distribution of the subsidiary faults. Although we have not performed a systematic investigation, in the 2017 Kaikoura earthquake, large aftershocks are clustered at the northern end of the mainshock rupture (Ando & Kaneko, 2018). This implies that the ratio of small to large aftershocks (i.e. b-value) is smaller for fault-tip events. This is consistent with the result by Wiemer & Katsumata (1999), who observed high b-values at the center of the mainshock rupture area surrounded by low b-value areas.

3.4.2. Stress heterogeneity

The choice of spatially uniform prestress condition is a simplification, as often assumed in dynamic rupture simulations (Ando & Kaneko, 2018; Aochi & Fukuyama, 2002). The prestress field depends on past earthquakes and any other slip events and should be heterogeneous (Duan & Oglesby, 2006; Manighetti et al., 2015). In addition, the spatial slip distribution in an earthquake often exhibits complexity, which cannot be captured from our model (see Fig. 3.7). This implies that there is additional heterogeneity in the prestress field other than traction heterogeneity produced from non-planar fault geometries (projection of uniform stress tensor onto local planes).

Because fault-side aftershocks reduce the local positive coulomb stress, they relax the strong stress heterogeneity induced by the mainshock (Dieterich & Smith, 2009; Scholz, 2019). Thus, aftershock processes could be regarded as viscous relaxation macroscopically, leading to a more homogeneous stress field before subsequent large earthquakes. For this reason, we can expect that the post-mainshock stress field is more heterogeneous than that of pre-mainshock, and the latter could play a minor role compared to the former in aftershock sequences. This can be justified by the observation of Trugman et al. (2020), who observed a step reduction in waveform similarity of neighboring earthquakes as a measure of the variability of stress field after the mainshock of the 2019 Ridgecrest sequence.

Fig. 3.12 shows a comparison of stress field between immediately after the mainshock, and after the aftershock sequence. An aftershock released a part of elevated σ_{xy} by the mainshock. However, simultaneously, this aftershock produces its own stress concentration on a smaller scale (Fig. 3.12). Therefore, this process is a highly multi-scale phenomenon (Helmstetter & Sornette, 2002; Marsan, 2005), and a more elaborate methodology is necessary to explore this scenario.

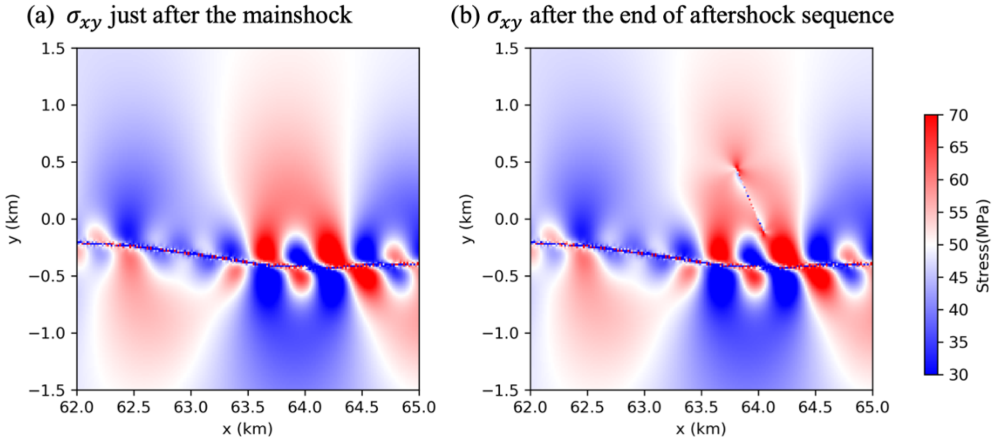

Figure 3.12. Distribution of σ_{xy} accounting for (a) only mainshock slip and (b) mainshock and all aftershock slip. Part of the large stress is relaxed by an aftershock, although the aftershock creates its own stress concentration.

3.4.3. Other Processes

Heterogeneous slip on a planar fault also leads to locations of positive coulomb stress on and at the side of the mainshock fault (Hainzl et al., 2010; Helmstetter & Shaw, 2006; Marsan, 2006). However, slip distributions in physics-based dynamic rupture simulations are smoother than those in observations at short-wavelength scales (Ampuero & Ben-Zion, 2008). In our simulations, despite the slip heterogeneity being weak (see Fig. 3.7), the Coulomb stress field is highly heterogeneous owing to the fault roughness.

Although it would be not majority, some aftershocks may be rerupture of the mainshock fault. Several earthquake sequence models add frictional heterogeneity (a mixture of velocity-weakening and -strengthening regions) to produces on-fault aftershocks. For example, Yabe & Ide (2018) were successful in reproducing on-fault aftershocks for a single planar fault by varying the sign of $a - b$. Kaneko & Lapusta (2008) also studied the earthquake nucleation process and aftershock sequences in the transition zone of $a - b$. Barbot (2019b) and Cattania (2019) observed Omori-like aftershock events around the transition zone of locked and creeping segments. The segmentation of locked and creeping areas is often observed in megathrust and transform faults. In such a case, frictional heterogeneity may be important. The observation of Omori-like decay of repeating aftershocks after the 1989 Loma Prieta earthquake in the San Andreas fault is one plausible example (Schaff et al., 1998). In contrast, the existence of velocity-strengthening area is not trivial for immature intraplate faults because stable creep is not universally observed (Harris, 2017). Our model can incorporate spatially heterogeneous friction parameters, so we will address this question in the future.

Velocity-strengthening friction also produces afterslip (Marone et al., 1991). Several studies suggest that afterslip plays an important role in triggering aftershocks (Cattania et al., 2015; Perfettini & Avouac, 2004; Schaff et al., 1998). The difficulty in discriminating the nucleation and afterslip models is attributed to the fact that the mathematical forms of the evolution of aftershock activity are exactly the same (Perfettini & Avouac, 2004). With a log-time increase or decrease of stress during the postseismic period, in addition to coseismic stress jump, the p-value can take larger or smaller values than one assuming uniform stress (Dieterich, 1994). Because the afterslip distribution is often different from the coseismic slip distribution, the spatial distribution of aftershocks could also change, which should be studied in more details. It is also notable that the expansion of the aftershock zone can also be explained by afterslip (Kato, 2007; Perfettini et al., 2018).

We used the random fault roughness as a representative characteristic of the geometrical complexity of faults, but the geometry of natural faults is not characterized only by fractals. For example, natural faults typically consist of several discontinuous segments (Manighetti et al., 2015). Stress will be concentrated at segment boundaries, which is expected to drive aftershocks.

Our model is 2D, and therefore, all events are purely strike-slip if this geometry is considered as map view. In 3D, normal and reverse faulting could occur depending on the local geometry of the main fault, which could contribute to the relaxation process of stress heterogeneity. Additionally, slip direction (rake angle) could be heterogeneous on the mainshock fault, which may reflect 3D fault geometries. Altogether, due to the constraint on slip direction of both main and subsidiary faults, we speculate that our 2D inplane model of nonplanar faults could exaggerate some results of the 3D case. Thus, 3D simulations need to be performed in the future.

We used the aging law for state evolution. However, the slip law is also often used, and some studies suggest that it is more consistent with laboratory experiments (Bhattacharya et al., 2015). Heimisson & Segall (2018) showed that the slip law predicts faster aftershock decay than the aging law, so it could change the temporal decay of aftershocks.

It has long been argued that a significant fraction of aftershocks is triggered by dynamic stress even for near field aftershocks (Felzer & Brodsky, 2006). Because our model is quasi-dynamic, dynamic stress is not accurately modeled. The stress field near the rupture front is distorted due to dynamic effects (Poliakov et al., 2002; Rice et al., 2005), and thus there may be some quantitative changes if the full inertia effects are taken into account.

4. Efficiency of rupture barriers caused by fault bends

4.1. Introduction

There is growing evidence for earthquake rupture terminations correlated with fault bends (King & Nábělek, 1985). For example, the last great earthquake on the Altyn Tagh fault, China, was terminated around a restraining bend (Elliott et al., 2015). Both ends of the surface rupture of the recent 2021 Mw 7.4 Maduo, China, earthquake correspond to a releasing bend (Jin & Fialko, 2021). The 1999 Mw 7.2 Dunze earthquake on the North Anatolian fault, Turkey, was arrested around a releasing bend (Duman et al., 2005). However, major fault bends do not always act as a barrier to rupture propagation. In the 1999 Mw 7.4 Izmit earthquake, which occurred four months after the Dunze earthquake at the neighboring segment of the North Anatolian fault, a 25° restraining bend did not stop the rupture (Harris et al., 2002). The 2018 Mw 7.5 Palu earthquake, Indonesia, propagated a major releasing bend with a supershear rupture speed (Okuwaki et al., 2020).

Biasi & Wesnousky (2017) compiled surface rupture traces of 67 historical earthquakes worldwide to show that the possibility of rupture passing the bend systematically decreases with the angle of the bend. For strike-slip ruptures, the passing ratio PR (ratio between passing ruptures and stopping ruptures) is approximately $PR=3.1-0.083\theta$ in the range $5^\circ < \theta < 30^\circ$, where θ is the bend angle. They also found that dip-slip ruptures are more likely to pass a bend for the same angle. The maximum bend angle that can be passed is ~30° for a strike-slip rupture and ~50° for a dip-slip rupture, respectively. Along with a similar empirical law for stepovers (Biasi & Wesnousky, 2016), this empirical law has been used in probabilistic seismic hazard assessment (Biasi & Wesnousky, 2021).

There are a lot of numerical studies focusing on the effect of faults' nonplanar geometries on rupture arrests on fault bends. Dynamic rupture simulations have been performed to address this problem (Aochi et al., 2000; Kase & Day, 2006; Lozos et al., 2011). Through parameter studies, they discussed the conditions that stop rupture propagations. For example, Lozos et al. (2011) performed dynamic rupture simulations on a fault that contains a restraining and releasing bend and found that a restraining bends larger than 18° and releasing bends larger than 34° stop the rupture. However, single dynamic rupture simulations must assume the initial condition, and the assumed initial condition does not necessarily arise in the earthquake cycle. Also, a single run of dynamic rupture simulations cannot address the question that how often a rupture is arrested at a given fault bend. On the other hand, earthquake sequence simulations are free from the assumption regarding the initial conditions and have the capability of addressing how often a rupture is arrested. For example, Duan & Oglesby (2005) studied the stress evolution and slip pattern of ruptures on a fault with a kink, although their model does not track the interseismic evolution of the slip rate.

A problem in earthquake sequence simulations specific to nonplanar faults is the change of normal stresses (Dieterich & Smith, 2009; Tal et al., 2018). Romanet et al. (2020) showed that the stress change on the fault can be decomposed into two terms: the slip-gradient term and the curvature term. The former is proportional to the spatial gradient of the slip and the latter is proportional to the product of local curvature and slip (= vanishes on a planar fault). If the deviation from planarity is small, the shear stress is dominated by the gradient term and the normal stress is dominated by the curvature term. Hence, on a nonplanar fault, the normal stress heterogeneity monotonically grows with accumulating slip. This eventually leads to fault opening or unrealistically large normal stresses. Because of this issue, many earthquake simulations on nonplanar faults neglect the normal stress changes (Li & Liu, 2021; Ohtani et al., 2014).

This pathological result comes from the assumption of the linear elastic off-fault medium, but the real rock is not purely elastic. Dynamic rupture simulations on a rough fault show that the opening (tensile stress) is prevented with Drucker-Prager type off-fault viscoelasticity, although the unreasonably high normal stresses cannot be prevented in their model (Dunham et al., 2011b). We speculate that other processes such as pressure solution creep and pore collapse could contribute to limiting large normal stresses. Furthermore, the use of a 2D model limits the sense of slip to purely strike-slip components. In the actual crust, slip on nearby normal and reverse faults (and also the main fault itself especially if it is not vertical) could remove the normal stress heterogeneity by uplift or subsidence. Transpressive and transtensional duplexes observed in strike-slip faults are the signatures of such mixed-mode deformations (Woodcock & Rickards, 2003).

As such, a 2D nonplanar fault within a purely elastic medium can be an unrealistic representation of a natural fault, although explicitly modeling aforementioned off-fault deformation (including the slip on not-explicitly modeled faults) is computationally challenging. In this work, to mimic the effect of the aforementioned process while keeping our numerical model simple, we use a simple linear stress relaxation. This is somewhat similar to the work by Duan & Oglesby (2005), D. Liu et al. (2021), and Nielsen & Knopoff (1998), although they are not earthquake sequence simulations in the sense that they do not track the evolution of the slip rate during the interseismic period with the rate and state friction framework.

In this work, we perform earthquake sequence simulations on two parallel planar faults connected by restraining and releasing bends. Using a stress relaxation method to ensure the long-term steady stress state, we address the statistics of the rupture arrest on the fault bends. We will show that the passing probability of a rupture encountering a bend is primarily a decreasing function of the bend angle, and other parameters have secondary importance.

4.2. Model

We use 2D plane strain models. The medium is a homogeneous and isotropic elastic full space. Numerical simulations are performed using a quasi-dynamic boundary element method accelerated with H-matrices (see **Chapter 2** for the detail), in which the stress change on the fault trace is written by

$$\Delta\sigma_{ij}(s) = \int K_{ij}(s,\xi)\Delta u(\xi)d\xi, \tag{4.1}$$

where $\Delta\sigma_{ij}$ is the change of stress tensor, K_{ij} is elastic integration kernel (Appendix A), Δu is the shear slip (right-lateral is positive). We use the regularized rate and state friction law, and the state evolution is governed by the aging law (Dieterich, 1979; Rice et al., 2001; Ruina, 1983), in which

$$\frac{\tau}{\sigma} = a\operatorname{arcsinh}\left(\frac{V}{2V_0}e^{-\phi}\right), \tag{4.2}$$

$$\frac{d\phi}{dt} = \frac{b}{d_c}\left[V_0\exp\left(\frac{f_0-\phi}{b}\right) - V\right], \tag{4.3}$$

where τ is shear stress, σ is normal stress, V is slip rate, ϕ is state variable, f_0 is the reference friction coefficient, a is the coefficient of the direct effect b is the coefficient of the evolution effect, and d_c is the characteristic slip distance. Parameter values are shown in Table 4.1.

4.2.1. Fault geometry

A fault surface contains a restraining or releasing bend. The shape of the fault is given by (Fig. 4.1)

$$y = \alpha\tanh\left(\frac{x - x_{bend}}{W}\right). \tag{4.4}$$

The maximum angle of the bend against the x-axis is $\theta = \tan^{-1}(\alpha/W)$ at $x = x_{bend}$. This geometry gives the local maximum/minimum of normal stress at $x = x_{bend}$. The fault (double-)bends were modeled as abrupt kinks by Lozos et al. (2011), while we use smooth curves. We emphasize that typical restraining and releasing bends are more gradual curves rather than straight segments with kinks (Mann, 2007).

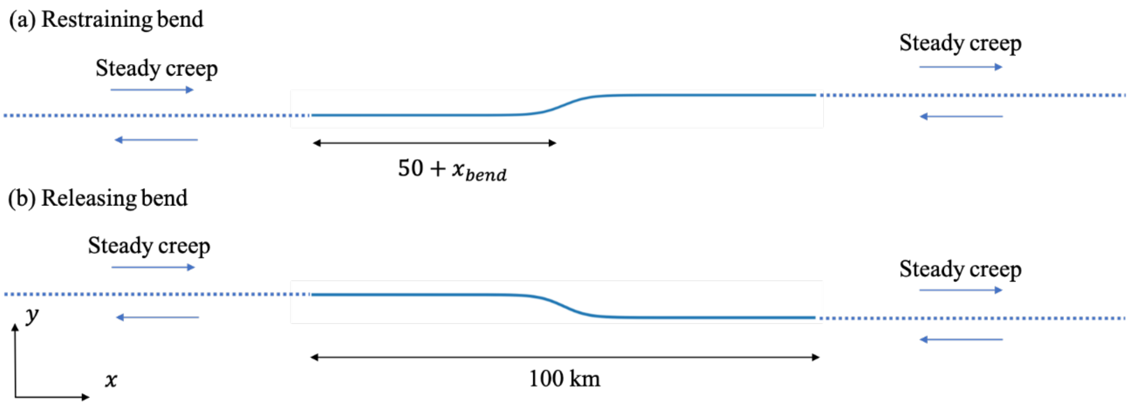

Figure 4.1. The fault geometry, loading condition, and coordinate system.

4.2.2. Loading condition

We assume that the fault is loaded by the steady creep on the extension of the fault surface (dotted sections in Fig. 4.1). The stressing rates are calculated from the semi-infinite straight elastic dislocations, namely

$$\dot{\sigma_{ij}}(s) = V_{pl} \int_{-\infty}^{s_0} K_{ij}(s,\xi) d\xi + V_{pl} \int_{s_1}^{\infty} K_{ij}(s,\xi) d\xi \,. \tag{4.5}$$

where s and ξ are the locations of the receiver and source measured by the fault trace, and s_0 and s_1 are the left and right ends of the computational domain, respectively. Following Romanet et al. (2020), we rewrite equation (4.5) as

$$\begin{aligned} \dot{\sigma_{ij}}(s) &= V_{pl} \int_{-\infty}^{\infty} K_{ij}^{grad}(s,\xi) \frac{\partial}{\partial \xi} \big(H(\xi - s_1) - H(\xi - s_0) \big) \mathrm{d}\xi \\ &= V_{pl} \left(K_{ij}^{grad}(s, s_0) - K_{ij}^{grad}(s, s_1) \right). \end{aligned} \tag{4.6}$$

We used the fact that $K_{ij}^{grad}(s, \pm\infty)$ is zero. The curvature term vanishes because straight dislocations are assumed. We compute the stressing rate of each element using equation (4.6).

4.2.3. Stress relaxation to a background stress field

We add a time-dependent stress relaxation term for shear and normal stresses as follows:

$$\frac{d\sigma}{dt} = -\frac{\sigma - \sigma_0(s)}{t_{relax}} \tag{4.7}$$

$$\frac{d\tau}{dt} = -\frac{\tau - \tau_0(s)}{t_{relax}} \tag{4.8}$$

Where t_{relax} is the characteristic relaxation time, σ_0 is the background normal stress and τ_0 is the background shear stress. The background shear and normal stresses are resolved from spatially uniform background stress that is determined by the following condition. We set σ_{yy}^0 to be 75 MPa and $\sigma_{xy}^0 = \mu^0 \sigma_{yy}^0$ with $\mu^0 = 0.55$. Also, we assume that x-axis (overall fault direction) has the angle $\Psi = 30^\circ$ (optimal for coulomb failure) or $\Psi = 45^\circ$ (maximum shear) for coulomb failure. Hence, σ_{xx}^0 is calculated by (Dunham et al., 2011a)

$$\sigma_{xx}^0 = \left[1 - \frac{2\sigma_{xy}^0}{\sigma_{yy}^0 \tan(2\Psi)}\right]\sigma_{yy}^0. \tag{4.9}$$

The value of t_{relax} is difficult to be constrained from observational or microphysical perspectives. It is also unclear whether exponential relaxation is a good approximation of the real crust. However, for the proof of concept, we need to choose t_{relax} as larger than the recurrence interval of ruptures not to relax the changed stresses rapidly and short enough not to have unrealistic large normal stresses. In addition, we do not allow tensile normal stresses and truncate the minimum normal stress on the fault to 10MPa. This procedure is motivated by the fact that dynamic rupture simulations on a fractally rough fault with off-fault plasticity prevent the releasing bend of a fault from having tensile normal stresses (Dunham et al., 2011b).

Fig. 4.2 shows the evolution of normal stress at the bend center in the case of $x_{bend} = 0$ and $W = 5$ km, where the normal stress takes maximum or minimum since the sign of the fault curvature is zero (Romanet et al. 2020). The case of a 20° restraining bend shows that, in the first few earthquake cycles, the normal stress increase from the initial (background) value during the coseismic periods. Eventually, the relaxation term resists the increase, and the value reaches a long-term steady state. The steady-state value increases with increase of t_{relax}. In the case of releasing bends, the normal stress reaches the artificial limit (10MPa) after a few earthquake cycles unless t_{relax} is not too short.

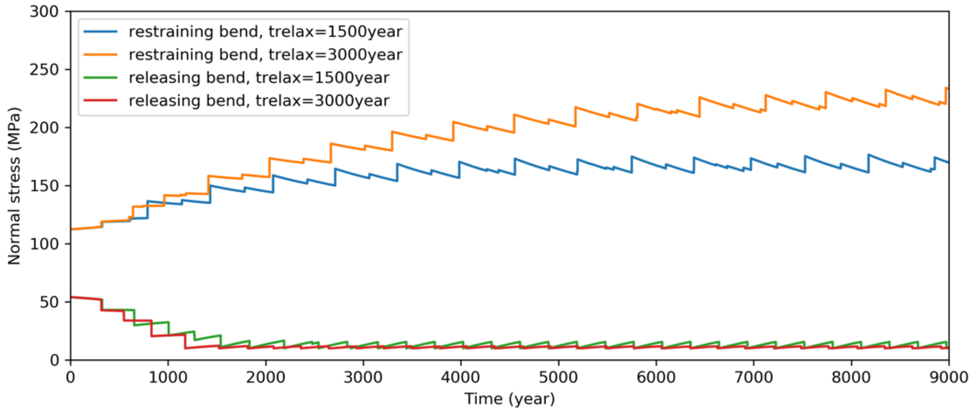

Figure 4.2. The time evolution of the normal stresses at the center of the bend with different t_{relax}. The case of 20° restraining and releasing bends are shown.

Table 4.1: Parameters

Parameter	Description	Value
G	Shear modulus	32.04 GPa
ν	Poisson's ratio	0.25
V_s	Shear wave speed	3.464 km/s
σ_{yy}^0	Background stress	75 MPa
μ	Background friction	0.55
Ψ	Maximum compressive angle of background stress	30° or 45°
a	Rate state parameter	0.016
b	Rate state parameter	0.02
d_c	State evolution distance	Variable
t_{relax}	Relaxation time	Variable
V_0	Reference slip rate	1 nm/s
μ_0	Reference friction coefficient	0.60
x_{bend}	Centeral location of the bend	Variable
θ	Angle of the bend	Variable
W	Charactersitc width of the bend	Variable

4.3. Simulation Results

4.3.1. Examples of Simulation Results

First, we show the result using a planar fault as a reference. Previous studies show that with this type of loading procedure, the system behavior is mainly controlled by the ratio of the velocity-weakening (VW) domain size and nucleation size (Barbot, 2019b; Cattania, 2019). Thus, in Fig. 4.3 we also compare the results of three d_c values, which is proportional to the nucleation size. In all cases, the unlocking (creep front) of the fault begins with the edge of the VW area. In the case of d_c=0.01 m (Fig. 4.3a), both full ruptures and partial ruptures confined in the edge of the VW area occur. It is well-known complexity in a larger fault/nucleation size ratio (Cattania, 2019). In the case of d_c=0.025 m (Fig. 4.3b), only full ruptures occur periodically. The hypocenters are the edges of the VW zone, which is similar to the case of d_c=0.01 m. In the case of d_c=0.06m (Fig. 4.3c), a dynamic slip begins by the coalescing of two creep fronts seen as the narrow blue green bands. In this case, a significant amount of slip is accommodated aseismically (Barbot, 2019b). Hereafter, we focus on the case of the intermediate d_c range (~0.025m) as it is simple and realistic.

We next show simulation results with restraining bends with $x_{bend} = 0$km and $W = 5$km (Fig. 4.4). As similar to the planar case, most ruptures begin at both edges of the VW zone. However, part of ruptures is arrested around the restraining bend, producing left-segment ruptures and right-segment ruptures. Because the slip area of the left-segment ruptures and right-segment ruptures are not overlapped, the concentrated shear stress at the bend will allow for the occurrence of a full rupture after several partial ruptures (i.e., the bend acts as a conditional barrier). Although the majority of the arrest location is around the bend, some ruptures are arrested other than the bend even though there are no partial ruptures in the case of a flat fault with identical parameters. This is presumably caused by the elastic long-range interaction.

Even if a rupture front does not stop at the bend, it usually slows down around the bend (see Fig 4.4b). If the deceleration of a rupture at the bend is significant, the rupture process is observed as a sequence of two events (see Fig. 4.4a). The first event is arrested at the bend, while the second event nucleates around the arrest location and propagates bilaterally. Therefore, the bend becomes the hypocenter of some events as observed in nature (King & Nábělek, 1985).

The cases of releasing bends also show rupture terminations around the bend (Fig. 4.5). Most ruptures break through the bend for the 10º and 20º bends, while most ruptures are arrested at the bend for the 30º and 40º cases. A difference from the restraining bend is that the slip area of left-segment and right-segment ruptures are overlapped around $x = 0$ (compare Figs. 4.4c-d and 4.5c-d). That is, the center of the bend slips both-segment ruptures. The mechanical origin of this difference will be discussed later.

Another important output of our numerical simulations is the spatial distribution of the long-term slip. Fig. 4.6 shows the spatial distribution of the cumulative slip during $2 \cdot 10^{11}$ seconds. The long-term slip rate is controlled by tectonic loading and stress relaxation. Planar faults show an almost uniform long-term slip rate, which is the same as the creep velocity of the external segment. On the other hand, fault bends decrease the slip rate. In an extreme case (40º restraining bend), the fault is always stuck, and no slip occurs. Due to elastic long-range interaction, the slip rate of the neighborhood of the bend also decreases. The gradual decrease of the long-term slip rate toward a restraining bend agrees with the observational geologic slip rate on the Altyn-Tagh fault as already mentioned (Elliott et al. 2018).

(a) dc=0.01 m

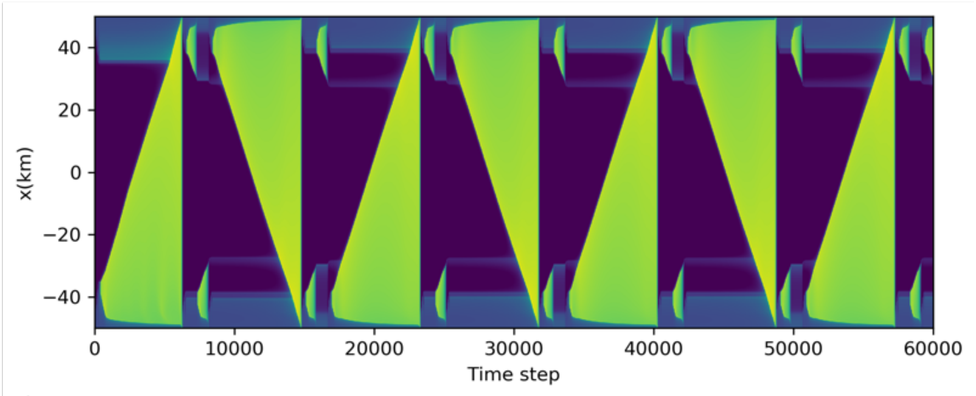

(b) dc=0.025 m

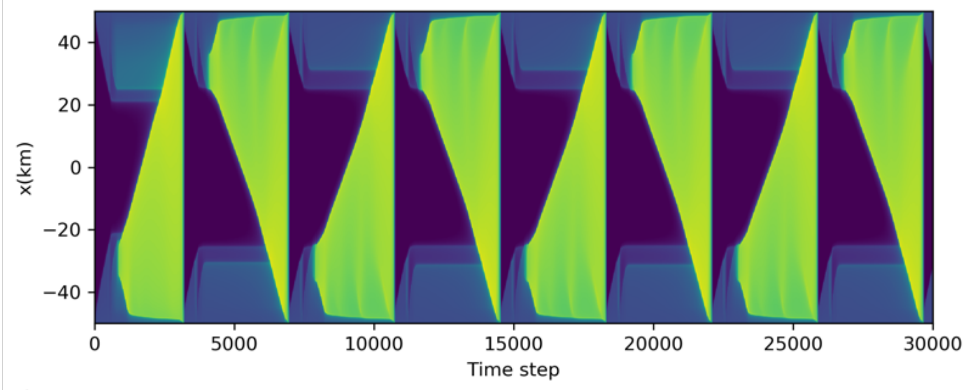

(c) dc=0.06 m

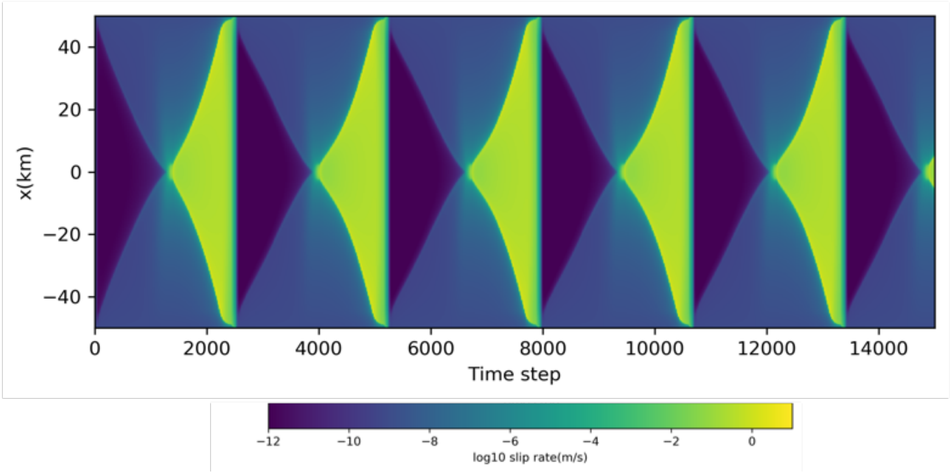

Figure 4.3. Simulation results with planar faults comparing different d_c values. Colors shows the temporal progress of the slip rate on the fault. Note that the horizontal axis is the time-step (not the actual time) and the actual time interval in a time-step is variable and roughly inversely proportional to the slip rate.

(a) 10° restraining bend

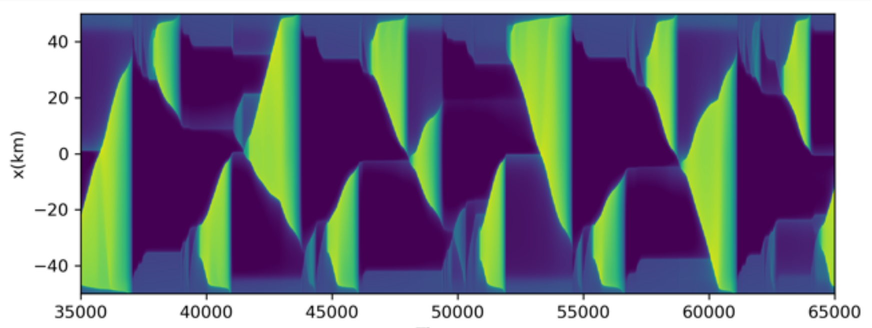

(b) 20° restraining bend

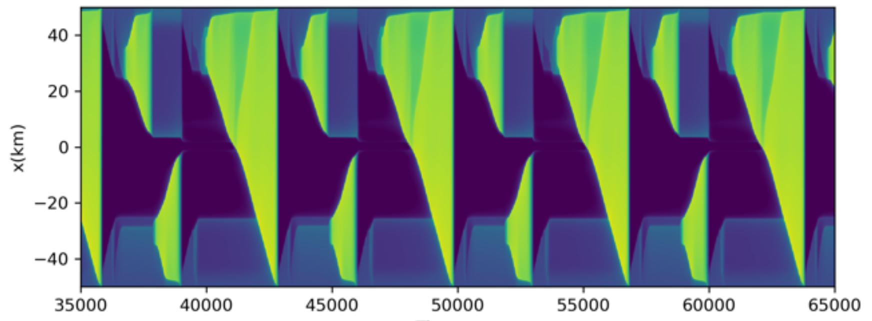

(c) 30° restraining bend

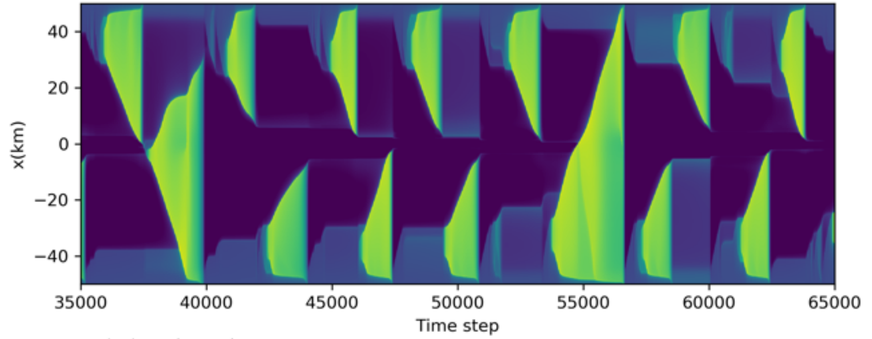

(d) 40° restraining bend

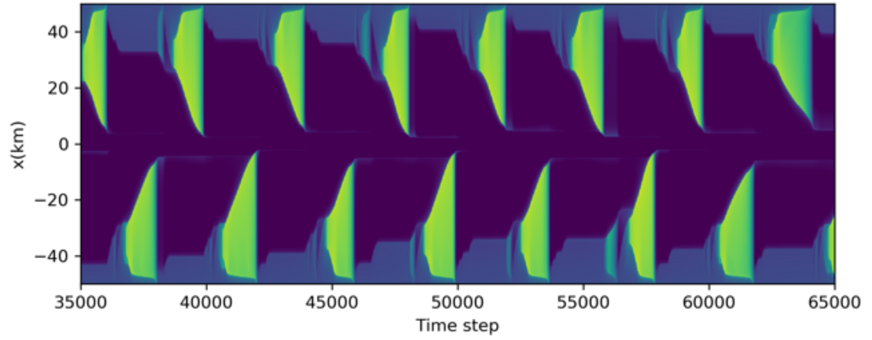

Figure 4.4. Simulation results for restraining bends with different angles. The parameters are $x_{bend} = 0$ km, $W = 5$ km, $d_c = 0.025$ m, $t_{relax} = 1500$ yrs.

(a) 10° resleasing bend

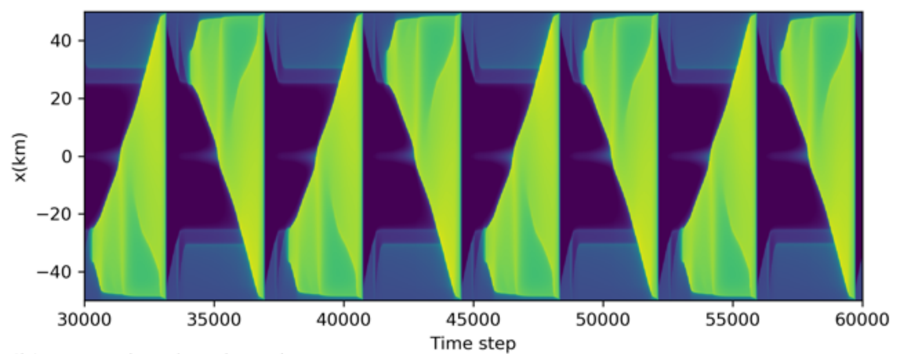

(b) 20° releasing bend

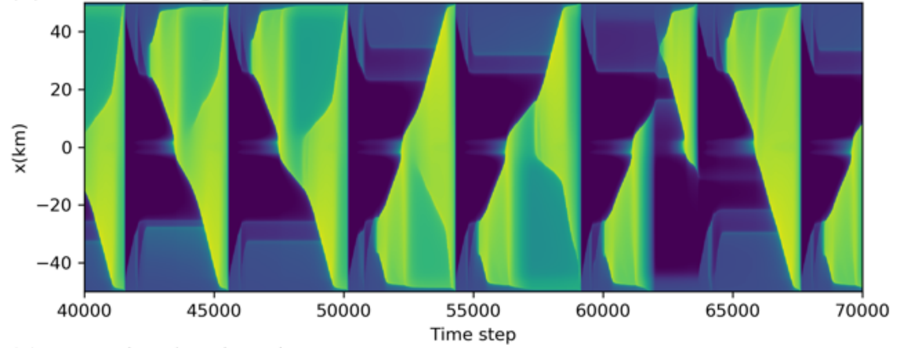

(c) 30° releasing bend

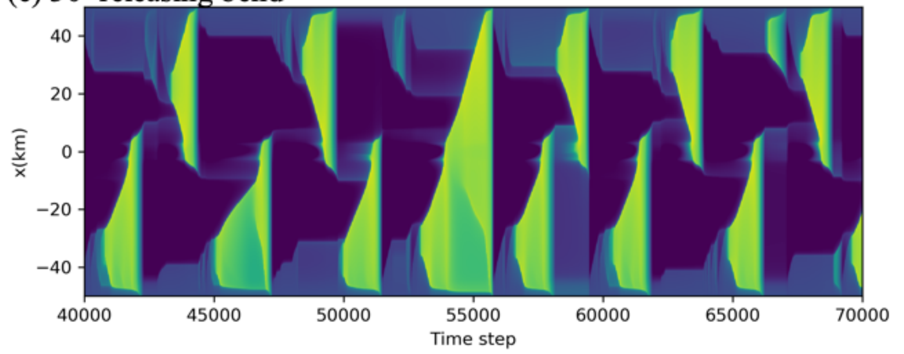

(d) 40° releasing bend

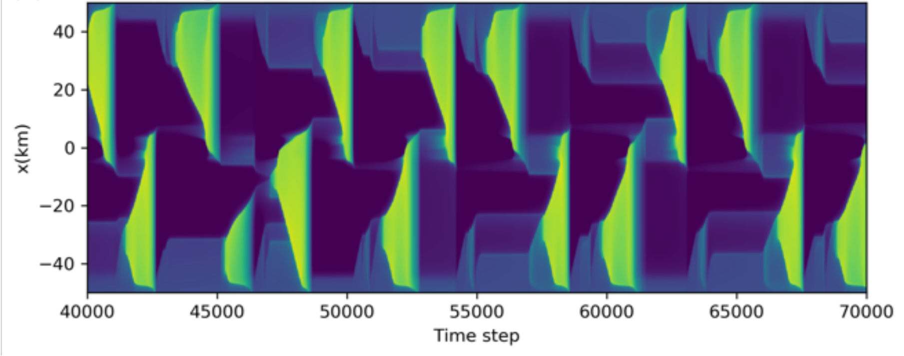

Figure 4.5. Simulation results for releasing bends with different angles. The parameters are $x_{bend} = 0$ km, $W = 5$ km, $d_c = 0.025$ m, $t_{relax} = 1500$ yrs.

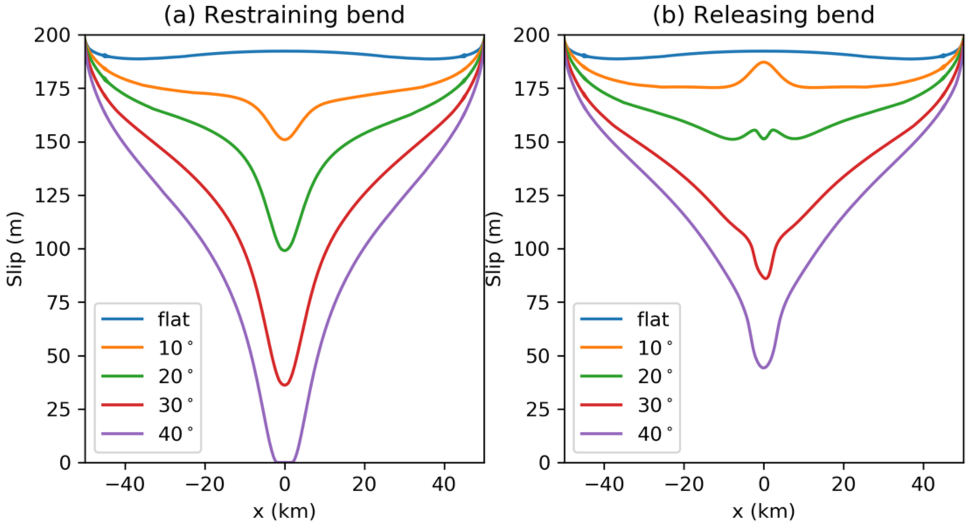

Figure 4.6. Long-term slip distributions for different bend angles from 0º (flat) to 40º. The cumulative slip during 2×10^{11} sec.

4.3.2. Passing probability statistics

We varied the following parameters: (1) bend angle (-45º to 45º), (2) background stress angle (30º or 45º), (3) the width of the bend (2 to 8 km), (4) location of the bend (0 to 25 km), (5) state evolution distance (0.015 to 0.03 m), (6) relaxation time ($3 \cdot 10^{10}$ to 10^{11}sec). We performed 400 simulations using randomly chosen sets of six parameters.

To consider the statistical properties of our simulated earthquake sequences, we compute the passing probability as follows:

1. Define the period of each rupture event with the condition that the maximum slip rate on the fault $V_{max} > 3$mm/s.
2. Compute the slip distribution of each rupture during the rupture period and obtain the left and right ends (x_l, x_r) of slip area with the condition that slip is larger than 1cm.
3. Classify the events into passing ruptures, stopping ruptures, and irrelevant ruptures by the rupture region using the following criterion. Passing ruptures are $x_l < x_{bend} - 2W, x_r > x_{bend} + 2W$. Irrelevant ruptures are $x_r < x_{bend} - 2W, x_l >$

$x_{bend} + 2W$. The rest ruptures are stopping ruptures. Examples of the slip distributions and event classifications are shown in Fig. 4.7.

4. Compute the passing probability with $PP = N_{full}/(N_{full} + N_{stop})$ using the event catalog after $1.5t_{relax}$.

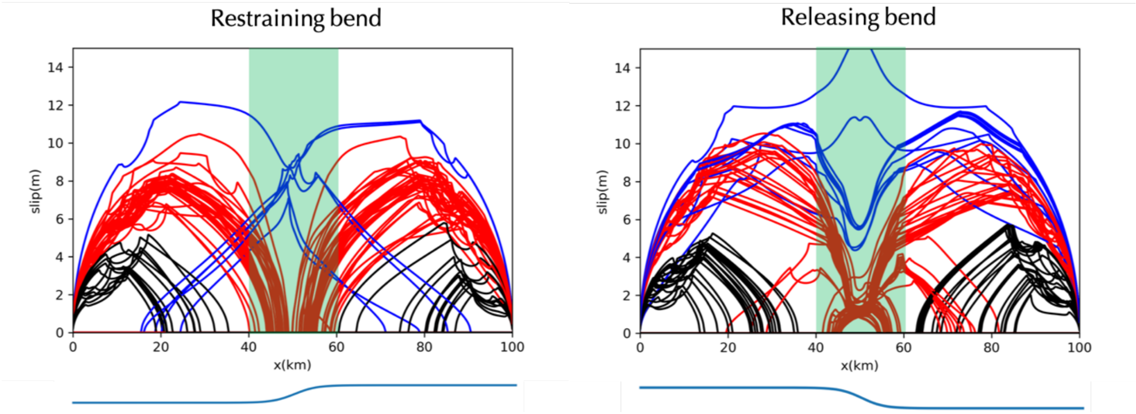

Figure 4.7. Examples of slip distribution of each event obtained by the procedure 1.-3. The left and right panels are a 20º restraining bend and a 20º releasing bend, respectively. Passing ruptures are shown in blue. Stopping ruptures are shown in red. Irrelevant ruptures are shown in black. The green area represents the region $x_{bend} - 2W < x < x_{bend} + 2W$. Ruptures arrested in this region are classified into stopping ruptures.

We computed the passing probabilities for 400 parameter sets and examined which parameter controls the passing probabilities. At least in the parameter range explored in this work, we find that the bend angle is the most important parameter. Fig. 4.8 shows all results. Although there is scatter, the passing probability generally decreases with increasing the bend angle. For larger angles (>30º), both bends act as a nearly permanent barrier ($PP \ll 1$). For smaller angles, restraining bends have a smaller passing probability than releasing bends, as observed in previous dynamic rupture simulations (Lozos et al. 2011). For a given bend angle, releasing bend usually have more variation in the passing probability than restraining bends. It should also be noted that restraining bends usually act as conditional barriers ($0 < PP < 1$), while releasing bends often act as either non or permanent barriers ($PP{\sim}0$ or $PP{\sim}1$). This difference may be related to the typical location of the rupture termination (overlap of the left and right segment ruptures).

The background stress angle is also important as seen from the two colors of Fig. 4.8. Because the stress on the fault relaxed toward the background stress, how much the bent segment is optimally oriented to the background stress controls the interseismic evolution of the stress state. In the case of “maximum shear (45º)”, a 15º releasing bend makes the optimal angle against the background stress. Therefore, the passing probability is shifted leftward than the “optimal (30º)” case.

The other four parameters have secondary effects as shown in Fig. 4.9, although some tendeicies could be seen. For example, noncentered releasing bends (larger x_{bend}) facilitate conditional barriers than centered releasing bends (Fig.4.9a) and larger d_c leads to a smaller PP (Fig 4.9d). For restraining bends, we could not see a systematic effect by these four parameters, probably because the complex interaction of the several parameters obscures their effects.

Finally, in Fig. 4.10 we directly compare our dataset with the data by Biasi & Wesnousky (2017). As they do not distinguish restraining and releasing bends, we take average the restraining and releasing bends. They are generally in good agreement, though our PP is systematically lower than the observational data. Note that our model presumably has some bias since we specifically assume the geometry of the bend (tangent-hyperbolic double-bend) and the loading condition. Also, our 2D and quasi-dynamic model may introduce some biases. Further numerical simulations are necessary in the future.

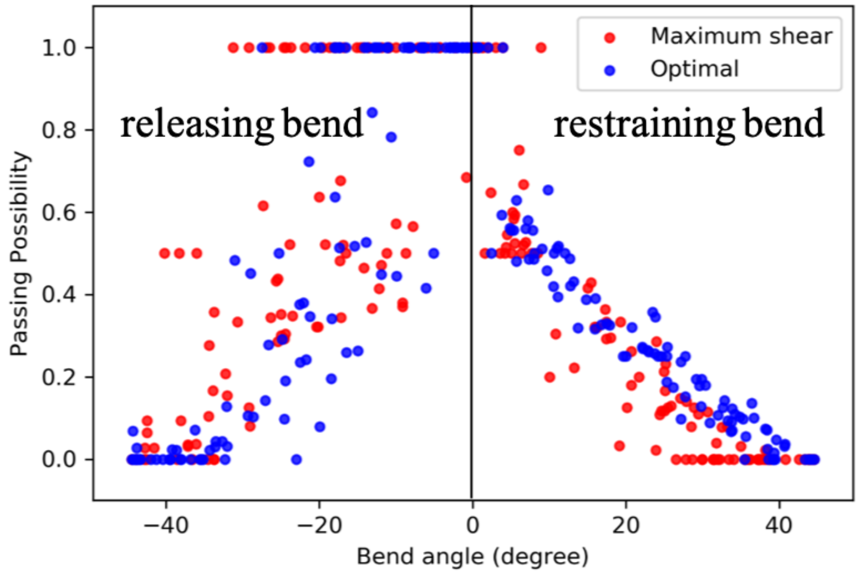

Figure 4.8. Passing probability statistics. Two background stress conditions; “maximum shear” corresponds to $\Psi = 45^\circ$ and “optimal” corresponds to $\Psi = 30^\circ$. The positive and negative bend angles correspond to restraining and releasing bends, respectively.

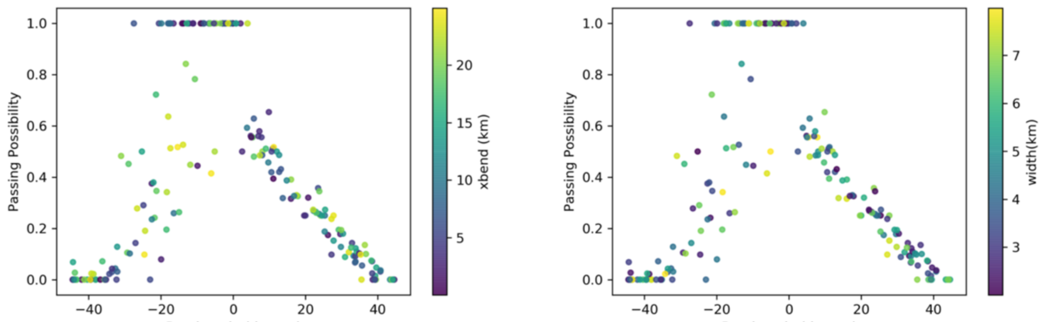

(a) location of the bend

(b) width of the bend

(c) relaxation time

(d) state evolution distance

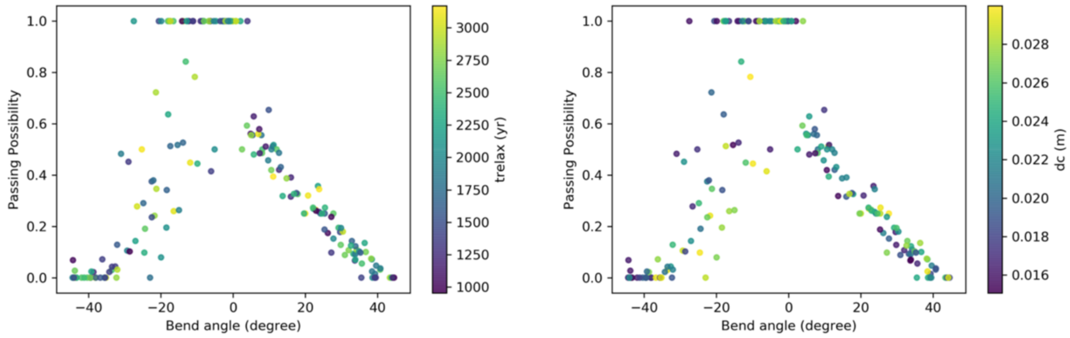

Figure 4.9. Passing probabilities with the case of "optimal" setting. Each symbol represents a numerical model with randomly selected parameters ($x_{bend}, W, t_{relax}, d_c$). All plots use the same data but the color represents (a) location of the bend x_{bend}, (b) width of the bend W, (c) relaxation time t_{relax}, and (d) state evolution distance d_c, respectively. The positive and negative bend angles correspond to restraining and releasing bends, respectively.

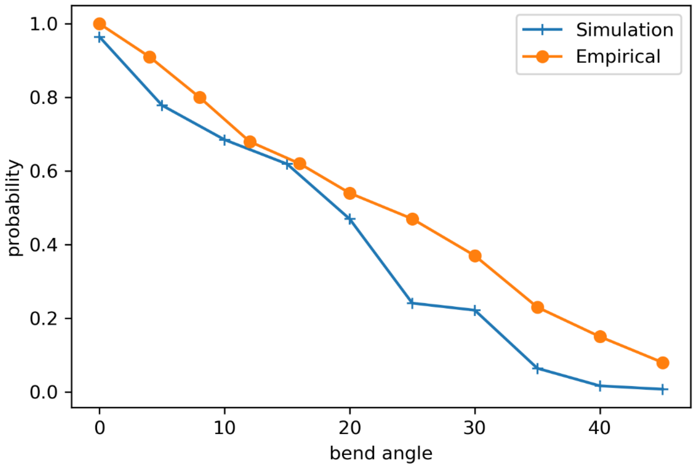

Figure 4.10. Passing probabilities. The numerical simulations are averaged over 400 parameter sets (the original data is shown in Fig. 4.8). The empirical is given by Biasi & Wesnousky (2017).

4.4. Discussion

4.4.1. Arrest mechanisms at restraining and releasing bends

Using numerical simulations, we have examined the occurrence of partial and full ruptures in a rate-state fault containing a restraining and releasing bend. Despite the 2D and quasi-dynamic nature of our numerical simulations, our result show rough agreement with the empirical law of passing probabilities by Biasi & Wesnousky (2017, 2021) over a wide range of parameters.

Although our numerical simulation is quasi-dynamic, we can qualitatively discuss the mechanism of rupture arrest due to fault bends using the concept of the Griffith's energy balance. In this concept derived from fracture mechanics, a rupture is arrested when the fracture energy exceeds the static energy release rate. In a planar fault with spatially uniform stress drop, the energy release rate is proportional to the rupture length, thus a rupture is difficult to be arrested. To hinder rupture propagations, a rupture must enter a region having (1) a very small or negative stress drop or (2) very large fracture energy. The former is determined by the prestress state (potential stress drop). The latter is roughly proportional to the normal stress given the aging law could be approximated as slip weakening law during the rupture process (Bizzarri & Cocco, 2003).

Fig. 4.11 shows an example of the distributions of potential stress drop and normal stress for a stopping rupture. In the case of restraining bends, as approaching the center of the bend ($x = 0$), the potential stress drop becomes smaller because it is misoriented from the regional stress field. Also, the normal stress increases due to the curvature effect. Both of them facilitate the rupture arrest. Because the ruptures of the left and right segments are not overlapped, the center of the bend accumulates elastic stress, causing occasional full ruptures. The frequency of full ruptures is determined by the balance of normal stress and potential stress drop, both of which are a function of the bend angle.

Releasing bends have a different tendency. Unlike the restraining bends, the location of rupture arrest in the releasing bend is after passing the center of the linking segment. This can be understood as follows. While the center of the linking segment (bend) has a smaller potential stress drop due to misorientation from the regional stress field, a rupture does not stop here because of very small normal stress (10MPa). After passing the center of the bend, normal stress increases and the arrest criterion is satisfied.

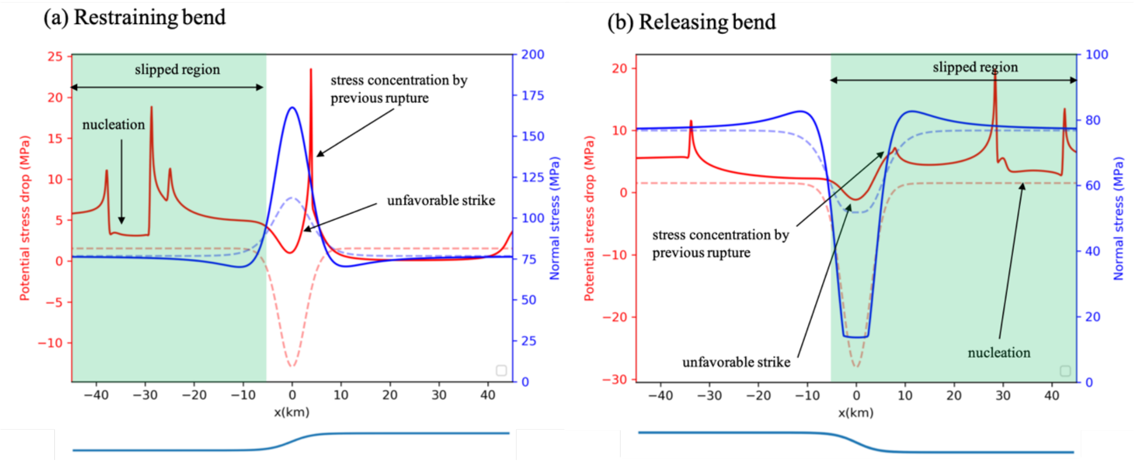

Figure 4.11. The potential stress drop and normal stress before a partial rupture for both bends. The dashed lines show the background potential stress drop and normal stress.

4.4.2. Is fracture energy proportional to normal stress in nature?

We assumed the standard rate-state friction with spatially uniform constitutive parameters. As a result, the fracture energy is roughly proportional to the local normal stress, and high normal stress directly leads to rupture termination via higher fracture energy. During rapid slip, the RSF law is no longer applicable because dynamic weakening is exerting (di Toro et al., 2011). Several mechanisms are proposed for dynamic weakening (e.g., Rice, 2006; Han et al. 2011; Hirose & Shimamoto, 2005), and the dependence of the normal stress on the fracture energy is different depending on the dominant mechanism.

Furthermore, in addition to the on-fault frictional heating, off-fault damage could also act as an energy sink during rupture propagation (e.g., Andrews, 2005). The extent of off-fault damage also varies along strike because it is sensitive to local stress field, which reflects the fault geometry. Dynamic rupture simulations on a rough fault with Drucker-Prager type viscoelasticity demonstrate the importance of the background stress field on the spatial pattern of plastic strain (Dunham et al., 2011b). Hence, it is likely that fracture energy is not simply proportional to the normal stresses in nature, and the simulation result is subject to changes if a more realistic off-fault medium and the dynamic weakening process are considered.

4.4.3. Comparison with a planar fault and nonuniform parameters

In contrast to our model, several sequence simulations explore the efficiency of rupture barriers using planar faults with spatially nonuniform parameters (Kaneko et al., 2010; Wei & Shi, 2021; Yang et al., 2012). Here we discuss the similarities and differences between these models and our nonplanar model.

From the stability analysis of the rate and state friction law, a velocity-strengthening fault is known to inhibit rupture nucleation and propagation. This is called the "stability barrier" (Scholz, 2019) and was explored in several earthquake sequence simulations. For example, Kaneko et al. (2010) placed a velocity-strengthening barrier between two velocity-weakening patches. By varying the width and $a - b$ value of the barrier, they were able to reproduce the full spectrum from no barrier to permanent barrier. This feature is similar to our bend barrier. Additionally, both models share the fact that some full ruptures nucleate at the barrier. However, the stability barrier accommodates the slip deficit by afterslip and interseismic creep, while there is a smaller or no slip deficit in our restraining bends.

Heterogeneous but constant normal stress distribution also causes barriers. Yang et al. (2012) modeled a subducted seamount as a high normal stress patch (instead of accounting for full elastic stress transfer on the nonplanar fault) and performed earthquake sequence simulations. They found that the normal stress patch acts as a conditional barrier if the normal stress at the patch is larger than a threshold but does not produce a permanent barrier as seen in our bend barrier and stability barrier. Although their study did not explore the whole possible parameter space, we speculate that a high normal stress patch does not act as a permanent barrier because the accumulated stress must be released eventually as a full rupture.

It should be noted that both Kaneko el al. (2010) and Yang et al. (2012) used uniform backslip loading (equation 2.20 in Chapter 2), which forces the long-term slip rate of the entire fault to be uniform. As their models target the megathrust earthquakes in subduction zones, this assumption may be reasonable. On the other hand, intraplate faults do not have spatially uniform long-term slip rates because plate motion is accommodated by multiple faults. Hence, models targeting intraplate faults should be able to reproduce the nonuniform spatial slip without assuming the spatial distribution of backslip values.

4.4.4. Long-term slip rates and off-fault deformation

The decrease of long-term slip on a restraining bend is consistent with several natural observations. As already mentioned, the geologic slip rate at the Altyn-Tagh fault decreases toward a restraining bend (Elliott et al., 2018). The San Andreas Fault (SAF) is another well-studied example. The geologic and geodetic slip rates in the southern big restraining bend of the SAF (the San Bernadino strand) are lower than the surrounding strands (the Mojave and Coachella segments) (Blisniuk et al., 2010; Cooke & Dair, 2011). The slip deficit in an unfavorable bend is thought to be accommodated by the activity of secondary faults or distributed deformation. In fact, significant off-fault shear deformation is also inferred from geodetic and topographic analyses (Dolan & Haravitch, 2014; Gray et al., 2018; Johnson, 2013).

For further discussion, we consider how large off-fault deformation due to the stress relaxation on the fault is expected in our simulations. The off-fault deformation field that results in the stress relaxation on the fault is not unique (i.e., different off-fault deformation patterns could reproduce the same stress relaxation on the fault). However, by assuming the off-fault deformation is localized near the fault trace, we can uniquely determine the equivalent slip and opening with the relaxed stresses. With this concept, we calculate the distribution of the imaginary slip $\Delta u^t_{1,\dots,N}$ and opening $\Delta u^n_{1,\dots,N}$ (negative values mean closing or compaction) that accommodate the relaxed shear stress $\Delta\tau_{1,\dots,N}$ and normal stress $\Delta\sigma_{1,\dots,N}$.

$$\begin{pmatrix} \Delta\tau_{1,\ldots,N} \\ \Delta\sigma_{1,\ldots,N} \end{pmatrix} = \begin{pmatrix} K_{\tau t} & K_{\tau n} \\ K_{\sigma t} & K_{\sigma n} \end{pmatrix} \begin{pmatrix} \Delta u^t_{1,\ldots,N} \\ \Delta u^n_{1,\ldots,N} \end{pmatrix}, \tag{4.11}$$

where K is the integral kernel for the boundary integral equation (Tada & Yamashita, 1997). By solving these $2N$ linear equations for Δu^t and Δu^n, we obtain the distribution of imaginary slip and opening.

Fig. 4.12 shows the result of the calculation. It seems that the equivalent off-fault slip compensates for the "slip deficit" (i.e., the sum of the on-fault slip and equivalent off-fault slip is spatially uniform). If an unfavorably oriented bend is present, the equivalent off-fault slip becomes large because of significant shear stress is relaxed during the interseismic period. The equivalent opening is zero in the case of planar fault as normal stress is constant. Closing and opening components are present in restraining and releasing bends, which suggest the occurrence of reverse-faulting and normal-faulting, respectively, in more realistic case of 3D configurations.

We note that Maxwell-type stress relaxation is not the unique way to avoid monotonic stress buildup due to the curvature term. If the stress relaxation is driven by aftershock activities (Chapter 3), logarithmic relaxation might be more reasonable, which is consistent with the Omori law. Further, instead of relaxing the stress in an element-wise manner, we could add a diffusional term of stresses to mimic stress redistributions by off-fault seismicity. Recently, Mallick et al. (2021) built an earthquake sequence simulation model on fold-thrust belts. They modeled the hanging wall deformation caused by the slip on a nonplanar thrust fault by placing additional boundary elements that are governed by the elastoplastic criterion. It is critically important to develop elaborate methods like Mallick et al. (2021) that account for the effect of off-fault deformation and to validate them with observables, such as moment tensor of off-fault earthquakes and geologic and geodetic slip rate of faults.

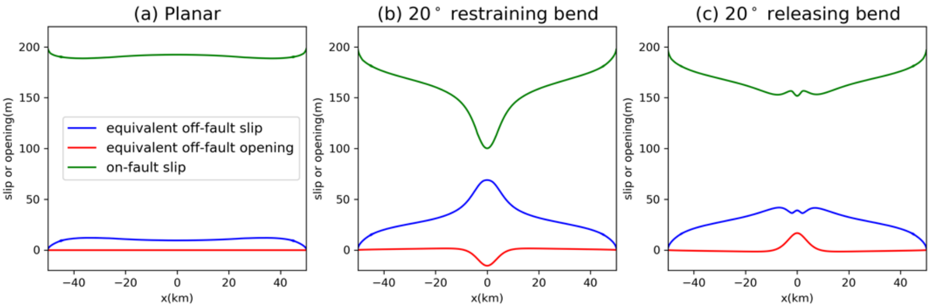

Figure 4.12. Calculated additional slip and opening that produce the relaxed stress. (a) Planar fault. (b) 20º restraining bend. (c) 20º releasing bend. Other parameters are $W = 5\,\text{km}$ and $t_{relax} = 1500\text{yrs}$.

4.4.5. Comments on other geometrical complexities

Fault stepovers (offset two parallel faults) are also known to arrest rupture propagations. Biasi & Wesnousky (2016) found that the likelihood of a rupture jumping past a stepover decreases with increasing the length of the stepover. Dynamic rupture simulations also confirm the existence of a critical offset length that hinders a rupture jumping one to another (Harris & Day, 1993), which makes a contrast to our bend result indicating the primary importance of the bend angle.

In mechanical models, stepovers are often distinguished from restraining/releasing bends in the sense that the two fault strands are not connected. However, the distinction of stepovers and (continuous) bends are based on the observation at the surface. It is suggested that two disconnected fault strands at the surface are often continuous at depth based on mechanical analysis of the coseismic slip distribution at the surface (Aochi, 2003; Oglesby, 2020) and seismic data (Giba et al., 2012). Also, extensional stepovers often contain several subsidiary faults. Therefore, the models of discontinuous stepover (e.g., Romanet et al., 2018) and continuous double-bend (this work) can be seen as the end members of the real world.

Fault branching is another nonplanar structure. Some earthquake ruptures (e.g., the 2002

Mw 7.9 Denali earthquake) propagate into a branching segment, not the main segment. Dynamic rupture simulations revealed how the branch angle, prestress, and rupture speed control the path selection of ruptures on a branching fault system (Kame et al., 2003). Natural fault bends often contain branching structures, for example, the 1992 Mw 7.3 Landers earthquake (Aochi & Fukuyama, 2002). Analog modeling of strike-slip restraining bends also produces branching structures (Cooke et al., 2013). Earthquake sequence simulations on branching faults will also be important future work.

Our model is the mode 2 configuration (map-view of strike-slip faults). In the mode 3 case that corresponds to dip-slip faults, the slip does not cause normal stress changes. This implies a more uniform normal stress (and fracture energy) over the fault, and a bend acts as a weaker barrier. In fact, Biasi & Wesnousky (2017) found that dip-slip earthquakes could propagate steeper bends than strike-slip earthquakes. The mode 3 case should also be explored in the future.

5. General Discussion

So far, I presented how earthquake sequence simulations with boundary element method and H-matrices can be used as a tool to address fundamental problems of the earthquake science (Chapter 2). In Chapter 3 and Chapter 4, I successfully explain several independent observations regarding aftershocks and rupture terminations using earthquake sequence simulations. Here, I discuss future perspectives on earthquake modeling building on this work.

5.1. Modeling multiscale earthquakes

Earthquakes are inherently multiscale phenomena as seen in the power-law event size distribution, but current numerical models have difficulty in dealing with multiscale problems. For example, numerical simulations targeting M_w~8 earthquakes cannot produce $M_w < 6$ earthquakes due to the use of finite mesh sizes. It is unclear how the neglect of smaller earthquakes below the model resolution biases the model output. High-performance simulation methods such as the lattice H-matrices (Chapter 2) will help us to extend the scale range of numerical simulations and answer this essential question. Rigorous models also help verify multiscale models enabled by essential assumptions, such as inherent discreteness (Richards-Dinger & Dieterich, 2012) and renormalization of the rupture process (Ide & Aochi, 2005).

5.2. The limitation of 2D models

In order to avoid high computational costs and to make a problem simpler, modeling studies generally favor 2D problems. However, on the modeling of nonplanar faults, 2D modeling has an inherent limitation. As discussed in Chapter 4, nonplanar strike-slip faults usually accompany dip-slip faulting in their neighborhood (transpressive or transtensional structures). This situation cannot be modeled in 2D. Furthermore, the 2D problem usually assumes infinite fault width, which is unrealistic because of the finite seismogenic width (less than 20km for vertical strike-slip faults). We should be aware that 2D modeling sometimes overlooks essential features that are present in the real world.

5.3. Toward realistic seismicity

The aftershock sequence simulations in Chapter 3 are not the whole earthquake cycle simulations but a single mainshock-aftershock sequence. On the other hand, the multicycle simulation in Chapter 4 does not produce a realistic aftershock sequence because it does not contain subsidiary faults. Important future work is to combine them. With a certain external loading to the fault system in Chapter 3, we could perform multicycle simulations of mainshocks, aftershocks, and foreshocks (if any) sequences. It would also be important to study the role of partial ruptures on the main fault on the aftershocks. In coupling Chapter 3 and Chapter 4, because the normal stress heterogeneity on the rough main fault monotonically accumulates over time, it will be required to add a stress relaxation method such as the one introduced in Chapter 4.

An ultimate goal of physics-based earthquake sequence simulations would be to explain the spatiotemporal characteristics of seismicity. The time series of seismicity is well explained by the epidemic type aftershock sequence (ETAS) model (Ogata, 1988). The ETAS model calculates the seismicity rate as the linear superposition of the Omori decay of all earthquakes that occurred in history. The success of the ETAS model places a constraint on physics-based earthquake models. Can physics-based earthquake sequence models replicate the ETAS model? Does multiscale interaction between faults yield the ETAS model? On the other hand, the ETAS model is still incomplete for very long time scales because it does not consider the slip budget on the fault. In other words, the ETAS model is a stochastic model, but the long-term slip budget gives somewhat deterministic description of seismicity. Physics-based simulations also has the potential to reconcile this discrepancy.

5.4. Evolving fault geometries

We presented earthquake sequence simulations up to 10,000 years in Chapter 4. We did not allow for the change of fault geometries, but fault geometries evolve over geologic time scales. How long is the assumption of the fixed fault geometry valid? It would be natural to consider that the fault geometry changes over a time scale that the fault experiences slip comparable to the characteristic scale of it ($d/\lambda\sim1$, where d is slip and λ is the characteristic scale of fault nonplanarity). Thus, this time scale is scale-dependent quantity. Smaller fault structure changes in s short period, while larger structures are persistent over a long time scale. This leads to the conclusion that we should not incorporate small-scale fault geometry in our model if we assume fixed fault geometry. However, the neglect of smaller scales could bias the result as numerical simulations suggest that the nucleation process of earthquakes depends on the minimum roughness length scale in the model (Ozawa et al., 2019).

Thus, one direction of next-generation earthquake sequence simulations is to consider the evolution of fault geometry as well as keep resolving each earthquake rupture. This requires an effort to model the creation of new fractures and their coalesces by some mechanical considerations. Some attempts account for fault growth during dynamic ruptures and earthquake sequences (Ando et al., 2004; Preuss et al., 2019), but current models only handle the extension of the fault tip. More general methods for the evolution of fault geometry will be necessary. Generally, fault grows toward simpler geometries by the accumulation of slip (Perrin, Manighetti, Ampuero, et al., 2016; Sagy et al., 2007; Wesnousky, 1988). However, the width of the fault damage zones has been suggested to increase linearly with fault length (Faulkner et al., 2011; Vermilye & Scholz, 1998). The growth process of faults is not yet fully understood, and physics-based approaches for this enigma is critically important.

6. General Conclusions

The purpose of this thesis was to advance our understanding of the earthquake generation process on nonplanar faults. We pursue this goal by quasi-dynamic earthquake sequence simulations. This thesis is divided into one part on the computational method and two parts on the application to earthquake science.

In Chapter 2, I developed a high-performance computational method for earthquake sequence simulations applicable to 3D nonplanar faults. We demonstrated that the use of the H-matrices significantly reduces the computational time of the matrix-vector multiplications. Furthermore, the use of lattice H-matrices improved the parallel scalability of the computational performance compared with the original H-matrices. The numerical experiments conducted in Oakforest-PACS demonstrated that the computational speed did not saturate up to 30,000 cores. We also showed the roughly $O(N\log N)$ complexity of both the memory size and execution time even when the fault is nonplanar.

In Chapter 3, I demonstrated that earthquake simulations on a geometrically complex fault zone can replicate realistic aftershock sequences both in space and time. I showed that the geometrical roughness of the mainshock fault trace is essential for the generation of fault-side aftershocks via stress heterogeneity entailed by the main fault slip. The features in our simulations are consistent with many observations, supporting the hypothesis that most aftershocks are off-fault events. Additionally, the model reproduces the Omori law and the migration of aftershock activities. To sum up, the spatiotemporal statistics of aftershocks can be explained by the heterogeneous stress field produced by the complexity of fault geometry, in combination with the time-dependent nucleation process by rate and state friction.

In Chapter 4, I performed long-term earthquake sequence simulations on a fault containing a restraining and releasing bend. I implemented a stress relaxation method to avoid monotonic buildup of normal stresses, which allows for steady earthquake cycles and performing statistical analyses. By varying several parameters, we showed that (1) the bend angle controls the passing possibility, (2) the bend angle dependence of passing possibility replicates the empirical law for continental strike-slip earthquakes, (3) the spatial heterogeneity of long-term slip rates on the fault.

Appendix A: The integration kernel for 2D plane strain problems

The discretized forms of the computational kernels used in Chapter 3 and Chapter 4 are given as follows (Ando et al., 2007; Segall, 2010). In the piecewise constant interpolation of slip, the kernel is the sum of the dislocations at both edges of each element; that is,

$$S_{ij} = s_{ij}^{+} - s_{ij}^{-},$$

$$N_{ij} = n_{ij}^{+} - n_{ij}^{-}.$$

By the definition of the coordinate transform of stress tensor ¥Sigma,

$$s_{ij}^{\pm} = \frac{G}{2\pi}\left[-\frac{1}{2}\left(\Sigma_{xx}^{\pm} - \Sigma_{yy}^{\pm}\right)\sin 2\theta + \cos 2\theta\right],$$

$$n_{ij}^{\pm} = \frac{G}{2\pi}\left[\frac{1}{2}\left(\Sigma_{xx}^{\pm} + \Sigma_{yy}^{\pm}\right) - \frac{1}{2}\left(\Sigma_{xx}^{\pm} - \Sigma_{yy}^{\pm}\right)\cos 2\theta - \Sigma_{xy}^{\pm}\sin 2\theta\right],$$

where θ is the angle between the tangential vectors at element i and j. The expressions of Σ are

$$\Sigma_{xx}^{\pm} = \frac{\left(y_i^c - y_j^{\pm}\right)\left[3\left(x_i^c - x_j^{\pm}\right)^2 + \left(y_i^c - y_j^{\pm}\right)^2\right]}{\left[\left(x_i^c - x_j^{\pm}\right)^2 + \left(y_i^c - y_j^{\pm}\right)^2\right]^2},$$

$$\Sigma_{yy}^{\pm} = \frac{\left(y_i^c - y_j^{\pm}\right)\left[\left(y_i^c - y_j^{\pm}\right)^2 - \left(x_i^c - x_j^{\pm}\right)^2\right]}{\left[\left(x_i^c - x_j^{\pm}\right)^2 + \left(y_i^c - y_j^{\pm}\right)^2\right]^2},$$

$$\Sigma_{xy}^{\pm} = \frac{\left(x_i^c - x_j^{\pm}\right)\left[\left(x_i^c - x_j^{\pm}\right)^2 - \left(y_i^c - y_j^{\pm}\right)^2\right]}{\left[\left(x_i^c - x_j^{\pm}\right)^2 + \left(y_i^c - y_j^{\pm}\right)^2\right]^2}.$$

where x_i^c, y_i^c are the coordinates of the center of element i and $x_j^{\pm}, y_j^{\pm}$ are the coordinates of the edges of element j.

Appendix B: Code verification with SEAS benchmark problems

Throughout this thesis, I used HBI (available at https://github.com/sozawa94/hbi) in performing earthquake sequence simulations. Since late 2020, I have participated in a SEAS project funded by Southern California Earthquake Center. Here, I demonstrate the accuracy of my code with the following two problems: BP3 (a 2D dip-slip fault) and BP5 (a 3D vertical strike-slip fault). The detailed information is found in https://strike.scec.org/cvws/seas/index.html. Fig. B.1 shows the result of BP3, and Fig. B.2 shows the result of BP5. Both results are in a good agreement between several modeling groups, including my HBI code (ozawa), which validate the accuracy of our simulations. The detailed comparison for BP5 is also found in Jiang et al. (2021).

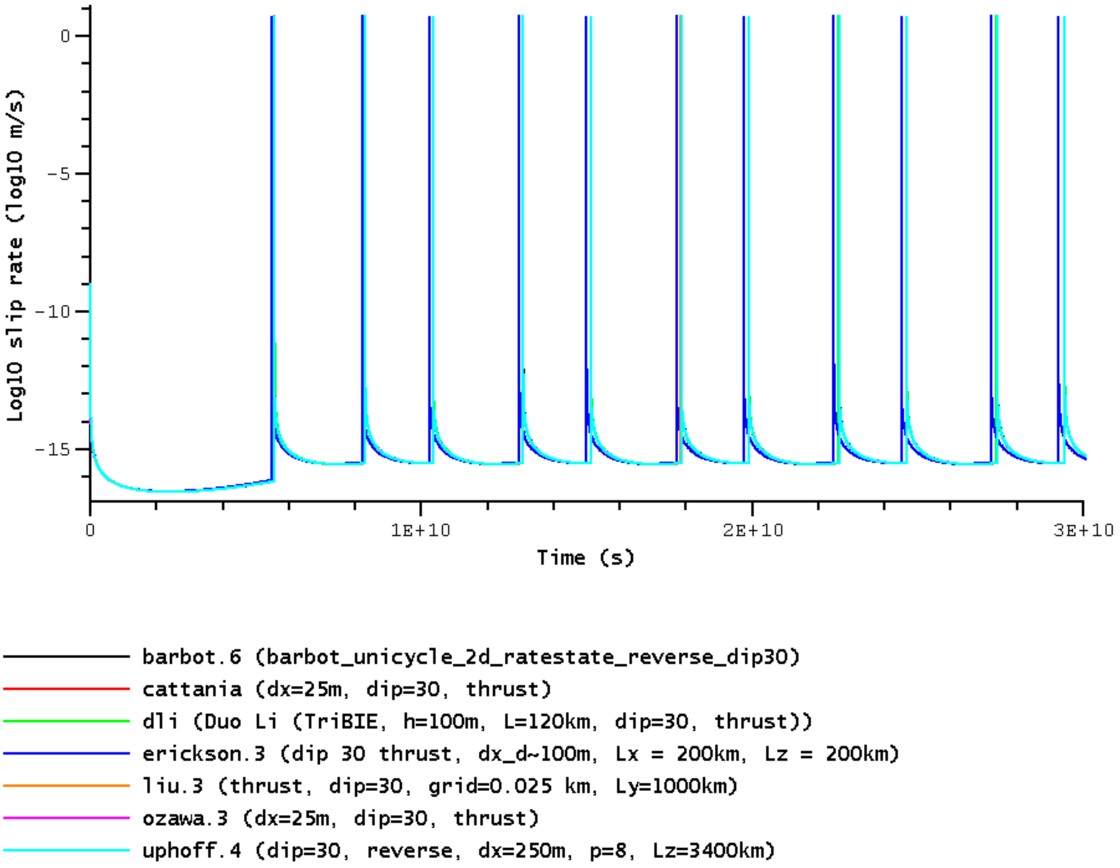

Figure B.1. The evolution of the slip rate on the free surface in BP3 problem with the dip=30º reverse fault. My result using HBI is shown in ozawa.3. All results show reasonable agreement. The figure is created in https://strike.scec.org/cvws/seas/index.html.

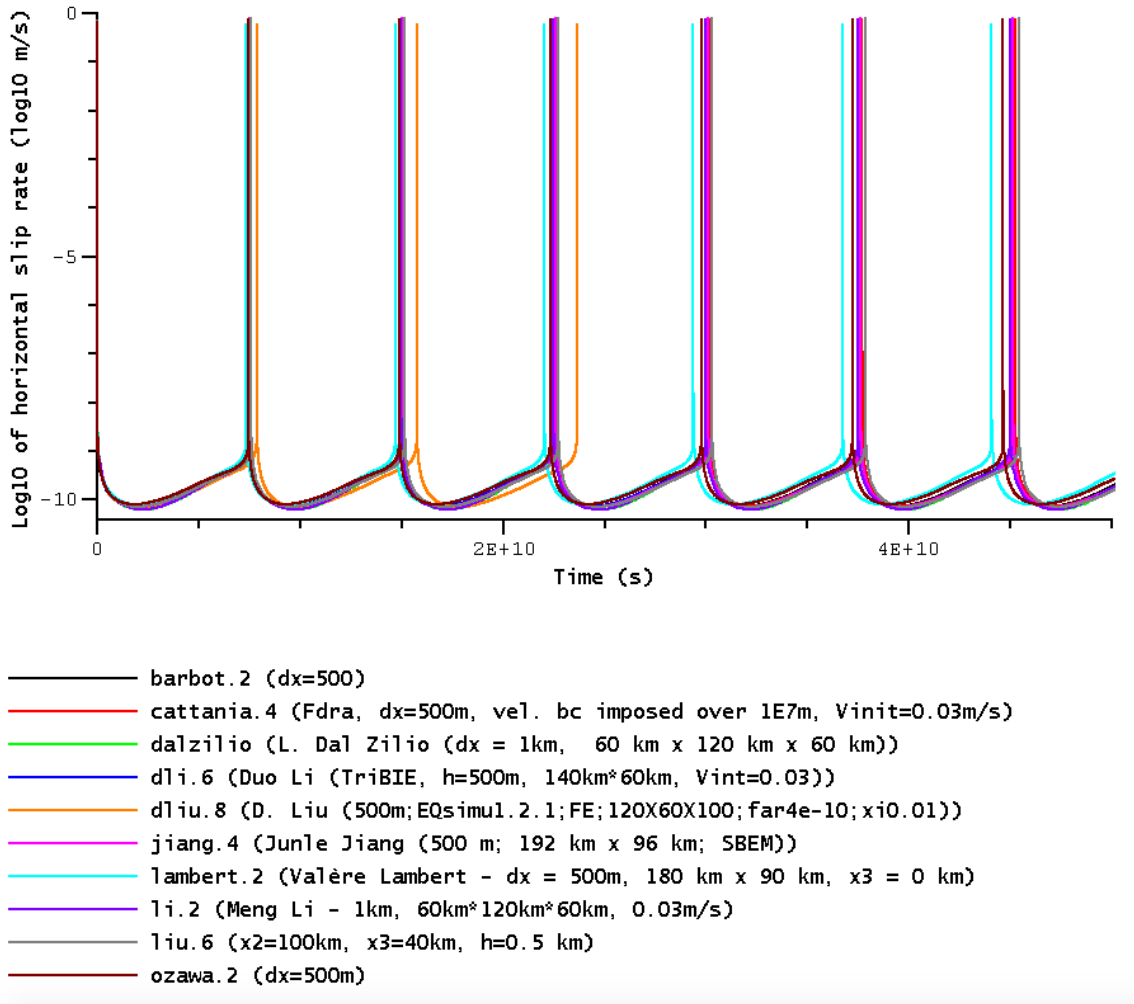

Figure B.2. The evolution of the slip rate on the free surface in BP5 problem. My result using HBI is shown in ozawa.2. All results show reasonable agreement. The figure is created in https://strike.scec.org/cvws/seas/index.html.

Appendix C: Analytical Approximation

C.1 Duration of power-law decay of aftershocks as a function of the initial condition

Here, we describe the analytical solution of the duration of the Omori aftershock sequence based on Dieterich (1992) and its extension by Heimisson & Segall (2018).

For a rate and state fault, time to instability in the case of no external loading is given by

$$t^* = \frac{a}{HV_{ini}}, \tag{C.1}$$

where

$$H = -\frac{G\eta}{\sigma l} + \frac{b}{d_c}, \tag{C.2}$$

with η and l being geometric factor and the length of fault, respectively. Following Heimisson & Segall (2018), for crack-like nucleation in an elastic medium, H can be approximated as

$$H = \frac{\left(b - \frac{\pi(b-a)^2}{b}\right)}{d_c}. \tag{C.3}$$

The aftershock duration can be estimated in the following manner. Heimisson & Segall (2018) showed that the time to instability (C.5) is valid when the healing term in the state evolution can be neglected (called well-above steady state).

With the definition of state variable as equation (3.2-3.3), this condition is expressed as

$$\frac{V_0}{V} e^{\frac{\mu_0 - \phi}{b}} \ll 1. \tag{C.4}$$

If the timescale of the coseismic stress change is short enough, the state variable after the mainshock is unchanged, that is, ϕ_{ini}. Thus, we expect that the minimum slip rate of subsidiary faults which are on the way to nucleation after the stress perturbation by the mainshock is given by

$$V \approx V_0\, e^{-\frac{\mu_0 - \phi_{ini}}{b}}. \tag{C.5}$$

Coupling equations (C.5) and (C.9), we obtain the duration of the Omori sequence as

$$t_{omori} = \frac{a}{HV_0} e^{-\frac{\mu_0 - \phi_{ini}}{b}}. \qquad (C.6)$$

Note that the duration of the Omori aftershock sequence is primarily dependent on the initial state variable ϕ_{ini}. That is, the duration does not directly depend on the stress, although whether individual faults produce aftershocks is determined by the stress condition.

C.2 Approximation of the aftershock migration

Next, we consider the migration process of aftershocks. For simplicity, we make the following assumptions: (1) receiver faults located on $y = 0$, (2) receiver faults are parallel to the x-axis, and (3) mainshock fault is planar ($\alpha = 0$). Fracture mechanics shows that the shear stress change near the tip of a crack is expressed as

$$\Delta\tau(x) = \frac{K}{\sqrt{2\pi x}} + O\left(x^{\frac{1}{2}}\right). \qquad (C.7)$$

where K is the stress intensity factor (Lawn, 1993) and x is measured from the crack tip. This stress gradient causes the gradient of time to instability and the resulting migration of aftershocks. Due to the direct effect, the slip rate immediately after the mainshock V_a is given by

$$V_a = V_{ini} \exp\left(\frac{\Delta\tau}{a\sigma}\right). \qquad (C.8)$$

where V_{ini} is the slip rate before the stress change $\Delta\tau$ and is assumed to be uniform. Combining equations (C.5) with neglecting $O(x^{\frac{1}{2}})$ term and (C.9-10), we obtain the locaiton of the aftershock front (AF)

$$x_{AF}(t) = \frac{K^2}{2\pi\, a^2\sigma^2}\left(\log\left(\frac{a}{HV_{ini}}\right) - \log t\right)^{-2}. \qquad (C.9)$$

Note that well above steady-state is assumed in deriving equation (C.6), so this does not hold for large t values because we have seen the absence of aftershocks for large t. In addition, the $O(x^{\frac{1}{2}})$ term in equation (C.11) becomes significant for large x.

Although the near-tip stress field given by equation (C.11) is valid for a planar crack, we believe that it approximately holds for a rough fault by modifying stress concentration factor K accounting for the rough geometry. As can be seen from equation (C.13), the migration distance of aftershock for a fixed time t scales with K^2. This implies that smaller stress concentration slows down the migration of aftershocks.

Appendix D: Convergence Tests

Here, we test the numerical convergence of the simulations shown in Chapter 2. We used four element sizes and the result is shown in Fig. D.1. Except the lowest resolution ($L_b/\Delta s = 1.8$), the curve of maximum slip rate evolution perfectly overlaps, although the overall behavior of the case of lowest resolution also agrees with others.

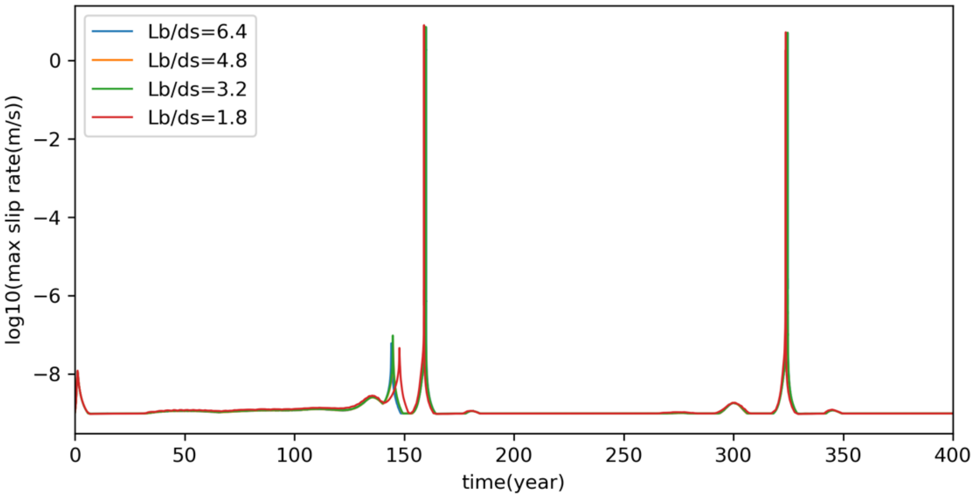

Figure D.1. The time evolution of maximum slip rate on the fault in the problem setting described in Section 2.2.4 using different element sizes (rectangular elements).

Similarly, we perform a convergence test for the model used in Chapter 3. We compare the results between the original (main fault: 0.01 km, subsidiary faults: 0.04 km) and refined mesh sizes in terms of the maximum slip rate on the fault system. The evolution of the maximum slip rate is shown in Fig. D.2. The two results are in good agreement. Although the exact timing of the aftershock shows some differences (Fig. D.2 inset), this will not change the result of our statistical analysis.

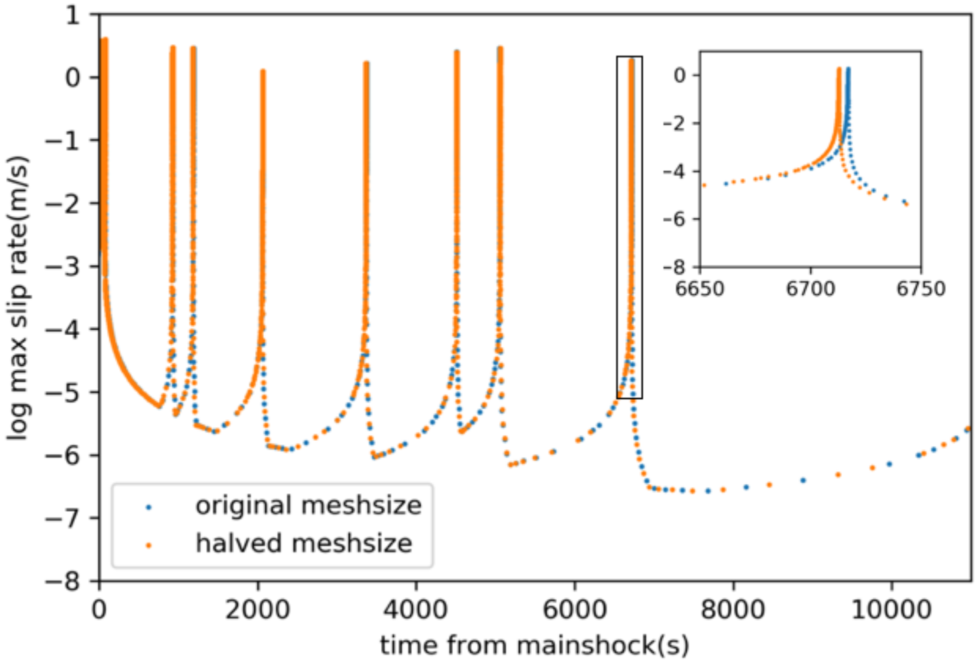

Figure D.2. Evolution of maximum slip rate for the original and refined meshsizes for the model used in Chapter 3.

Acknowledgements

I am grateful to my adviser Ryosuke Ando for giving me numerous scientific insights into earthquake science, invaluable opportunities, and maximum freedom. I have truly enjoyed working with him for these three years. He also obtained the computational resource in Oakforest-PACS that was necessary to accomplish this study. I also thank my former advisers. Takahiro Hatano was my adviser during my master's program and teach me important skills as a scientist. Nobuki Kame introduced me to the basics of earthquake sequence simulations using the boundary element method when I was in my fourth year of undergraduate. I also appreciate my coworkers; Eric M. Dunham, Pierre Romanet, Akihiro Ida, and Tetsuya Hoshino for giving me excellent advice. Insightful comments by the reviewers (Satoshi Ide, Nobuki Kame, Masao Nakatani, Naoyuki Kato, and Yoshihiro Kaneko) greatly improved this thesis.

My motivation for this study has been maintained by communications and discussions with people in the earthquake science community. I thank my wonderful colleagues in University of Tokyo. I especially want to thank Hanaya Okuda for giving me abundant knowledge about rock friction and Kansuke Uemura for stimulating discussion about earthquake physics. Also, I thank the participants of the workshops "Numerical Modeling of Earthquake Motions" in Slovakia and "Earthquakes (3rd edition), Nucleation , Triggering, and Relationship With Aseismic Processes" in France.

I was supported by Grant-in-Aid for JSPS Fellows [project number: 19J21676].

I thank all my friends for giving me a wonderful time. Finally, I thank my family who gave me the best environment where I can do what I like without any anxiety.

References

Abdelmeguid, M., Ma, X., & Elbanna, A. (2019). A Novel Hybrid Finite Element-Spectral Boundary Integral Scheme for Modeling Earthquake Cycles: Application to Rate and State Faults With Low-Velocity Zones. *Journal of Geophysical Research: Solid Earth*, *124*(12), 12854–12881. https://doi.org/10.1029/2019JB018036

Ader, T. J., Lapusta, N., Avouac, J. P., & Ampuero, J. P. (2014). Response of rate-and-state seismogenic faults to harmonic shear-stress perturbations. *Geophysical Journal International*, *198*(1), 385–413. https://doi.org/10.1093/gji/ggu144

Aharonov, E., & Scholz, C. H. (2018). A Physics-Based Rock Friction Constitutive Law: Steady State Friction. *Journal of Geophysical Research: Solid Earth*, *123*(2), 1591–1614. https://doi.org/10.1002/2016JB013829

Allam, A. A., Kroll, K. A., Milliner, C. W. D., & Richards-Dinger, K. B. (2019). Effects of Fault Roughness on Coseismic Slip and Earthquake Locations. *Journal of Geophysical Research: Solid Earth*, *124*(11), 11336–11349. https://doi.org/10.1029/2018JB016216

Allison, K. L., & Dunham, E. M. (2018). Earthquake cycle simulations with rate-and-state friction and power-law viscoelasticity. *Tectonophysics*, *733*, 232–256. https://doi.org/10.1016/j.tecto.2017.10.021

Ampuero, J.-P., & Ben-Zion, Y. (2008). Cracks, pulses and macroscopic asymmetry of dynamic rupture on a bimaterial interface with velocity-weakening friction. *Geophysical Journal International*, *173*(2), 674–692.

Ampuero, J.-P., & Rubin, A. M. (2008). Earthquake nucleation on rate and state faults – Aging and slip laws. *Journal of Geophysical Research*, *113*(B1), B01302. https://doi.org/10.1029/2007JB005082

Ando, R., Kame, N., & Yamashita, T. (2007). An efficient boundary integral equation method applicable to the analysis of non-planar fault dynamics. *Earth, Planets and Space*, *59*(5), 363–373. https://doi.org/10.1186/BF03352696

Ando, R., & Kaneko, Y. (2018). Dynamic rupture simulation reproduces spontaneous multifault rupture and arrest during the 2016 Mw 7.9 Kaikoura earthquake. *Geophysical Research Letters*, *45*(23).

Ando, R., Shaw, B. E., & Scholz, C. H. (2009). Quantifying natural fault geometry: Statistical of splay fault angles. *Bulletin of the Seismological Society of America*, *99*(1), 389–395. https://doi.org/10.1785/0120080942

Ando, R., Tada, T., & Yamashita, T. (2004). Dynamic evolution of a fault system through interactions between fault segments. *Journal of Geophysical Research: Solid Earth*, *109*(5), 1–15. https://doi.org/10.1029/2003JB002665

Ando, R., & Yamashita, T. (2007). Effects of mesoscopic-scale fault structure on dynamic earthquake ruptures: Dynamic formation of geometrical complexity of earthquake faults. *Journal of Geophysical Research: Solid Earth*, *112*(B9).

Andrews, D. J. (1976). Rupture propagation with finite stress in antiplane strain. *Journal of Geophysical Research*, *81*(20), 3575–3582.

Andrews, D. J. (2005). Rupture dynamics with energy loss outside the slip zone. *Journal of Geophysical Research B: Solid Earth*, *110*(1), 1–14. https://doi.org/10.1029/2004JB003191

Aochi, H. (2003). *The role of fault continuity at depth in numerical simulations of earthquake rupture*.

Aochi, H., & Fukuyama, E. (2002). Three-dimensional nonplanar simulation of the 1992 Landers earthquake. *Journal of Geophysical Research: Solid Earth*, *107*(B2), ESE--4.

Aochi, H., Fukuyama, E., & Matsu'ura, M. (2000). Spontaneous rupture propagation on a non-planar fault in 3-D elastic medium. *Pure and Applied Geophysics*, *157*(11–12), 2003–2027. https://doi.org/10.1007/978-3-0348-7695-7_11

Aochi, H., & Ide, S. (2009). Complexity in earthquake sequences controlled by multiscale heterogeneity in fault fracture energy. *Journal of Geophysical Research: Solid Earth*, *114*(B3).

Aslam, K. S., & Daub, E. G. (2018). Effect of Fault Roughness on Aftershock Distribution: Elastic Off-Fault Material Properties. *Journal of Geophysical Research: Solid Earth*, *123*(11), 9689–9711. https://doi.org/10.1029/2018JB016214

Aslam, K. S., & Daub, E. G. (2019). Effect of fault roughness on aftershock distribution: Plastic off-fault material properties. *Journal of Geophysical Research: Solid Earth*, *124*(7), 6989–7012.

Barall, M., & Tullis, T. E. (2016). The performance of triangular fault elements in Earthquake Simulators. *Seismological Research Letters*, *87*(1), 164–170. https://doi.org/10.1785/0220150163

Barbot, S. (2018). Asthenosphere Flow Modulated by Megathrust Earthquake Cycles.

Geophysical Research Letters, *45*(12), 6018–6031. https://doi.org/10.1029/2018GL078197

Barbot, S. (2019a). Modulation of fault strength during the seismic cycle by grain-size evolution around contact junctions. *Tectonophysics*, *765*, 129–145. https://doi.org/10.1016/j.tecto.2019.05.004

Barbot, S. (2019b). Slow-slip, slow earthquakes, period-two cycles, full and partial ruptures, and deterministic chaos in a single asperity fault. *Tectonophysics*, *768*. https://doi.org/10.1016/j.tecto.2019.228171

Bebendorf, M. (2000). Numerische Mathematik Approximation of boundary element matrices. *Numerische Mathematik*, *86*, 565–589.

Beeler, N. M., Tullis, T. E., & Goldsby, D. L. (2008). Constitutive relationships and physical basis of fault strength due to flash heating. *Journal of Geophysical Research: Solid Earth*, *113*(1), 1–12. https://doi.org/10.1029/2007JB004988

Behr, W. M., Gerya, T. v., Cannizzaro, C., & Blass, R. (2021). Transient Slow Slip Characteristics of Frictional-Viscous Subduction Megathrust Shear Zones. *AGU Advances*, *2*(3). https://doi.org/10.1029/2021AV000416

Ben-Zion, Y., & Rice, J. R. (1993). Earthquake failure sequences along a cellular fault zone in a three-dimensional elastic solid containing asperity and nonasperity regions. *Journal of Geophysical Research: Solid Earth*, *98*(B8), 14109–14131.

Ben-Zion, Y., & Sammis, C. G. (2003). Characterization of fault zones. *Pure and Applied Geophysics*, *160*(3–4), 677–715.

Beroza, G. C., & Zoback, M. D. (1993). Mechanism diversity of the Loma Prieta aftershocks and the mechanics of mainshock-aftershock interaction. *Science*, *259*(5092), 210–213.

Bhattacharya, P., Rubin, A. M., Bayart, E., Savage, H. M., & Marone, C. (2015). Critical evaluation of state evolution laws in rate and state friction: Fitting large velocity steps in simulated fault gouge with time-, slip-, and stress-dependent constitutive laws. *Journal of Geophysical Research: Solid Earth*, *120*(9), 6365–6385.

Bhattacharya, P., & Viesca, R. C. (2019). Fluid-induced aseismic fault slip outpaces pore-fluid migration. *Science*, *364*(6439), 464–468. https://doi.org/10.1126/science.aaw7354

Biasi, G. P., & Wesnousky, S. G. (2016). Steps and gaps in ground ruptures: Empirical bounds on rupture propagation. *Bulletin of the Seismological Society of America*, *106*(3), 1110–1124. https://doi.org/10.1785/0120150175

Biasi, G. P., & Wesnousky, S. G. (2017). Bends and ends of surface ruptures. *Bulletin of the Seismological Society of America*, *107*(6), 2543–2560. https://doi.org/10.1785/0120160292

Biasi, G. P., & Wesnousky, S. G. (2021). Rupture passing probabilities at fault bends and steps, with application to rupture length probabilities for earthquake early warning. *Bulletin of the Seismological Society of America*, *111*(4), 2235–2247. https://doi.org/10.1785/0120200370

Bistacchi, A., Griffith, W. A., Smith, S. A. F., di Toro, G., Jones, R., & Nielsen, S. (2011). Fault roughness at seismogenic depths from LIDAR and photogrammetric analysis. *Pure and Applied Geophysics*, *168*(12), 2345–2363.

Bizzarri, A., & Cocco, M. (2003). Slip-weakening behavior during the propagation of dynamic ruptures obeying rate- and state-dependent friction laws. *Journal of Geophysical Research*, *108*(B8). https://doi.org/10.1029/2002jb002198

Blanpied, M. L., Lockner, D. A., & Byerlee, J. D. (1995). Frictional slip of granite at hydrothermal conditions. *Journal of Geophysical Research: Solid Earth*, *100*(B7), 13045–13064. https://doi.org/10.1029/95jb00862

Blisniuk, K., Rockwell, T., Owen, L. A., Oskin, M., Lippincott, C., Caffee, M. W., & Dortch, J. (2010). Late Quaternary slip rate gradient defined using high-resolution topography and 10Be dating of offset landforms on the southern San Jacinto Fault zone, California. *Journal of Geophysical Research: Solid Earth*, *115*(8). https://doi.org/10.1029/2009JB006346

Bonnet, E., Bour, O., Odling, N. E., Davy, P., Main, I., Cowie, P., & Berkowitz, B. (2001). Scaling of fracture systems in geological media. *Reviews of Geophysics*, *39*(3), 347–383.

Bonnet, M. (1999). Boundary Integral Equation Methods for Solids and Fluids. *Meccanica*, *34*(4), 301–302. https://doi.org/10.1023/A:1004795120236

Borm, S., Grasedyck, L., & Hackbusch, W. (2006). Hierarchical Matrices. In *Hierarchical Matrices* (Lecture Note). Max-Plunk-Institut fur Mathematik.

Brace, W. F., & Byerlee, J. D. (1966). Stick-slip as a Mechanism for Earthquakes. *Nature*, *153*.

Brodsky, E. E., Gilchrist, J. J., Sagy, A., & Collettini, C. (2011). Faults smooth gradually as a function of slip. *Earth and Planetary Science Letters*, *302*(1–2), 185–193.

Brodsky, E. E., Kirkpatrick, J. D., & Candela, T. (2016). Constraints from fault roughness on the scale-dependent strength of rocks. *Geology*, *44*(1), 19–22. https://doi.org/10.1130/G37206.1

Brown, S. R., & Scholz, C. H. (1985). Broad bandwidth study of the topography of natural rock surfaces. *Journal of Geophysical Research: Solid Earth*, *90*(B14), 12575–12582.

Bruhat, L., Klinger, Y., Vallage, A., & Dunham, E. M. (2020). Influence of fault roughness on surface displacement: from numerical simulations to coseismic slip distributions. *Geophysical Journal International*, *220*(3), 1857–1877.

Candela, T., & Brodsky, E. E. (2016). The minimum scale of grooving on faults. *Geology*, *44*(8), 603–606.

Candela, T., Renard, F., Bouchon, M., Brouste, A., Marsan, D., Schmittbuhl, J., & Voisin, C. (2009). Characterization of fault roughness at various scales: Implications of three-dimensional high resolution topography measurements. *Pure and Applied Geophysics*, *166*(10–11), 1817–1851. https://doi.org/10.1007/s00024-009-0521-2

Candela, T., Renard, F., Klinger, Y., Mair, K., Schmittbuhl, J., & Brodsky, E. E. (2012). Roughness of fault surfaces over nine decades of length scales. *Journal of Geophysical Research: Solid Earth*, *117*(B8).

Cattania, C. (2019). Complex Earthquake Sequences On Simple Faults. *Geophysical Research Letters*, *46*(17–18), 10384–10393. https://doi.org/10.1029/2019GL083628

Cattania, C., Hainzl, S., Wang, L., Enescu, B., & Roth, F. (2015). Aftershock triggering by postseismic stresses: A study based on Coulomb rate-and-state models. *Journal of Geophysical Research: Solid Earth*, *120*(4), 2388–2407.

Cattania, C., & Segall, P. (2019). Crack Models of Repeating Earthquakes Predict Observed Moment-Recurrence Scaling. *Journal of Geophysical Research: Solid Earth*, *124*(1), 476–503. https://doi.org/10.1029/2018JB016056

Cattania, C., & Segall, P. (2021). Precursory Slow Slip and Foreshocks on Rough Faults. *Journal of Geophysical Research: Solid Earth*, *126*(4). https://doi.org/10.1029/2020JB020430

Chang, T.-W., & Ide, S. (2020). Toward comparable relative locations between the mainshock slip and aftershocks via empirical approaches. *Earth, Planets and Space*, *72*(1), 1–16.

Chen, J., Niemeijer, A. R., & Spiers, C. J. (2017). Microphysically Derived Expressions for Rate-and-State Friction Parameters, a , b , and D_c . *Journal of Geophysical Research: Solid Earth*. https://doi.org/10.1002/2017JB014226

Chester, F. M. (1994). Effects of temperature on friction: Constitutive equations and experiments with quartz gouge. *Journal of Geophysical Research: Solid Earth*, *99*(93), 7247–7261.

Chester, F. M., & Chester, J. S. (1998). Ultracataclasite structure and friction processes of the Punchbowl fault, San Andreas system, California. *Tectonophysics*, *295*(1–2), 199–221. https://doi.org/10.1016/S0040-1951(98)00121-8

Chester, F. M., & Higgs, N. G. (1992). Multimechanism friction constitutive model for ultrafine quartz gouge at hypocentral conditions. *Journal of Geophysical Research*, *97*(B2), 1859–1870. https://doi.org/10.1029/91JB02349

Chester, M., & Chester, J. S. (2000). Stress and deformation along wavy frictional faults. *Journal of Geophysical Research: Solid Earth*, *105*.

Cooke, M. L., & Dair, L. C. (2011). Simulating the recent evolution of the southern big bend of the San Andreas fault, Southern California. *Journal of Geophysical Research: Solid Earth*, *116*(4), 1–20. https://doi.org/10.1029/2010JB007835

Cooke, M. L., Schottenfeld, M. T., & Buchanan, S. W. (2013). Evolution of fault efficiency at restraining bends within wet kaolin analog experiments. *Journal of Structural Geology*, *51*, 180–192. https://doi.org/10.1016/j.jsg.2013.01.010

Cunningham, W. D., & Mann, P. (2007). Tectonics of strike-slip restraining and releasing bends. *Geological Society, London, Special Publications*, *290*(1), 1–12.

Dahlstrom, C. (1969). Balanced cross sections. *Canadian Journal of Earth Sciences*, *6*, 743–757.

Das, S., & Henry, C. (2003). Spatial relation between main earthquake slip and its aftershock distribution. *Reviews of Geophysics*, *41*(3).

den Hartog, S. A. M., Niemeijer, A. R., & Spiers, C. J. (2012). New constraints on megathrust slip stability under subduction zone P--T conditions. *Earth and Planetary Science Letters*, *353*, 240–252.

di Toro, G., Han, R., Hirose, T., de Paola, N., Nielsen, S., Mizoguchi, K., Ferri, F., Cocco, M., & Shimamoto, T. (2011). Fault lubrication during earthquakes. *Nature*, *471*(7339), 494.

Dieterich, J. H. (1972). Time-dependent friction in rocks. *Journal of Geophysical Research*, *77*(20), 3690–3697.

Dieterich, J. H. (1978). Time-dependent friction and the mechanics of stick-slip. In *Rock Friction and Earthquake Prediction* (pp. 790–806). Springer.

Dieterich, J. H. (1979). Modeling of rock friction 1. Experimental results and constitutive equations. *Journal of Geophysical Research: Solid Earth*, *84*(B5), 2161–2168. https://doi.org/10.1029/JB084iB05p02161

Dieterich, J. H. (1992). Earthquake nucleation on faults with rate-and state-dependent strength. *Tectonophysics*, *211*(1–4), 115–134.

Dieterich, J. H. (1994). A constitutive law for rate of earthquake its application to earthquake clustering production. *Journal of Geophysical Research: Solid Earth*, *99*(B2), 2601–2618. https://doi.org/10.1029/93JB02581

Dieterich, J. H., & Smith, D. E. (2009). Nonplanar faults: Mechanics of slip and off-fault damage. *Pure and Applied Geophysics*, *166*, 1799–1815.

Dolan, J. F., & Haravitch, B. D. (2014). How well do surface slip measurements track slip at depth in large strike-slip earthquakes? The importance of fault structural maturity in controlling on-fault slip versus off-fault surface deformation. *Earth and Planetary Science Letters*, *388*, 38–47. https://doi.org/10.1016/j.epsl.2013.11.043

Duan, B., & Oglesby, D. D. (2005). Multicycle dynamics of nonplanar strike-slip faults. *Journal of Geophysical Research: Solid Earth*, *110*(3), 1–16. https://doi.org/10.1029/2004JB003298

Duan, B., & Oglesby, D. D. (2006). Heterogeneous fault stresses from previous earthquakes and the effect on dynamics of parallel strike-slip faults. *Journal of Geophysical Research: Solid Earth*, *111*(B5).

Dublanchet, P., Bernard, P., & Favreau, P. (2013). Interactions and triggering in a 3-D rate-and-state asperity model. *Journal of Geophysical Research: Solid Earth*, *118*(5), 2225–2245.

Duman, T. Y., Emre, O., Dogan, A., & Ozalp, S. (2005). Step-over and bend structures along the 1999 Duzce earthquake surface rupture, North Anatolian Fault, Turkey. *Bulletin of the Seismological Society of America*, *95*(4), 1250–1262. https://doi.org/10.1785/0120040082

Dunham, E. M., Belanger, D., Cong, L., & Kozdon, J. E. (2011a). Earthquake ruptures with strongly rate-weakening friction and off-fault plasticity, Part 1: Planar faults. *Bulletin of the Seismological Society of America*, *101*(5), 2296–2307.

Dunham, E. M., Belanger, D., Cong, L., & Kozdon, J. E. (2011b). Earthquake ruptures with strongly rate-weakening friction and off-fault plasticity, Part 2: Nonplanar faults. *Bulletin of the Seismological Society of America*, *101*(5), 2308–2322.

Duru, K., Allison, K. L., Rivet, M., & Dunham, E. M. (2019). Dynamic rupture and earthquake sequence simulations using the wave equation in second-order form. *Geophysical Journal International*, *219*(2), 796–815. https://doi.org/10.1093/gji/ggz319

Elliott, A. J., Oskin, M. E., Liu-Zeng, J., & Shao, Y. (2015). Rupture termination at restraining bends: The last great earthquake on the Altyn Tagh Fault. *Geophysical Research Letters*, *42*(7), 2164–2170. https://doi.org/10.1002/2015GL063107

Elliott, A. J., Oskin, M. E., Liu-zeng, J., & Shao, Y. X. (2018). Persistent rupture terminations at a restraining bend from slip rates on the eastern Altyn Tagh fault. *Tectonophysics*, *733*, 57–72. https://doi.org/10.1016/j.tecto.2018.01.004

Enescu, B., Mori, J., Miyazawa, M., & Kano, Y. (2009). Omori-Utsu law c-values associated with recent moderate earthquakes in Japan. *Bulletin of the Seismological Society of America*, *99*(2A), 884–891.

Erickson, B. A., & Day, S. M. (2016). Bimaterial effects in an earthquake cycle model using rate-and-state friction. *Journal of Geophysical Research: Solid Earth*, *121*(4), 2480–2506. https://doi.org/10.1002/2015JB012470

Erickson, B. A., & Dunham, E. M. (2014). An efficient numerical method for earthquake cycles in heterogeneous media: Alternating subbasin and surface-rupturing events on faults crossing a sedimentary basin. *Journal of Geophysical Research: Solid Earth*, *119*(4), 3290–3316.

Erickson, B. A., Dunham, E. M., & Khosravifar, A. (2017). A finite difference method for off-fault plasticity throughout the earthquake cycle. *Journal of the Mechanics and Physics of Solids*, *109*, 50–77. https://doi.org/10.1016/j.jmps.2017.08.002

Erickson, B. A., Jiang, J., Barall, M., Lapusta, N., Dunham, E. M., Harris, R., Abrahams, L. S., Allison, K. L., Ampuero, J.-P., Barbot, S., & others. (2020). The community code verification exercise for simulating sequences of earthquakes and aseismic slip (seas). *Seismological Research Letters*, *91*(2A), 874–890.

Fang, Z., & Dunham, E. M. (2013). Additional shear resistance from fault roughness and stress levels on geometrically complex faults. *Journal of Geophysical Research: Solid Earth*, *118*(7), 3642–3654. https://doi.org/10.1002/jgrb.50262

Faulkner, D. R., Jackson, C. A. L., Lunn, R. J., Schlische, R. W., Shipton, Z. K., Wibberley,

C. A. J., & Withjack, M. O. (2010). A review of recent developments concerning the structure, mechanics and fluid flow properties of fault zones. *Journal of Structural Geology*, *32*(11), 1557–1575. https://doi.org/10.1016/j.jsg.2010.06.009

Faulkner, D. R., Lewis, A. C., & Rutter, E. H. (2003). On the internal structure and mechanics of large strike-slip fault zones: field observations of the Carboneras fault in southeastern Spain. *Tectonophysics*, *367*(3–4), 235–251.

Faulkner, D. R., Mitchell, T. M., Jensen, E., & Cembrano, J. (2011). Scaling of fault damage zones with displacement and the implications for fault growth processes. *Journal of Geophysical Research: Solid Earth*, *116*(5), 1–11. https://doi.org/10.1029/2010JB007788

Felzer, K. R., & Brodsky, E. E. (2006). Decay of aftershock density with distance indicates triggering by dynamic stress. *Nature*, *441*(7094), 735–738.

Fujiwara, S., Yarai, H., Kobayashi, T., Morishita, Y., Nakano, T., Miyahara, B., Nakai, H., Miura, Y., Ueshiba, H., Kakiage, Y., & Une, H. (2016). Small-displacement linear surface ruptures of the 2016 Kumamoto earthquake sequence detected by ALOS-2 SAR interferometry 4. Seismology 2016 Kumamoto earthquake sequence and its impact on earthquake science and hazard assessment. *Earth, Planets and Space*, *68*(1). https://doi.org/10.1186/s40623-016-0534-x

Fukuyama, E. (2015). Dynamic faulting on a conjugate fault system detected by near-fault tilt measurements. *Earth, Planets and Space*, *67*(1), 1–10.

Fukuyama, E., Ellsworth, W. L., Waldhauser, F., & Kubo, A. (2003). Detailed fault structure of the 2000 western Tottori, Japan, earthquake sequence. *Bulletin of the Seismological Society of America*, *93*(4), 1468–1478.

Galvez, P., Somerville, P., Petukhin, A., Ampuero, J. P., & Peter, D. (2020). Earthquake Cycle Modelling of Multi-segmented Faults: Dynamic Rupture and Ground Motion Simulation of the 1992 M w 7.3 Landers Earthquake. *Pure and Applied Geophysics*, *177*(5), 2163–2179. https://doi.org/10.1007/s00024-019-02228-x

Geubelle, P. H., & Rice, J. R. (1995). A spectral method for three-dimensional elastodynamic fracture problems. *Journal of the Mechanics and Physics of Solids*, *43*(11), 1791–1824. https://doi.org/10.1016/0022-5096(95)00043-I

Giba, M., Walsh, J. J., & Nicol, A. (2012). Segmentation and growth of an obliquely reactivated normal fault. *Journal of Structural Geology*, *39*, 253–267. https://doi.org/10.1016/j.jsg.2012.01.004

Goebel, T. H. W., Kwiatek, G., Becker, T. W., Brodsky, E. E., & Dresen, G. (2017). What allows seismic events to grow big?: Insights from b-value and fault roughness analysis in laboratory stick-slip experiments. *Geology*, *45*(9), 815–818.

Grant Ludwig, L. (2015). Paleoseismology. *Treatise on Geophysics: Second Edition*, *4*, 559–579. https://doi.org/10.1016/B978-0-444-53802-4.00088-9

Gray, H. J., Shobe, C. M., Hobley, D. E. J., Tucker, G. E., Duvall, A. R., Harbert, S. A., & Owen, L. A. (2018). Off-fault deformation rate along the southern San Andreas fault at Mecca Hills, southern California, inferred from landscape modeling of curved drainages. *Geology*, *46*(1), 59–62. https://doi.org/10.1130/G39820.1

Griffith, W. A., Nielsen, S., di Toro, G., & Smith, S. A. F. (2010). Rough faults, distributed weakening, and off-fault deformation. *Journal of Geophysical Research: Solid Earth*, *115*(8), 1–22. https://doi.org/10.1029/2009JB006925

HACApK. Retrieved October 22, 2021, from https://github.com/Post-Peta-Crest/ppOpenHPC/tree/MATH/HACApK

Hackbusch, W. (1999). A Sparse Matrix Arithmetic Based on H-Matrices. Part I: Introduction to H-Matrices. *Computing*, *62*(2), 89–108.

Hainzl, S., Zöller, G., & Wang, R. (2010). Impact of the receiver fault distribution on aftershock activity. *Journal of Geophysical Research: Solid Earth*, *115*(5). https://doi.org/10.1029/2008JB006224

Hamling, I. J., Hreinsdóttir, S., Clark, K., Elliott, J., Liang, C., Fielding, E., Litchfield, N., Villamor, P., Wallace, L., Wright, T. J., D'Anastasio, E., Bannister, S., Burbidge, D., Denys, P., Gentle, P., Howarth, J., Mueller, C., Palmer, N., Pearson, C., … Stirling, M. (2017). Complex multifault rupture during the 2016 Mw 7.8 Kaikōura earthquake, New Zealand. *Science*, *356*(6334). https://doi.org/10.1126/science.aam7194

Han, R., Hirose, T., Shimamoto, T., Lee, Y., & Ando, J. I. (2011). Granular nanoparticles lubricate faults during seismic slip. *Geology*, *39*(6), 599–602. https://doi.org/10.1130/G31842.1

Hardebeck, J. L., & Okada, T. (2018). Temporal stress changes caused by earthquakes: a review. *Journal of Geophysical Research: Solid Earth*, *123*(2), 1350–1365.

Harding, T. P. (1985). Seismic Characteristics and Identification of Negative Flower Structures, Positive Flower Structures, and Positive Structural Inversion. *American Association of Petroleum Geologists Bulletin*, *69*(4), 582–600.

https://doi.org/10.1306/ad462538-16f7-11d7-8645000102c1865d

Harris, R. A. (2017). Large earthquakes and creeping faults. *Reviews of Geophysics*, *55*(1), 169–198.

Harris, R. A., & Day, S. M. (1993). Dynamics of fault interaction: parallel strike-slip faults. *Journal of Geophysical Research*, *98*(B3), 4461–4472. https://doi.org/10.1029/92JB02272

Harris, R. A., & Day, S. M. (1999). Dynamic 3D simulations of earthquakes on en echelon faults. *Geophysical Research Letters*, *26*(14), 2089–2092. https://doi.org/10.1029/1999GL900377

Harris, R. A., Dolan, J. F., Hartleb, R., & Day, S. M. (2002). The 1999 I ˙ zmit, Turkey, Earthquake: A 3D Dynamic Stress Transfer Model of Intraearthquake Triggering. *Bulletin of the Seismological Society of America*, *92*, 245–255. http://pubs.geoscienceworld.org/ssa/bssa/article-pdf/92/1/245/2717075/245_921_00825.245_255.pdf?casa_token=8mug_HWHiL4AAAAA:nqlXpIP5GGHmy7NRPFGQP8RBpIENRBFbuyXudE058n_ldCzLsrR4oxZ

Heimisson, E. R. (2020). Crack to pulse transition and magnitude statistics during earthquake cycles on a self-similar rough fault. *Earth and Planetary Science Letters*, *537*, 116202.

Heimisson, E. R., & Avouac, J. P. (2020). Analytical Prediction of Seismicity Rate Due to Tides and Other Oscillating Stresses. *Geophysical Research Letters*, *47*(23), 1–12. https://doi.org/10.1029/2020GL090827

Heimisson, E. R. (2019). Constitutive law for earthquake production based on rate-and-state friction: Theory and application of interacting sources. *Journal of Geophysical Research: Solid Earth*, *124*(2), 1802–1821. https://doi.org/10.1029/2018JB016823

Heimisson, E. R., & Segall, P. (2018). Constitutive law for earthquake production based on rate-and-state friction: Dieterich 1994 revisited. *Journal of Geophysical Research: Solid Earth*, *123*(5), 4141–4156.

Helmstetter, A., & Shaw, B. E. (2006). Relation between stress heterogeneity and aftershock rate in the rate-and-state model. *Journal of Geophysical Research: Solid Earth*, *111*(B7), B07304. https://doi.org/10.1029/2005JB004077

Helmstetter, A., & Sornette, D. (2002). Diffusion of epicenters of earthquake aftershocks, Omori's law, and generalized continuous-time random walk models. *Physical*

Review E, *66*(6), 61104.

Herrendörfer, R., Gerya, T., & van Dinther, Y. (2018). An Invariant Rate- and State-Dependent Friction Formulation for Viscoeastoplastic Earthquake Cycle Simulations. *Journal of Geophysical Research: Solid Earth*, *123*(6), 5018–5051. https://doi.org/10.1029/2017JB015225

Heslot, F., Baumberger, T., Perrin, B., Caroli, B., & Caroli, C. (1994). Creep, stick-slip, and dry-friction dynamics: Experiments and a heuristic model. *Physical Review E*, *49*(6), 4973.

Hillers, G., Ben-Zion, Y., & Mai, P. M. (2006). Seismicity on a fault controlled by rate- and state-dependent friction with spatial variations of the critical slip distance. *Journal of Geophysical Research: Solid Earth*, *111*(1), 1–23. https://doi.org/10.1029/2005JB003859

Hirose, T., & Shimamoto, T. (2005). Growth of molten zone as a mechanism of slip weakening of simulated faults in gabbro during frictional melting. *Journal of Geophysical Research: Solid Earth*, *110*(5), 1–18. https://doi.org/10.1029/2004JB003207

Hisakawa, T., Ando, R., Yano, T. E., & Matsubara, M. (2020). Dynamic rupture simulation of 2018, Hokkaido Eastern Iburi earthquake: role of non-planar geometry. *Earth, Planets and Space*, *72*(1), 1–14.

Hori, T., Kato, N., Hirahara, K., Baba, T., & Kaneda, Y. (2004). A numerical simulation of earthquake cycles along the Nankai Trough in southwest Japan: Lateral variation in frictional property due to the slab geometry controls the nucleation position. *Earth and Planetary Science Letters*, *228*(3–4), 215–226. https://doi.org/10.1016/j.epsl.2004.09.033

Hori, T., & Miyazaki, S. (2011). A possible mechanism of M 9 earthquake generation cycles in the area of repeating M 7~8 earthquakes surrounded by aseismic sliding. *Earth, Planets and Space*, *63*(7), 773–777. https://doi.org/10.5047/eps.2011.06.022

Howarth, J. D., Barth, N. C., Fitzsimons, S. J., Richards-Dinger, K., Clark, K. J., Biasi, G. P., Cochran, U. A., Langridge, R. M., Berryman, K. R., & Sutherland, R. (2021). Spatiotemporal clustering of great earthquakes on a transform fault controlled by geometry. *Nature Geoscience*, *14*(5), 314–320. https://doi.org/10.1038/s41561-021-00721-4

Huang, L., & Liu, C. Y. (2017). Three Types of Flower Structures in a Divergent-Wrench

Fault Zone. *Journal of Geophysical Research: Solid Earth*, *122*(12), 10,478-10,497. https://doi.org/10.1002/2017JB014675

Hyodo, M., Hori, T., & Kaneda, Y. (2016). A possible scenario for earlier occurrence of the next Nankai earthquake due to triggering by an earthquake at Hyuga-nada, off southwest Japan 4. Seismology. *Earth, Planets and Space*, *68*(1). https://doi.org/10.1186/s40623-016-0384-6

Ida, A. (2018). Lattice h-matrices on distributed-memory systems. *Proceedings - 2018 IEEE 32nd International Parallel and Distributed Processing Symposium, IPDPS 2018*, 389–398. https://doi.org/10.1109/IPDPS.2018.00049

Ida, A., Ataka, T., & Furuya, A. (2020). Lattice H-Matrices for Massively Parallel Micromagnetic Simulations of Current-Induced Domain Wall Motion. *IEEE Transactions on Magnetics*, *56*(4), 18–21. https://doi.org/10.1109/TMAG.2019.2959349

Ida, A., Iwashita, T., Mifune, T., & Takahashi, Y. (2014). Parallel hierarchical matrices with adaptive cross approximation on symmetric multiprocessing clusters. *Joirnal of Information Processing*, *22*, 642–650.

Ida, A., Iwashita, T., Ohtani, M., & Hirahara, K. (2015). Improvement of hierarchical matrices with adaptive cross approximation for large-scale simulation. *Journal of Information Processing*, *23*(3), 366–372.

Ida, A., Nakashima, H., & Kawai, M. (2018). Parallel hierarchical matrices with block low-rank representation on distributed memory computer systems. *ACM International Conference Proceeding Series*, 232–240. https://doi.org/10.1145/3149457.3149477

Ide, S., & Aochi, H. (2005). Earthquakes as multiscale dynamic ruptures with heterogeneous fracture surface energy. *Journal of Geophysical Research: Solid Earth*, *110*(11), 1–10. https://doi.org/10.1029/2004JB003591

Idini, B., & Ampuero, J. P. (2020). Fault-Zone Damage Promotes Pulse-Like Rupture and Back-Propagating Fronts via Quasi-Static Effects. *Geophysical Research Letters*, *47*(23), 1–12. https://doi.org/10.1029/2020GL090736

Jiang, J., Erickson, B. A., Lambert, V. R., Ampuero, J., Ando, R., Barbot, S. D., Cattania, C., Zilio, L. D., Duan, B., Dunham, E. M., & Gabriel, A. (2021). Community-Driven Code Comparisons for Three-Dimensional Dynamic Modeling of Sequences of Earthquakes and Aseismic Slip (SEAS). *Essoar Preprint*, 1–55.

Jiang, J., & Lapusta, N. (2016). Deeper penetration of large earthquakes on seismically quiescent faults. *Science*, *352*(6291), 1293–1297. https://doi.org/10.1126/science.aaf1496

Jin, Z., & Fialko, Y. (2021). Coseismic and Early Postseismic Deformation Due to the 2021 M7.4 Maduo (China) Earthquake. *Geophysical Research Letters*, *48*(21), 1–10. https://doi.org/10.1029/2021gl095213

Johnson, K. M. (2013). Slip rates and off-fault deformation in Southern California inferred from GPS data and models. *Journal of Geophysical Research: Solid Earth*, *118*(10), 5643–5664. https://doi.org/10.1002/jgrb.50365

Kame, N., Rice, J. R., & Dmowska, R. (2003). Effects of prestress state and rupture velocity on dynamic fault branching. *Journal of Geophysical Research: Solid Earth*, *108*(B5), 1–21. https://doi.org/10.1029/2002jb002189

Kaneko, Y., & Ampuero, J. P. (2011). A mechanism for preseismic steady rupture fronts observed in laboratory experiments. *Geophysical Research Letters*, *38*(21), 1–7. https://doi.org/10.1029/2011GL049953

Kaneko, Y., Ampuero, J. P., & Lapusta, N. (2011). Spectral-element simulations of long-term fault slip: Effect of low-rigidity layers on earthquake-cycle dynamics. *Journal of Geophysical Research: Solid Earth*, *116*(10), 1–18. https://doi.org/10.1029/2011JB008395

Kaneko, Y., Avouac, J. P., & Lapusta, N. (2010). Towards inferring earthquake patterns from geodetic observations of interseismic coupling. *Nature Geoscience*, *3*(5), 363–369. https://doi.org/10.1038/ngeo843

Kaneko, Y., & Fialko, Y. (2011). Shallow slip deficit due to large strike-slip earthquakes in dynamic rupture simulations with elasto-plastic off-fault response. *Geophysical Journal International*, *186*(3), 1389–1403. https://doi.org/10.1111/j.1365-246X.2011.05117.x

Kaneko, Y., & Lapusta, N. (2008). Variability of earthquake nucleation in continuum models of rate-and-state faults and implications for aftershock rates. *Journal of Geophysical Research: Solid Earth*, *113*(B12).

Kase, Y., & Day, S. M. (2006). Spontaneous rupture processes on a bending fault. *Geophysical Research Letters*, *33*(10), 2–5. https://doi.org/10.1029/2006GL025870

Kato, A., Fukuda, J., Nakagawa, S., & Obara, K. (2016). Foreshock migration preceding the 2016 Mw 7.0 Kumamoto earthquake, Japan. *Geophysical Research Letters*, *43*(17), 8945–8953.

Kato, A., Sakai, S., Matsumoto, S., & Iio, Y. (2021). Conjugate faulting and structural complexity on the young fault system associated with the 2000 Tottori earthquake. *Communications Earth & Environment*, *2*(1), 1–9. https://doi.org/10.1038/s43247-020-00086-3

Kato, N. (2003). Repeating slip events at a circular asperity: Numerical simulation with a rate- and state- dependent friction law. *Bull. Earthq. Res. Inst.*, *78*, 151–166.

Kato, N. (2007). Expansion of aftershock areas caused by propagating post-seismic sliding. *Geophysical Journal International*, *168*(2), 797–808.

Kato, N. (2016). Earthquake cycles in a model of interacting fault patches: Complex behavior at transition from seismic to aseismic slip. *Bulletin of the Seismological Society of America*, *106*(4), 1772–1787. https://doi.org/10.1785/0120150185

Kato, N., & Tullis, E. (2001). A composite rate- and state-dependent law for rock friction. *Geophysical Research Letters*, *28*(6), 1103–1106.

Kim, Y. S., Peacock, D. C. P., & Sanderson, D. J. (2004). Fault damage zones. *Journal of Structural Geology*, *26*(3), 503–517. https://doi.org/10.1016/j.jsg.2003.08.002

King, G. C. P., Stein, R. S., & Lin, J. (1994). Static stress changes and the triggering of earthquakes. *Bulletin of the Seismological Society of America*, *84*(3), 935–953.

King, G., & Nábělek, J. (1985). Role of fault bends in the initiation and termination of earthquake rupture. *Science*, *228*(4702), 984–987. https://doi.org/10.1126/science.228.4702.984

Klinger, Y. (2010). Relation between continental strike-slip earthquake segmentation and thickness of the crust. *Journal of Geophysical Research: Solid Earth*, *115*(7), 1–19. https://doi.org/10.1029/2009JB006550

Kodaira, S., Takahashi, N., Nakanishi, A., Miura, S., & Kaneda, Y. (2000). Subducted seamount imaged in the rupture zone of the 1946 Nankaido earthquake. *Science*, *289*(5476), 104–106. https://doi.org/10.1126/science.289.5476.104

Koper, K. D., Pankow, K. L., Pechmann, J. C., Hale, J. M., Burlacu, R., Yeck, W. L., Benz, H. M., Herrmann, R. B., Trugman, D. T., & Shearer, P. M. (2018). Afterslip Enhanced Aftershock Activity During the 2017 Earthquake Sequence Near Sulphur Peak, Idaho. *Geophysical Research Letters*, *45*(11), 5352–5361. https://doi.org/10.1029/2018GL078196

Lachenbruch, A. H. (1980). Frictional heating, fluid pressure, and the resistance to fault motion. *Journal of Geophysical Research: Solid Earth*, *85*(B11), 6097–6112. https://doi.org/10.1029/JB085iB11p06097

Lambert, V., & Barbot, S. (2016). Contribution of viscoelastic flow in earthquake cycles within the lithosphere-asthenosphere system. *Geophysical Research Letters*, *43*(19), 10,142-10,154. https://doi.org/10.1002/2016GL070345

Lambert, V., Lapusta, N., & Perry, S. (2021). Propagation of large earthquakes as self-healing pulses or mild cracks. *Nature*, *591*(7849), 252–258. https://doi.org/10.1038/s41586-021-03248-1

Lapusta, N., & Liu, Y. (2009). Three-dimensional boundary integral modeling of spontaneous earthquake sequences and aseismic slip. *Journal of Geophysical Research: Solid Earth*, *114*(9). https://doi.org/10.1029/2008JB005934

Lapusta, N., Rice, J. R., Ben-Zion, Y., & Zheng, G. (2000). Elastodynamic analysis for slow tectonic loading with spontaneous rupture episodes on faults with rate- and state-dependent friction. *Journal of Geophysical Research: Solid Earth*, *105*(B10), 23765–23789. https://doi.org/10.1029/2000JB900250

Lawn, B. (1993). *Fracture of brittle solids*. Cambridge university press.

Leeman, J. R., Saffer, D. M., Scuderi, M. M., & Marone, C. (2016). Laboratory observations of slow earthquakes and the spectrum of tectonic fault slip modes. *Nature Communications*, *7*, 11104.

Lengliné, O., Enescu, B., Peng, Z., & Shiomi, K. (2012). Decay and expansion of the early aftershock activity following the 2011, Mw9. 0 Tohoku earthquake. *Geophysical Research Letters*, *39*(18).

Li, D., & Liu, Y. (2021). Cascadia megathrust earthquake rupture model constrained by geodetic fault locking. *Philosophical Transactions of the Royal Society A: Mathematical, Physical and Engineering Sciences*, *379*(2196). https://doi.org/10.1098/rsta.2020.0135

Lieou, C. K. C., Daub, E. G., Guyer, R. A., Ecke, R. E., Marone, C., & Johnson, P. A. (2017). Simulating stick-slip failure in a sheared granular layer using a physics-based constitutive model. *Journal of Geophysical Research: Solid Earth*, *122*(1), 295–307. https://doi.org/10.1002/2016JB013627

Liu, D., Duan, B., & Luo, B. (2020). EQsimu: A 3-D finite element dynamic earthquake simulator for multicycle dynamics of geometrically complex faults governed by rate- And state-dependent friction. *Geophysical Journal International*, *220*(1), 598–

609. https://doi.org/10.1093/GJI/GGZ475

Liu, D., Duan, B., Prush, V. B., Oskin, M. E., & Liu-Zeng, J. (2021). Observation-constrained multicycle dynamic models of the Pingding Shan earthquake gate along the Altyn Tagh Fault. *Tectonophysics*, *814*, 228948. https://doi.org/10.1016/j.tecto.2021.228948

Liu, Y., & Rice, J. R. (2007). Spontaneous and triggered aseismic deformation transients in a subduction fault model. *Journal of Geophysical Research*, *112*(B9), B09404. https://doi.org/10.1029/2007JB004930

Lozos, J. C., Oglesby, D. D., Duan, B., & Wesnousky, S. G. (2011). The effects of double fault bends on rupture propagation: A geometrical parameter study. *Bulletin of the Seismological Society of America*, *101*(1), 385–398. https://doi.org/10.1785/0120100029

Mallick, R., Bürgmann, R., Johnson, K., & Hubbard, J. (2021). A unified framework for earthquake sequences and the growth of geological structure in fold-thrust belts. *Journal of Geophysical Research: Solid Earth*, 1–26. https://doi.org/10.1029/2021jb022045

Manighetti, I., Campillo, M., Bouley, S., & Cotton, F. (2007). Earthquake scaling, fault segmentation, and structural maturity. *Earth and Planetary Science Letters*, *253*(3–4), 429–438. https://doi.org/10.1016/j.epsl.2006.11.004

Manighetti, I., Caulet, C., de Barros, L., Perrin, C., Cappa, F., & Gaudemer, Y. (2015). Generic along-strike segmentation of A far normal faults, E ast A frica: Implications on fault growth and stress heterogeneity on seismogenic fault planes. *Geochemistry, Geophysics, Geosystems*, *16*(2), 443–467.

Mann, P. (2007). Global catalogue, classification and tectonic origins of restraining- and releasing bends on active and ancient strike-slip fault systems. *Geological Society Special Publication*, *290*, 13–142. https://doi.org/10.1144/SP290.2

Marone, C. (1998). Laboratory-derived friction laws and their application to seismic faulting. *Annual Review of Earth and Planetary Sciences*, *26*(1), 643–696.

Marone, C. J., Scholz, C. H., & Bilham, R. (1991). On the mechanics of earthquake afterslip. *Journal of Geophysical Research: Solid Earth*, *96*(B5), 8441–8452.

Marsan, D. (2005). The role of small earthquakes in redistributing crustal elastic stress. *Geophysical Journal International*, *163*(1), 141–151.

Marsan, D. (2006). Can coseismic stress variability suppress seismicity shadows?

Insights from a rate-and-state friction model. *Journal of Geophysical Research: Solid Earth*, *111*(6). https://doi.org/10.1029/2005JB004060

Masson, D., Rossi, M., Carmona, C., Adragna, F., Peltzer, G., Felgl, K., & Rabautet, T. (1993). The displacement field of the Landers earthquake Mapped By Radar Interferometry. *Nature*, *364*(July), 138–142.

Milliner, C. W. D., Dolan, J. F., Hollingsworth, J., Leprince, S., Ayoub, F., & Charles G. Sammis. (2015). Quantifying near-field and off-fault deformation patterns of the 1992 Mw 7.3 Landers earthquake Christopher. *Geochemistry Geophysics Geosystems*, *18*(1–2), 1541–1576. https://doi.org/10.1002/2014GC005693.Received

Miyake, Y., & Noda, H. (2019). Fully dynamic earthquake sequence simulation of a fault in a viscoelastic medium using a spectral boundary integral equation method: does interseismic stress relaxation promote aseismic transients? *Earth, Planets and Space*, *71*(1). https://doi.org/10.1186/s40623-019-1113-8

Moore, G. F., Bangs, N. L., Taira, A., Kuramoto, S., Pangborn, E., & Tobin, H. J. (2007). Three-dimensional splay fault geometry and implications for tsunami generation. *Science*, *318*(5853), 1128–1131. https://doi.org/10.1126/science.1147195

Nagata, K., Nakatani, M., & Yoshida, S. (2012). A revised rate-and state-dependent friction law obtained by constraining constitutive and evolution laws separately with laboratory data. *Journal of Geophysical Research: Solid Earth*, *117*(B2).

Nakatani, M. (2001). Conceptual and physical clarification of rate and state friction: Frictional sliding as a thermally activated rheology. *Journal of Geophysical Research: Solid Earth*, *106*(B7), 13347–13380. https://doi.org/10.1029/2000JB900453

Nielsen, S. B., & Knopoff, L. (1998). The equivalent strength of geometrical barriers to earthquakes. *Journal of Geophysical Research: Solid Earth*, *103*(5), 9953–9965. https://doi.org/10.1029/97jb03293

Nikkhoo, M., & Walter, T. R. (2015). Triangular dislocation: An analytical, artefact-free solution. *Geophysical Journal International*, *201*(2), 1119–1141. https://doi.org/10.1093/gji/ggv035

Noda, H., & Lapusta, N. (2013). Stable creeping fault segments can become destructive as a result of dynamic weakening. *Nature*, *493*(7433), 518–521. https://doi.org/10.1038/nature11703

Ogata, Y. (1988). Statistical models for earthquake occurrences and residual analysis for point processes. *Journal of the American Statistical Association*, *83*(401), 9–27. https://doi.org/10.1080/01621459.1988.10478560

Oglesby, D. D. (2020). What can surface-slip distributions tell us about fault connectivity at depth? *Bulletin of the Seismological Society of America*, *110*(3), 1025–1036. https://doi.org/10.1785/0120190245

Oglesby, D. D., Archuleta, R. J., & Nielsen, S. B. (2000). The three-dimensional dynamics of dipping faults. *Bulletin of the Seismological Society of America*, *90*(3), 616–628. https://doi.org/10.1785/0119990113

Ohtani, M., Hirahara, K., Hori, T., & Hyodo, M. (2014). Observed change in plate coupling close to the rupture initiation area before the occurrence of the 2011 Tohoku earthquake: Implications from an earthquake cycle model. *Geophysical Research Letters*, *41*(6), 1899–1906. https://doi.org/10.1002/2013GL058751

Ohtani, M., Hirahara, K., Takahashi, Y., Hori, T., Hyodo, M., Nakashima, H., & Iwashita, T. (2011). Fast computation of quasi-dynamic earthquake cycle simulation with Hierarchical Matrices. *Procedia Computer Science*, *4*, 1456–1465.

Okada, Y. (1992). Internal dislocations due to shear and tensile faults in a half-space. *Bulletin of the Seismological Society of America*, *82*(2), 1018–1040. http://pubs.geoscienceworld.org/ssa/bssa/article-pdf/82/2/1018/2707430/BSSA0820021018.pdf

Okubo, K., Bhat, H. S., Rougier, E., Marty, S., Schubnel, A., Lei, Z., Knight, E. E., & Klinger, Y. (2019). Dynamics, radiation and overall energy budget of earthquake rupture with coseismic off-fault damage. *Journal of Geophysical Research: Solid Earth*, *124*, 11771–11801.

Okubo, P. G., & Aki, K. (1987). Fractal geometry in the San Andreas fault system (USA). *Journal of Geophysical Research*, *92*(B1), 345–355. https://doi.org/10.1029/JB092iB01p00345

Okuwaki, R., Hirano, S., Yagi, Y., & Shimizu, K. (2020). Inchworm-like source evolution through a geometrically complex fault fueled persistent supershear rupture during the 2018 Palu Indonesia earthquake. *Earth and Planetary Science Letters*, *547*, 116449. https://doi.org/10.1016/j.epsl.2020.116449

Omori, F. (1894). On the after-shocks of earthquakes. *Coll. Sci. Imp. Univ. Tokyo*, *7*.

Ong, S. Q. M., Barbot, S., & Hubbard, J. (2019). Physics-Based Scenario of Earthquake

Cycles on the Ventura Thrust System, California: The Effect of Variable Friction and Fault Geometry. *Pure and Applied Geophysics*, *176*(9), 3993–4007. https://doi.org/10.1007/s00024-019-02111-9

Oskin, M. E., Arrowsmith, J. R., Corona, A. H., Elliott, A. J., Fletcher, J. M., Fielding, E. J., Gold, P. O., Garcia, J. J. G., Hudnut, K. W., Liu-Zeng, J., & Teran, O. J. (2012). Near-field deformation from the El Mayor-Cucapah earthquake revealed by differential LIDAR. *Science*, *335*(6069), 702–705. https://doi.org/10.1126/science.1213778

Otsuki, K., & Dilov, T. (2005). Evolution of hierarchical self-similar geometry of experimental fault zones: Implications for seismic nucleation and earthquake size. *Journal of Geophysical Research: Solid Earth*, *110*(3), 1–9. https://doi.org/10.1029/2004JB003359

Ozawa, S. W., Hatano, T., & Kame, N. (2019). Longer migration and spontaneous decay of aseismic slip pulse caused by fault roughness. *Geophysical Research Letters*, *46*.

Peng, Z., & Zhao, P. (2009). Migration of early aftershocks following the 2004 Parkfield earthquake. *Nature Geoscience*, *2*(12), 877–881.

Perfettini, H., & Avouac, J.-P. (2004). Postseismic relaxation driven by brittle creep: A possible mechanism to reconcile geodetic measurements and the decay rate of aftershocks, application to the Chi-Chi earthquake, Taiwan. *Journal of Geophysical Research: Solid Earth*, *109*(B2).

Perfettini, H., Frank, W. B., Marsan, D., & Bouchon, M. (2018). A model of aftershock migration driven by afterslip. *Geophysical Research Letters*, *45*(5), 2283–2293.

Perfettini, H., & Molinari, A. (2017). A micromechanical model of rate and state friction: 1. Static and dynamic sliding. *Journal of Geophysical Research: Solid Earth*, *122*(4), 2590–2637. https://doi.org/10.1002/2016JB013302

Perrin, C., Manighetti, I., Ampuero, J.-P., Cappa, F., & Gaudemer, Y. (2016). Location of largest earthquake slip and fast rupture controlled by along-strike change in fault structural maturity due to fault growth. *Journal of Geophysical Research: Solid Earth*, *121*(5), 3666–3685.

Perrin, C., Manighetti, I., & Gaudemer, Y. (2016). Off-fault tip splay networks: A genetic and generic property of faults indicative of their long-term propagation. *Comptes Rendus Geoscience*, *348*(1), 52–60.

Poliakov, A. N. B., Dmowska, R., & Rice, J. R. (2002). Dynamic shear rupture interactions with fault bends and off-axis secondary faulting. *Journal of Geophysical Research: Solid Earth*, *107*(B11), ESE--6. https://doi.org/10.1029/2001jb000572

Power, W. L., & Tullis, T. E. (1991). Euclidean and fractal models for the description of rock surface roughness. *Journal of Geophysical Research: Solid Earth*, *96*(B1), 415–424.

Power, W. L., Tullis, T. E., Brown, S. R., Boitnott, G. N., & Scholz, C. H. (1987). Roughness of natural fault surfaces. *Geophysical Research Letters*, *14*(1), 29–32.

Press, W. H., Teukolsky, S. A., Vetterling, W. T., & Flannery, B. P. (2007). *Numerical recipes 3rd edition: The art of scientific computing*. Cambridge university press.

Preuss, S., Herrendörfer, R., Gerya, T., Ampuero, J. P., & van Dinther, Y. (2019). Seismic and Aseismic Fault Growth Lead to Different Fault Orientations. *Journal of Geophysical Research: Solid Earth*, *124*(8), 8867–8889. https://doi.org/10.1029/2019JB017324

Qiu, Q., Hill, E. M., Barbot, S., Hubbard, J., Feng, W., Lindsey, E. O., Feng, L., Dai, K., Samsonov, S. v., & Tapponnier, P. (2016). The mechanism of partial rupture of a locked megathrust: The role of fault morphology. *Geology*, *44*(10), 875–878. https://doi.org/10.1130/G38178.1

Renard, F., Candela, T., & Bouchaud, E. (2013). Constant dimensionality of fault roughness from the scale of micro-fractures to the scale of continents. *Geophysical Research Letters*, *40*(1), 83–87.

Rice, J. R. (1993). Spatio-temporal complexity of slip on a fault. *Journal of Geophysical Research*, *98*(B6), 9885. https://doi.org/10.1029/93JB00191

Rice, J. R. (2006). Heating and weakening of faults during earthquake slip. *Journal of Geophysical Research: Solid Earth*, *111*(B5), n/a-n/a. https://doi.org/10.1029/2005JB004006

Rice, J. R., Lapusta, N., & Ranjith, K. (2001). Rate and state dependent friction and the stability of sliding between elastically deformable solids. *Journal of the Mechanics and Physics of Solids*, *49*(9), 1865–1898.

Rice, J. R., & Ruina, A. L. (1983). Stability of steady frictional slipping. *Journal of Applied Mechanics*, *50*(2), 343–349.

Rice, J. R., Sammis, C. G., & Parsons, R. (2005). Off-fault secondary failure induced by a dynamic slip pulse. *Bulletin of the Seismological Society of America*, *95*(1), 109–134.

Richards-Dinger, K., & Dieterich, J. H. (2012). RSQSim earthquake simulator. *Seismological Research Letters*, *83*(6), 983–990.

Romanet, P. (2017). *Fast algorithms to model quasi-dynamic earthquake cycles in complex fault networks (PhD thesis)*.

Romanet, P., Bhat, H. S., Jolivet, R., & Madariaga, R. (2018). Fast and Slow Slip Events Emerge Due to Fault Geometrical Complexity. *Geophysical Research Letters*, *45*(10), 4809–4819. https://doi.org/10.1029/2018GL077579

Romanet, P., & Ozawa, S. (2021). Fully Dynamic Earthquake Cycle Simulations on a Nonplanar Fault Using the Spectral Boundary Integral Element Method (sBIEM). *Bulletin of the Seismological Society of America*. https://doi.org/10.1785/0120210178

Romanet, P., Sato, D. S. K., & Ando, R. (2020). Curvature, a mechanical link between the geometrical complexities of a fault: Application to bends, kinks and rough faults. *Geophysical Journal International*, *223*(1), 211–232. https://doi.org/10.1093/gji/ggaa308

Ross, Z. E., Cochran, E. S., Trugman, D. T., & Smith, J. D. (2019). 3D fault architecture controls the dynamism of earthquake swarms. *Science*. http://science.sciencemag.org/

Ross, Z. E., Idini, B., Jia, Z., Stephenson, O. L., Zhong, M., Wang, X., Zhan, Z., Simons, M., Fielding, E. J., Yun, S.-H., & others. (2019). Hierarchical interlocked orthogonal faulting in the 2019 Ridgecrest earthquake sequence. *Science*, *366*(6463), 346–351.

Rubin, A. M., & Ampuero, J. P. (2005). Earthquake nucleation on (aging) rate and state faults. *Journal of Geophysical Research: Solid Earth*, *110*(11), 1–24. https://doi.org/10.1029/2005JB003686

Ruina, A. (1983a). Slip instability and state variable friction laws. *Journal of Geophysical Research*, *88*(B12), 10359–10370. https://doi.org/10.1029/JB088iB12p10359

Sagy, A., Brodsky, E. E., & Axen, G. J. (2007). Evolution of fault-surface roughness with slip. *Geology*, *35*(3), 283–286. https://doi.org/10.1130/G23235A.1

Sagy, A., & Lyakhovsky, V. (2019b). Stress patterns and failure around rough interlocked fault surface. *Journal of Geophysical Research: Solid Earth*, *124*(7), 7138–7154.

Sathiakumar, S., Barbot, S., & Hubbard, J. (2020). Earthquake Cycles in Fault-Bend Folds. *Journal of Geophysical Research: Solid Earth*, *125*(8). https://doi.org/10.1029/2019JB018557

Sato, D. S., & Ando, R. (2021). A log-linear time algorithm for the elastodynamic boundary integral equation method. *Engineering Analysis with Boundary Elements*, *133*, 407–450. https://doi.org/10.1016/j.enganabound.2021.08.026

Sato, H., Hirata, N., Koketsu, K., Okaya, D., Abe, S., Kobayashi, R., Matsubara, M., Iwasaki, T., Ito, T., Ikawa, T., Kawanaka, T., Kasahara, K., & Harder, S. (2005). Geology: Earthquake source fault beneath Tokyo. *Science*, *309*(5733), 462–464. https://doi.org/10.1126/science.1110489

Savage, H. M., & Brodsky, E. E. (2011). Collateral damage: Evolution with displacement of fracture distribution and secondary fault strands in fault damage zones. *Journal of Geophysical Research: Solid Earth*, *116*(B3).

Schaff, D. P., Beroza, G. C., & Shaw, B. E. (1998). Postseismic response of repeating aftershocks. *Geophysical Research Letters*, *25*(24), 4549–4552.

Scholz, C. H. (1998). Earthquakes and friction laws. *Nature*, *391*(6662), 37–42. https://doi.org/10.1038/34097

Scholz, C. H. (2019). *The mechanics of earthquakes and faulting*. Cambridge university press.

Scholz, C. H., Ando, R., & Shaw, B. E. (2010). The mechanics of first order splay faulting: The strike-slip case. *Journal of Structural Geology*, *32*(1), 118–126. https://doi.org/10.1016/j.jsg.2009.10.007

Scholz, C. H., Dawers, N. H., Yu, J.-Z., Anders, M. H., & Cowie, P. A. (1993). Fault growth and fault scaling laws: preliminary results. *Journal of Geophysical Research: Solid Earth*, *98*(B12), 21951–21961.

Scott, C., Champenois, J., Klinger, Y., Nissen, E., Maruyama, T., Chiba, T., & Arrowsmith, R. (2019). The 2016 M7 Kumamoto, Japan, Earthquake Slip Field Derived From a Joint Inversion of Differential Lidar Topography, Optical Correlation, and InSAR Surface Displacements. *Geophysical Research Letters*, *46*(12), 6341–6351. https://doi.org/10.1029/2019GL082202

Segall, P. (2010). Earthquake and volcano deformation. In *Earthquake and Volcano Deformation*. Princeton University Press. https://doi.org/10.5860/choice.48-0287

Segall, P., & Pollard, D. D. (1980). Mechanics of discontinuous faults. *Journal of Geophysical Research: Solid Earth*, *85*(B8), 4337–4350.

Shaw, B. E., Richards-Dinger, K., & Dieterich, J. H. (2015). Deterministic model of earthquake clustering shows reduced stress drops for nearby aftershocks.

Geophysical Research Letters, *42*(21), 9231–9238.

Shen, Z.-K., Sun, J., Zhang, P., Wan, Y., Wang, M., Bürgmann, R., Zeng, Y., Gan, W., Liao, H., & Wang, Q. (2009). Slip maxima at fault junctions and rupturing of barriers during the 2008 Wenchuan earthquake. *Nature Geoscience*, *2*(10), 718–724.

Shi, Q., Barbot, S., Wei, S., Tapponnier, P., Matsuzawa, T., & Shibazaki, B. (2020). Structural control and system-level behavior of the seismic cycle at the Nankai Trough. *Earth, Planets and Space*, *72*(1). https://doi.org/10.1186/s40623-020-1145-0

Shi, Z., & Day, S. M. (2013). Rupture dynamics and ground motion from 3-D rough-fault simulations. *Journal of Geophysical Research: Solid Earth*, *118*(3), 1122–1141.

Shipton, Z. K., & Cowie, P. A. (2001). Damage zone and slip-surface evolution over \$μ\$m to km scales in high-porosity Navajo sandstone, Utah. *Journal of Structural Geology*, *23*(12), 1825–1844.

Sibson, R. H. (1983). Continental fault structure and the shallow earthquake source. *Journal of the Geological Society*, *140*(5), 741–767. https://doi.org/10.1144/gsjgs.140.5.0741

Sieh, K. E., & Jahns, R. H. (1984). Holocene Activity of the San Andreas Fault At Wallace Creek, California. *Bulletin of the Geological Society of America*, *95*(8), 883–896.

Smith, D. E., & Dieterich, J. H. (2010). Aftershock sequences modeled with 3-D stress heterogeneity and rate-state seismicity equations: Implications for crustal stress estimation. *Pure and Applied Geophysics*, *167*, 1067–1085.

Tada, T., & Yamashita, T. (1997). Non-hypersingular boundary integral equations for two-dimensional non-planar crack analysis. *Geophysical Journal International*, *130*(2), 269–282.

Tajima, F., & Kanamori, H. (1985). Global survey of aftershock area expansion patterns. *Physics of the Earth and Planetary Interiors*, *40*(2), 77–134.

Tal, Y., Goebel, T., & Avouac, J. P. (2020). Experimental and modeling study of the effect of fault roughness on dynamic frictional sliding. *Earth and Planetary Science Letters*, *536*, 116133. https://doi.org/10.1016/j.epsl.2020.116133

Tal, Y., & Hager, B. H. (2018a). Dynamic mortar finite element method for modeling of shear rupture on frictional rough surfaces. *Computational Mechanics*, *61*(6), 699–716.

Tal, Y., & Hager, B. H. (2018b). The Slip Behavior and Source Parameters for

Spontaneous Slip Events on Rough Faults Subjected to Slow Tectonic Loading. *Journal of Geophysical Research: Solid Earth*, *123*(2), 1810–1823. https://doi.org/10.1002/2017JB014737

Tal, Y., Hager, B. H., & Ampuero, J. P. (2018). The Effects of Fault Roughness on the Earthquake Nucleation Process. *Journal of Geophysical Research: Solid Earth*, *123*(1), 437–456. https://doi.org/10.1002/2017JB014746

Tal, Y., Rubino, V., Rosakis, A. J., & Lapusta, N. (2020). lluminating the physics of dynamic friction throughlaboratory earthquakes on thrust faults. *PNAS*, *117*(35), 21095–21100. https://doi.org/10.1073/pnas.2004590117/-/DCSupplemental

Tchalenko, J. S. (1970). Similarities between shear zones of different magnitudes. *Geological Society of America Bulletin*, *81*(June), 1625–1640.

Thakur, P., Huang, Y., & Kaneko, Y. (2020). Effects of Low-Velocity Fault Damage Zones on Long-Term Earthquake Behaviors on Mature Strike-Slip Faults. *Journal of Geophysical Research: Solid Earth*, *125*(8), 1–20. https://doi.org/10.1029/2020JB019587

Thomas, M. Y., Lapusta, N., Noda, H., & Avouac, J. P. (2014). Quasi-dynamic versus fully dynamic simulations of earthquakes and aseismic slip with and without enhanced coseismic weakening. *Journal of Geophysical Research: Solid Earth*, *119*(3), 1986–2004. https://doi.org/10.1002/2013JB010615

Thompson, T., & Meade, B. (2019). *Earthquake cycle modeling of the Cascadia subduction zone*. https://doi.org/10.31223/OSF.IO/3VUXW

Trugman, D. T., Ross, Z. E., & Johnson, P. A. (2020). Imaging stress and faulting complexity through earthquake waveform similarity. *Geophysical Research Letters*, *47*(1), e2019GL085888.

Tse, S. T., & Rice, J. R. (1986). Crustal earthquake instability in relation to the depth variation of frictional slip properties. *Journal of Geophysical Research: Solid Earth*, *91*(B9), 9452–9472.

Utsu, T., Ogata, Y., & Ritsuko S, M. (1995). The centenary of the Omori formula for a decay law of aftershock activity. *Journal of Physics of the Earth*, *43*(1), 1–33.

van den Ende, M. P. A., Chen, J., Ampuero, J. P., & Niemeijer, A. R. (2018). A comparison between rate-and-state friction and microphysical models, based on numerical simulations of fault slip. *Tectonophysics*, *733*(November 2017), 273–295. https://doi.org/10.1016/j.tecto.2017.11.040

Vermilye, J. M., & Scholz, C. H. (1998). The process zone: microstructural view of fault growth. *Journal of Geophysical Research*, *103*.

Waldhauser, F., & Ellsworth, W. L. (2000). A Double-difference Earthquake location algorithm: Method and application to the Northern Hayward Fault, California. *Bulletin of the Seismological Society of America*, *90*(6), 1353–1368. https://doi.org/10.1785/0120000006

Wang, X., & Zhan, Z. (2020). Seismotectonics and Fault Geometries of the 2019 Ridgecrest Sequence: Insight From Aftershock Moment Tensor Catalog Using 3-D Green's Functions. *Journal of Geophysical Research: Solid Earth*, *125*(5), e2020JB019577.

Wei, M., & Shi, P. (2021). Synchronization of Earthquake Cycles of Adjacent Segments on Oceanic Transform Faults Revealed by Numerical Simulation in the Framework of Rate-and-State Friction. *Journal of Geophysical Research: Solid Earth*, *126*(1), 1–15. https://doi.org/10.1029/2020JB020231

Wesnousky, S. G. (1988). Seismological and structural evolution of strike-slip faults. *Nature*, *335*(6188), 340.

Wetzler, N., Brodsky, E. E., & Lay, T. (2016). Regional and stress drop effects on aftershock productivity of large megathrust earthquakes. *Geophysical Research Letters*, *43*(23), 12.

Wetzler, N., Lay, T., Brodsky, E. E., & Kanamori, H. (2018). Systematic deficiency of aftershocks in areas of high coseismic slip for large subduction zone earthquakes. *Science Advances*, *4*(2), eaao3225.

Wiemer, S., & Katsumata, K. (1999). Spatial variability of seismicity parameters in aftershock zones. *Journal of Geophysical Research: Solid Earth*, *104*(B6), 13135–13151.

Woodcock, N. H., & Rickards, B. (2003). Transpressive duplex and flower structure: Dent Fault System, NW England. *Journal of Structural Geology*, *25*(12), 1981–1992. https://doi.org/10.1016/S0191-8141(03)00057-9

Wu, X., Liang, L., Shi, Y., & Fomel, S. (2019). FaultSeg3D: Using synthetic data sets to train an end-to-end convolutional neural network for 3D seismic fault segmentation. *Geophysics*, *84*(3), IM35–IM45. https://doi.org/10.1190/geo2018-0646.1

Yabe, S., & Ide, S. (2017). Slip-behavior transitions of a heterogeneous linear fault. *Journal of Geophysical Research: Solid Earth*, *122*(1), 387–410.

https://doi.org/10.1002/2016JB013132

Yabe, S., & Ide, S. (2018). Why Do Aftershocks Occur Within the Rupture Area of a Large Earthquake? *Geophysical Research Letters*, *45*(10), 4780–4787. https://doi.org/10.1029/2018GL077843

Yang, H., Liu, Y., & Lin, J. (2012). Effects of subducted seamounts on megathrust earthquake nucleation and rupture propagation. *Geophysical Research Letters*, *39*(24), 2–7. https://doi.org/10.1029/2012GL053892

Yeats, R. S., Sieh, K., & Allen, C. R. (1997). *The Geology of Earthquakes*. Oxford University Press, USA.

Yu, H., Liu, Y., Yang, H., & Ning, J. (2018). Modeling earthquake sequences along the Manila subduction zone: Effects of three-dimensional fault geometry. *Tectonophysics*, *733*(August 2017), 73–84. https://doi.org/10.1016/j.tecto.2018.01.025

Yukutake, Y., & Iio, Y. (2017). Why do aftershocks occur? Relationship between mainshock rupture and aftershock sequence based on highly resolved hypocenter and focal mechanism distributions. *Earth, Planets and Space*, *69*(1), 68.

Zhu, W., Allison, K. L., Dunham, E. M., & Yang, Y. (2020). Fault valving and pore pressure evolution in simulations of earthquake sequences and aseismic slip. *Nature Communications*, *11*(1), 1–11. https://doi.org/10.1038/s41467-020-18598-z

Zielke, O., Galis, M., & Mai, P. M. (2017). Fault roughness and strength heterogeneity control earthquake size and stress drop. *Geophysical Research Letters*, *44*(2), 777–783. https://doi.org/10.1002/2016GL071700

Zielke, O., Klinger, Y., & Arrowsmith, J. R. (2015). Fault slip and earthquake recurrence along strike-slip faults - Contributions of high-resolution geomorphic data. *Tectonophysics*, *638*(1), 43–62. https://doi.org/10.1016/j.tecto.2014.11.004

Ziv, A., & Rubin, A. M. (2003). Implications of rate-and-state friction for properties of aftershock sequence: Quasi-static inherently discrete simulations. *Journal of Geophysical Research: Solid Earth*, *108*(B1).

Zoback, M., Hickman, S., & Ellsworth, W. (2010). Scientific drilling into the san andreas fault zone. *Eos*, *91*(22), 197–199. https://doi.org/10.1029/2010EO220001